

INCLUSION FORMATION IN THE SYSTEM Fe-FeO-FeS

by

JOHN COLIN YARWOOD

B.Sc. Manchester University 1964

Submitted in Partial Fulfillment of the Requirements

for the Degree of

DOCTOR OF PHILOSOPHY

at the

Massachusetts Institute of Technology

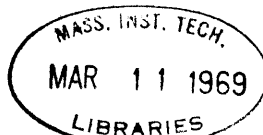
1968, i. e. Feb. 1969

Signature of Author  
Department of Metallurgy

Signatures of the Professors  
in Charge of Research

Signature of Chairman of  
Departmental Committee  
on Graduate Research

Archives



## INCLUSION FORMATION IN THE SYSTEM Fe-FeO-FeS

by

JOHN COLIN YARWOOD

Submitted to the Department of Metallurgy and Materials Science on December 11, 1968 in partial fulfillment of the requirements for the degree of Doctor of Philosophy.

---

## ABSTRACT

The processes by which inclusions form during solidification of Fe-O-S alloys were investigated based on the Fe-FeO-FeS phase diagram, which is dominated by a miscibility gap extending from the Fe-FeO binary in the liquid region.

In Part I of this study the location of the miscibility gap close to the iron corner of the phase diagram was determined. Experiments were performed in which an Fe-O-S melt was homogenized in the one phase region and then cooled; the temperature at which the slag phase separated out of the homogeneous liquid iron located a point on the surface of the miscibility gap. The form of the surface over a composition range of zero to 0.5% S and 0.15% to 0.30% O is expressed as a function of the absolute temperature as follows:

$$T = -5750/(\log\%O - 2.43) + \%S[-684-192(\log\%O - 2.43)]$$

The value of the interaction coefficient  $e_O^S$  was found to decrease from -0.08 at 1450°C to -0.16 at 1700°C.

In Part II, two models simulating the possible processes of solidification and inclusion formation involving the miscibility gap were constructed. Model 1, the "equilibrium" model, assumes complete equilibrium between solid iron and the two immiscible liquids during solidification. Model 2, the "isolation" model assumes entrapment of the oxygen-sulphur rich slag, formed because of the presence of the miscibility gap, in the solidifying iron. The inclusion compositions and their locations in the solid sections were determined for each model.

Experiments were performed in which levitated melts of various O/S ratios were equilibrated and solidified over a range of cooling rates. The compositions and locations of the inclusions observed correspond to those predicted by the "isolation" model.

The results indicate that during solidification of iron containing oxygen and sulphur, liquid pools rich in oxygen and sulphur are entrapped by the growing iron dendrites and isolated from liquid iron. This phenomenon results in the liquid iron enriching in sulphur up to the plait point of the miscibility gap and then solidifying as an interdendritic network of inclusions. Solidification of the entrapped oxygen-sulphur rich pools results in the formation of other inclusions having a range of composition.

Thesis Supervisors: Merton C. Flemings  
Title: Associate Professor of Metallurgy

John F. Elliott  
Title: Professor of Metallurgy

## TABLE OF CONTENTS

<u>Chapter Number</u>		<u>Page Number</u>
	ABSTRACT	ii
	LIST OF FIGURES	viii
	LIST OF TABLES	xiv
	ACKNOWLEDGEMENTS	xvi
I	INTRODUCTION	1
	Part I. THE SURFACE OF THE MISCIBILITY GAP	3
II	LITERATURE SURVEY	4
	A. Solubility of Oxygen in Liquid Iron	4
	1. Direct Measurements	5
	2. Indirect Measurements	7
	B. Solubility of Oxygen in Liquid Iron-Sulphur Alloys	8
III	OUTLINE OF THIS INVESTIGATION	11
IV	APPARATUS AND MATERIALS	12
	A. Description of Apparatus	12
	1. Levitation Apparatus	14
	2. Gas Purification	17
	3. Temperature Measurement	19
	B. Materials	21
V	EXPERIMENTAL PROCEDURE	22
	A. Sample Preparation	22
	B. Levitation	23
	C. Metallographic Examination and Chemical Analysis	24
VI	RESULTS	26
	A. Metallographic	26
	B. Chemical Analysis	26
	C. Oxide-Liquid Iron Phase Boundary	26

<u>Chapter Number</u>		<u>Page Number</u>
VII	ANALYSIS AND DISCUSSION OF RESULTS	29
	A. Solubility of Oxygen in Liquid Iron	29
	B. Solubility of Oxygen in Undercooled Iron	34
	C. Free Energy of Formation of FeO	35
	D. Solubility of Oxygen in Liquid Iron-Sulphur Alloys	37
	E. Interaction Coefficients	43
	1. Calculation of the Interaction Coefficients $e_O^S$ and $\epsilon_O^S$ as Functions of Temperature	46
	2. Calculation of $\eta_O^S$	50
VIII	SUMMARY AND CONCLUSIONS	51
	Part II. INCLUSION FORMATION	53
IX	LITERATURE SURVEY	54
	A. On Non-Metallic Inclusions	54
	B. On the Fe-FeS-FeO Phase Diagram	55
	C. Inclusion Formation in the System Fe-FeS-FeO	59
	D. On Solute Redistribution in Dendritic Solidification	64
X	OUTLINE OF INVESTIGATION	66
XI	SOLIDIFICATION MODELS	67
	A. The Fe-FeO-FeS Phase Diagram	67
	B. The Models	71
	1. Model 1: The "Equilibrium" Solidification Model	72
	2. Model 2: The "Isolation" Solidification Model	85
	3. Comparison of Models	102
	a. Inclusion composition	103
	b. Morphology and distribution of inclusions	105
XII	EXPERIMENTAL TECHNIQUES	107
	A. Apparatus	107
	B. Materials	107
	C. Experimental Procedure	107
	D. Metallography	109

<u>Chapter Number</u>		<u>Page Number</u>
XIII	RESULTS	111
	A. Composition of the Inclusions	111
	1. Qualitative Phase Identification	111
	2. The Range of Inclusion Composition	113
	a. Qualitative observations of inclusion composition	113
	b. Quantitative observations of inclusion composition	117
	(i) Composition range at constant cooling rate	118
	(ii) Maximum wustite content of the inclusion	118
	(iii) Effect of cooling rate	120
	B. Inclusion Morphology and Distribution	124
	1. Morphology and Distribution of Wustite Rich and Iron Sulphide Rich Inclusions	126
	2. Effect of O/S Ratio	128
	3. Effect of Solidification Rate	133
XIV	DISCUSSION	136
	A. Inclusion Composition	136
	1. Composition Range at Constant Cooling Rate	138
	2. Effect of O/S Ratio and Cooling Rate	142
	B. Morphology and Distribution of the Inclusions	145
XV	SUMMARY AND CONCLUSIONS	149
XVI	SUGGESTIONS FOR FURTHER WORK	151
XVII	BIBLIOGRAPHY	154
XVIII	APPENDICES	158
	A. Calibration of the Pyrometer	158
	1. Experimental Technique	158
	2. Calculation of the Standard Deviation	158
	B. Materials	161
	C. Sample Preparation for Optical Metallography	162
	D. Solubility of Oxygen in Undercooled Iron	163

Chapter  
NumberPage  
Number

E. Solubility of Sulphur and Oxygen in Solid Iron	166
F. Tie-Line Data	170
G. Considerations of the Effect of the Position of the Plait Point on Solidification	179
H. Equilibrium Solidification Model - Computer Program	187
I. Isolation Solidification Model - Computer Program	188
J. Point Counting Technique	189
K. Calculation of Inclusion Composition	193
BIOGRAPHICAL NOTE	202

## LIST OF FIGURES

<u>Figure Number</u>		<u>Page Number</u>
1	Experimental apparatus; (a) general view showing the generator, levitation furnace, gas purification train, pyrometer and recorder; (b) detailed view of the levitation furnace and charging and casting unit	13
2	Electrical circuit of the levitation furnace	15
3	Cutaway view of the charging and casting unit and the levitation furnace	16
4	Gas purification and storage system	18
5	Temperature measurement and recording system	20
6	Longitudinal section of an ingot showing allocations of portions for analysis	25
7	Solubility of FeO in liquid Fe-O alloys, a least squares fit of the data given in Table 1	31
8	Solubility of FeO in liquid Fe-O alloys. Curve (a) from Figure 7, curve (b) calculated from Figure 9 taking $e_O^O = -0.2$	32
9	Activity of oxygen in liquid Fe-O alloys (from the data of Table 1 corrected using $e_O^O = -0.2$ )	36
10	Iso-oxygen lines on the miscibility gap surface (least squares fits of the data of Table 2)	38
11	Slopes of the iso-oxygen lines of Figure 10 as %S $\rightarrow$ O as a function of reciprocal temperature. The line shown is a least square fit of the data	41



<u>Figure Number</u>		<u>Page Number</u>
12	Solubility of FeO in Fe-O-S alloys (lines obtained from equation 25)	42
13	Interaction coefficient $e_O^S$ as a function of reciprocal temperature (from equation 53)	49
14	Liquidus surface of the Fe-FeO-FeS system according to Hilty and Crafts <sup>12</sup>	57
15	Liquidus surface of the Fe-FeO-FeS system according to Schurmann and von Hertwig <sup>46</sup>	58
16	Schematic representation of inclusion formation in the Fe-FeO-FeS system at a high O/S ratio according to Crafts and Hilty <sup>39</sup>	62
17	Schematic representation of inclusion formation in the Fe-FeO-FeS system at a low O/S ratio according to Crafts and Hilty <sup>39</sup>	63
18	Sulphur content ( $C_{L1}$ ) versus oxygen content ( $C_{L1}^O$ ) in liquid iron ( $L_1$ ) at the intersection of the miscibility gap and iron liquidus surfaces	69
19	Sulphur content ( $C_{L2}$ ) of the liquid slag phase ( $L_2$ ) versus the sulphur content ( $C_{L1}$ ) of liquid iron ( $L_1$ ) at the intersection of the miscibility gap and iron liquidus surfaces	70
20	Composition and fraction of the three phases, $\alpha$ , $L_1$ and $L_2$ at a point in the monotectic three-phase reaction	75
21	Fractions of iron ( $f_\alpha$ ), $L_1$ ( $f_{L1}$ ) and $L_2$ ( $f_{L2}$ ) versus temperature during the three-phase monotectic reaction according to the "equilibrium" solidification model	79

<u>Figure Number</u>		<u>Page Number</u>
22	Schematic representation of inclusion formation in the Fe-FeO-FeS system according to the "equilibrium" solidification model	81
23	Inclusion composition versus O/S ratio of the melt for "equilibrium" solidification	84
24	Schematic illustration of the entrapment of liquid slag $L_2$ by the advancing $\alpha$ - $L_1$ interface	88
25	Compositions $C_\alpha$ , $C_{L_1}$ and $C_{L_2}$ and fractions $f_\alpha$ , $f_{L_1}$ and $f_{L_2}$ of the three phases $\alpha$ , $L_1$ and $L_2$ and their increments due to freezing of a differential quantity $df_\alpha$ of $L_1$ (a schematic diagram)	89
26	Fractions of iron ( $f_\alpha$ ), $L_1$ ( $f_{L_1}$ ) and $L_2$ ( $f_{L_2}$ ) as functions of temperature during the three-phase monotectic reaction according to the "isolation" solidification model	93
27	Schematic illustration of solidification in a small dendrite "volume element" of an Fe-FeO-FeS alloy according to the "isolation" model; (a) showing solid iron phase, $\alpha$ , growing dendritically and the liquid slag phase, $L_2$ , becoming entrapped by the $\alpha$ -phase, (b) continuation of this process as the liquid metal $L_1$ becomes enriched in oxygen and sulphur, (c) final stage of the three-phase monotectic reaction; the remaining interdendritic liquid having reached the plait point	94
28	Schematic illustration of the course of solidification on the Fe-FeO-FeS phase diagram leading to inclusion formation according to the "isolation" solidification model	96

<u>Figure Number</u>		<u>Page Number</u>
29	O/S ratio of the liquid slag $L_2$ versus the O/S ratio of the liquid iron $L_1$ at the intersection of the miscibility gap and iron liquidus surfaces (from the data of Hilty and Crafts <sup>12</sup> )	98
30	Fraction of the total amount of liquid slag ( $L_2$ ) precipitated during the monotectic reaction having an O/S greater than that of the ternary eutectic, $F_{L_2}^{TE}$ , as a function of the O/S ratio of $L_2$ the melt	99
31	Fraction of the total amount of liquid slag ( $L_2$ ) precipitated during the monotectic reaction which is precipitated before the alloy is half solidified, $F_{L_2}^{50}$ , versus the O/S ratio of the melt	100
32	Maximum volume percent of FeO or minimum volume percent of FeS dendrites in the inclusions as a function of the O/S ratio of the melt predicted by the equilibrium and isolation solidification models, based on data of Hilty and Crafts <sup>12</sup> (C) and Schurmann and von Hertwig <sup>46</sup> (S)	104
33	Photomicrographs of Fe-S-O alloys showing typical inclusions, unetched, 1000X	112
34	Photomicrographs of an Fe-0.14%S-0.175%O alloy (O/S = 1.25) solidification at 1°C/sec, unetched, 1000X. Shows inclusions of progressively decreasing O/S ratio	114-116
35	Photomicrographs of an Fe-0.15%S-0.175%O alloy (O/S = 1.25) solidified at 1°C/sec, unetched, 1000X. Show successive sections through the same inclusion	127

<u>Figure Number</u>		<u>Page Number</u>
36	(a) & (b): Photomicrographs of an Fe-0.34%S-0.17%O alloy (O/S = 0.5) solidified at 1°C/sec, unetched, 700X, showing the morphologies and relative positions of wustite rich and iron sulphide rich inclusions. (c) & (d) Photomicrographs of an Fe-0.2%S-0.1%O alloy solidified at 1°C/sec, unetched, 1000X, showing the proximity of wustite rich and iron sulphide rich inclusions	129
37	Photomicrographs of an Fe-0.4%S-0.05%O alloy (O/S = 0.125) solidified at 1°C/sec, unetched, showing: (a) inclusion morphology and distribution, 200X, (b) morphology of an iron sulphide rich inclusion, 1000X, (c) morphology of a wustite rich inclusion, 1000X	131
38	Photomicrographs of Fe-S-O alloys solidified at 10°C/sec, unetched, 100X, showing the effect of O/S ratio on inclusion morphology and distribution	132
39	Photomicrographs of Fe-S-O alloys, unetched, 1000X, showing morphology and distribution of inclusion solidified at different rates	134
40	Observed inclusion composition range compared to the range predicted by the "isolation" model (indicated by the arrows) for alloys of three different O/S ratios, all solidified at ~1°C/sec	139
41	Observed maximum volume percent of FeO or minimum volume percent of FeS dendrites in the inclusions compared to those predicted by the "equilibrium" and "isolation" models for alloys having a range of O/S ratios and all solidified at ~1°C/sec	141

<u>Figure Number</u>		<u>Page Number</u>
42	Observed range of inclusion composition for three alloys all having an O/S ratio of 0.5 but solidified at different rates, compared to the ranges predicted by the "isolation" model (indicated by arrows)	143
43	Observed range of inclusion composition for two alloys both having an O/S ratio of 1.25 but solidified at different rates compared to the ranges predicted by the "isolation" model (indicated by arrows)	144
A1	Distribution of melting point readings about the mean	159
D1	Solubility of oxygen in undercooled liquid iron. The line of Fischer and Ackermann <sup>11</sup> comes from equation D1 corrected to $a_{\text{FeO}} = 1$	164
G1	Schematic illustration of the Fe-FeO-FeS phase diagram used in considering "equilibrium" solidification	180
G2	Schematic illustration of the Fe-FeO-FeS phase diagram used in considering "isolation" solidification	183

## LIST OF TABLES

<u>Table Number</u>		<u>Page Number</u>
1	Solubility of FeO in Liquid Fe-O Alloys	27
2	Solubility of FeO in Liquid Fe-O-S Alloys	28
3	Solubility of Oxygen in Liquid Iron	33
4	Equations of Iso-Oxygen Lines on the Miscibility Gap	39
5	The Fe-FeO-FeS Phase Diagrams	68
6	Definition of Symbols	74
7	Range of Inclusion Composition	119
8	Maximum Wustite Content of Inclusions	121
9	Effect of Cooling Rate on Inclusion Composition Range	122
10	Effect of Cooling Rate on Inclusion Composition Range	123
B1	Lot Analysis of Ferrovac-E Iron	161
F1	Tie-Line Data Interpolated from the Phase Diagram of Hilty and Crafts <sup>12</sup>	171
F2	Tie-Line Data Interpolated from the Phase Diagram of Schurmann and von Hertwig <sup>46</sup>	175
J1	Comparison of the Point Counting and Areal Analysis Techniques	191
K1	Liquid Compositions and Weight Fractions of L <sub>2</sub> During Solidification Between the Miscibility Gap and the Eutectic Valley	195
K2	Liquid Compositions and Weight Fractions of the Various Phases Involved During the Solidification of L <sub>2</sub> from the Intersection of the Pseudobinary Eutectic to the Ternary Eutectic Point	198

Table  
NumberPage  
Number

K3	Inclusion Composition for Melts of Various O/S Ratios; "Equilibrium" Solidification Model	199
K4	Various Symbols Used in Appendix K	200

## ACKNOWLEDGEMENTS

The author wishes to express his sincere appreciation to Professors John F. Elliott and Merton C. Flemings for their guidance and constant encouragement throughout the course of this work.

Sincere thanks are also due to Professor John Chipman and to my fellow graduate students for many stimulating discussions and helpful suggestions.

The author also wishes to acknowledge the American Iron and Steel Institute for the financial support of this project.



## I. INTRODUCTION

Most inclusions found in steels are either oxides or sulphides. The nature of these inclusions and the manner in which they form can be understood in terms of specific modifications to the basic Fe-FeO-FeS phase diagram caused by the addition of alloying elements. A good deal of information on the composition and kinetics of formation of the various inclusions in particular steels has been gathered in the past. Most of this work was conducted on multicomponent systems under loosely controlled conditions, which limits the range of its application to other systems and conditions considerably. On the other hand relatively little work has been conducted on the nature of the basic Fe-FeO-FeS phase diagram and on inclusion formation in this system. It is considered that better understanding of these two aspects could form a sound basis for the understanding of inclusion formation in steels.

The purpose of the investigation was two-fold. In Part I of the study, the effect of sulphur on the solubility of oxygen in liquid iron was investigated over a range of temperatures. The data obtained were used to establish the location of the miscibility gap which exists in the liquid close to the iron rich corner of the Fe-FeO-FeS phase diagram, and to determine the value of the interaction coefficient  $e_O^S$  as a function of temperature.

In Part II the formation of inclusions during solidification of Fe-S-O alloys was investigated. Two possible solidification models; the "equilibrium" model and the "isolation" model, were constructed. With the aid of simple computer programs, solidification was simulated, according to the dictates of the two models, and the compositions, morphologies, and location of the inclusions were predicted. Small samples of Fe-S-O alloys were melted and solidified, under carefully controlled conditions, and the inclusions appearing in the solidified sections were characterized as to composition, morphology, and location. Comparison of the predicted and experimental results was used as a means of assessing the validity of the proposed models.

## PART I

## THE SURFACE OF THE MISCIBILITY GAP

## II. LITERATURE SURVEY

### A. Solubility of Oxygen in Liquid Iron

The solubility of oxygen in liquid iron can be measured directly or indirectly. A direct determination refers to a straight investigation of the reaction:



At any temperature  $\underline{\text{O}}$  refers to the solubility of oxygen in iron. Its value can be found by determination of the oxygen content of iron in equilibrium with a pure FeO slag at a particular temperature or by measurement of the temperature at which FeO is precipitated from liquid iron of known oxygen content. The latter temperature is referred to as the solution temperature of oxygen in liquid iron.

Impurities in the liquid iron or the iron oxide slag have an effect on the solubility of oxygen. Consider the equilibrium constant  $K_1$  for equation (1):

$$K_1 = \frac{a_{\text{FeO}}}{a_{\text{Fe}}} \cdot \frac{1}{a_{\text{O}}} \quad (2)$$

where  $a$  = activity

$$\text{Now, } a_{\text{O}} = f_{\text{O}} \cdot \% \underline{\text{O}}, \text{ where } f_{\text{O}} = \text{activity coefficient of oxygen} \quad (3)$$

Hence,

$$\% \underline{\text{O}} = \frac{a_{\text{FeO}}}{a_{\text{Fe}}} \cdot \frac{1}{f_{\text{O}}} \cdot \frac{1}{K_1} \quad (4)$$

In the pure binary system iron-oxygen at a particular temperature and oxygen level, the terms  $a_{\text{FeO}}$ ,  $a_{\text{Fe}}$  and  $f_{\text{O}}$  have specific constant values. As  $K_1$  is a constant the oxygen content,  $\%O$ , is fixed for these conditions and is the value required. However, if impurities, which affect the values  $a_{\text{FeO}}$  and  $f_{\text{O}}$ , are introduced the solubility of oxygen as expressed by  $\%O$  will change. For this reason corrections should be applied to measurements made in the presence of significant impurities.

The solubility of oxygen in liquid iron may also be determined indirectly by measurement of the equilibrium constant of two or more reactions, other than reaction (1), and manipulation of these constants to give  $K_1$ , usually as a function of temperature. Knowing the values of  $a_{\text{FeO}}$ ,  $a_{\text{Fe}}$  and  $f_{\text{O}}$  the solubility of oxygen can be deduced as a function of temperature.

#### 1. Direct Measurements.

The first measurement of oxygen solubility at a known temperature was conducted by the Bureau of Standards<sup>1</sup> and gave a value of 0.21 percent at the melting point of electrolytic iron in air. Tritton and Hanson<sup>2</sup> were able to reproduce this value by melting the charge of iron in a magnesia crucible under a nitrogen atmosphere. Herty and Gaines<sup>3</sup> measured the solubility in the range 1535°C to 1734°C. Their 50 lb heats were made in magnesia crucibles under air in an induction furnace. The oxygen content was found by sampling the melt with a fire-clay coated spoon,

casting into a steel mold, and analyzing the cast sample. Körber et al<sup>4,5</sup> used a similar technique and obtained results which agree quite well with those of Herty<sup>3</sup>. Both Herty<sup>3</sup> and Körber<sup>4,5</sup> relied on optical pyrometers for temperature measurement.

Chipman and Fetters<sup>6</sup> used a more refined technique to check the results of Herty<sup>3</sup> and Körber<sup>4,5</sup> which included the use of tungsten-molybdenum thermocouples instead of optical pyrometers. Seventy pound charges of iron were induction melted under air and pure nitrogen atmospheres in magnesia crucibles. The surface of the melt was covered by an iron oxide slag containing small amounts of MgO, CaO and SiO<sub>2</sub>. Both slag and metal were sampled by dipping small split molds into the melt and oxygen in the iron determined by vacuum fusion. No consistent differences in the oxygen content of liquid iron under slags containing 96% and 90% total iron oxides were found. For this reason no correction was made for variation in slag composition; the limiting solubility under pure FeO was expected to be greater than that measured but by less than the experimental errors of the investigation. The results differed considerably from those given by Herty and Gaines<sup>3</sup> and Körber<sup>4,5</sup> and for this reason they were checked by Taylor and Chipman<sup>7</sup>. The latter experimenters used a rotating induction furnace and a copper sampler into which the metal was sucked prior to analysis by vacuum fusion. As their results agreed quite well with those of Chipman and Fetters<sup>6</sup>, even under widely differing sampling techniques and

conditions, they concluded that the previous workers had been in error; the most probable error being temperature measurement. The results of Taylor and Chipman<sup>7</sup> are expressed by the relation:

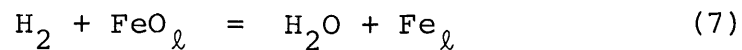
$$\log \%O = - \frac{6320}{T} + 2.734 \quad (5)$$

Fischer and vom Ende<sup>8</sup> carried out similar experiments to determine the solubility of oxygen in liquid iron under silica saturated slags. They concluded that, allowing for the difference in activity of FeO their results were in good agreement with those of Taylor and Chipman<sup>7</sup>. Fischer and Ackermann<sup>11</sup> were able to extend the range of these measurements down as far as 1320°C at which point the liquid iron was undercooled by about 200°C. Their results showed a lower solubility than would be expected from extrapolation of the equation given by Fischer and vom Ende<sup>8</sup>. No explanation was given for this discrepancy.

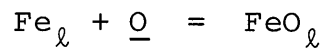
The method used in this study is the determination of the solution temperature for various alloys, the oxygen content of which could be found by analysis. As this technique had never been used before, the results were compared to the accepted values given by the other techniques to evaluate the accuracy of the new method.

## 2. Indirect Measurement.

Gokcen<sup>9</sup> and later Tankins, Gokcen and Belton<sup>10</sup> determined the equilibrium coefficients of reactions (6) and (7) below as functions of temperature.



Subtracting (7) from (6):



which is the equation (1) above; the required reaction. Thus, knowing  $K_6$  and  $K_7$ ,  $K_1$  may be calculated. From (4),  $\% \underline{\text{O}}$  the solubility of oxygen in liquid iron may be found, if  $f_{\text{O}}$  is known. Gokcen assumed  $f_{\text{O}}$  equal to 1 and found that at saturation with FeO:

$$\log \% \underline{\text{O}} = - \frac{5762}{T} + 2.439 \quad (8)$$

This equation shows good agreement with that of Taylor and Chipman<sup>7</sup> when the scatter of the data is taken into account. Both equations were considered in establishing the accuracy of the "solution temperature method" used in this study.

#### B. Solubility of Oxygen in Liquid Iron-Sulphur Alloys

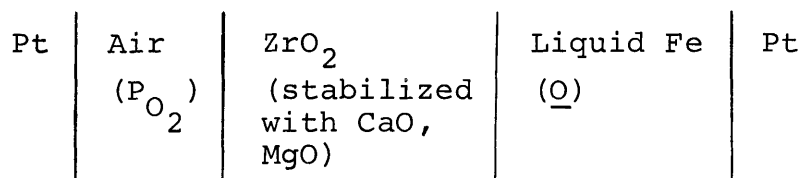
Hilty and Crafts<sup>12</sup> studied the effect of sulphur on the solubility of oxygen in liquid iron at 50°C intervals from 1450°C to 1650°C. They melted electrolytic iron in magnesia crucibles under an argon atmosphere in a rotating furnace. Sulphur was added as ferrous sulphide and the bath was saturated with oxygen at all times by addition of ferric



oxide when required. The oxygen in the metal samples was determined by a modified vacuum fusion method developed by Hamner and Fowler<sup>13</sup> and the sulphur was determined gravimetrically. Contamination of the slag by the crucible and the thermocouple protection tube was considered relatively unimportant. Plots of  $\log \%O$  versus  $\%S$  showed an initial dip in oxygen solubility followed by an upswing at all temperatures. Thus they report that sulphur in concentrations less than about 0.1% decreases the solubility of oxygen and that in greater concentrations it increases the solubility.

The interaction of sulphur with oxygen in liquid iron is characterized by the coefficient  $e_O^S = \left( \frac{d \log f_O}{d \%S} \right) \%Fe \rightarrow 100$ . This coefficient is not discussed by Hilty and Crafts<sup>12</sup>, but from the curvature of  $\log \%O$  at low sulphur concentration one can infer that it would be a small positive number.

Fischer and Ackermann<sup>14,15</sup> have measured  $e_O^S$  at 1600°C by studying the effect of  $\%O$  and  $\%S$  on  $a_O$ , the activity of oxygen in liquid iron. In their experiment they measured the e.m.f. of the following cell:



The cell reaction is  $O_{2(g)} = 2O$  and the equilibrium constant for this reaction  $K = (a_O)^2 / P_{O_2}$ . K was determined from the e.m.f. measurement at known levels of  $\%O$  and  $\%S$  and, knowing the value of  $P_{O_2}$ ,  $a_O$  was found as a function of

$\%O$  and  $\%S$ . For binary iron-oxygen alloys a plot of  $\log f_O$  versus percent oxygen suggests that  $e_O^O = \left(\frac{d \log f_O}{d \%O}\right) \%Fe \rightarrow 100'$  lies between +0.4 and -0.4. The scatter of the data showed no systematic deviation from Henrian behavior and so  $e_O^O$  was taken equal to zero in the subsequent determination of  $e_O^S$ . With  $e_O^O$  and hence  $\log f_O$  equal to zero the slope of a  $\log f_O$  versus  $\%S$  plot gives the value of  $e_O^S$ . In the first paper<sup>14</sup> a value of -0.12 is given. Further measurements were made and a new value of the enthalpy of the reaction  $\frac{1}{2}(O_2) = \%O$  was taken into account in the second paper<sup>15</sup> leading to a revised value of  $e_O^S = -0.104$ .

In the present study the solubility of oxygen in liquid iron-sulphur alloys was studied by the equivalent of the "solution temperature method" the accuracy of which had previously been established.

## III. OUTLINE OF THIS INVESTIGATION

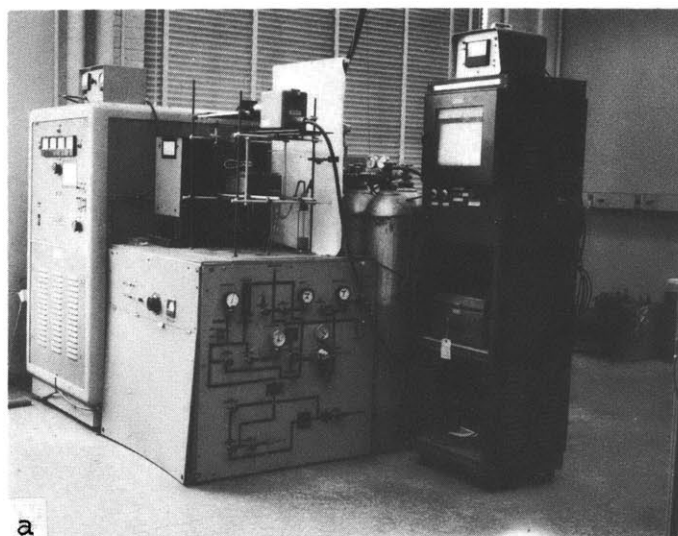
The object of the investigation was to determine in some detail the surface of the iron rich side of the miscibility gap in the Fe-FeO-FeS system. A temperature range of 1450°C to 1700°C and a sulphur composition range of zero to 0.5 weight percent was chosen. These data, once obtained, facilitate calculation of the interaction coefficient  $e_O^S$  as a function of temperature.

The method used involves homogenization of an iron-oxygen-sulphur melt in the one phase liquid region followed by cooling; the temperature at which the slag phase separates out of the homogeneous liquid iron, pinpoints a spot on the surface of the miscibility gap. However, this is only true so long as no measurable supersaturation is necessary for nucleation of the slag phase. For this reason a separate but similar set of experiments was carried out to check the validity of the technique. In the latter experiments the solution temperature of oxygen in the binary iron-oxygen system was measured by an identical technique. Reliable equilibrium data on the binary system is available (see Chapter II) and hence comparison of the observed experimental data with valid equilibrium data is possible. Conformity of the two sets of data was regarded as proof of the accuracy of the method in the ternary iron-oxygen-sulphur system, under the conditions described.

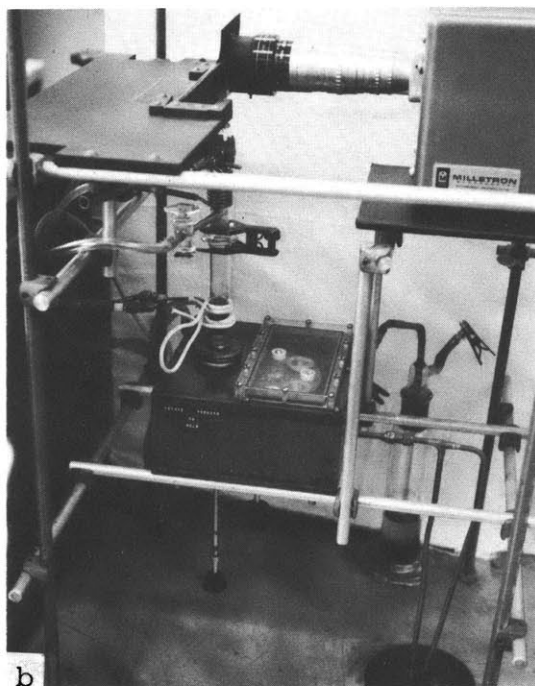
#### IV. APPARATUS AND MATERIALS

##### A. Description of Apparatus

The experiments outlined in this investigation demand freedom of the melt from contamination plus the ability to control the melt temperature and to monitor it continuously. Rapidity of homogenization and temperature cycling are also most desirable. In order to prevent contamination from curcible materials a levitation apparatus was chosen. Temperature control of the levitated melt may be affected by power or frequency regulation. A more practical method is to pass a cooling gas through a Vycor tube in which the droplet is levitated. The levitation coil was designed to fit around this tube exactly. Helium was used as the coolant and was purified prior to use to avoid oxidation of the melt. Continuous monitoring of the melt temperature was achieved by use of a two-color pyrometer and strip chart recorder. The assembled apparatus consisted of the levitation furnace and power source, the pyrometer, the gas purification train and the unit for charging and casting the samples. The latter was positioned under the Vycor furnace tube, and was designed as an integral part of the gas flow system to prevent atmospheric contamination during charging and casting. This apparatus satisfies all the requirements outlined above. A general view of the apparatus is presented in Figure 1.



a



b

Figure 1: Experimental apparatus.

- (a) General view showing the generator, levitation furnace, gas purification train, pyrometer and recorder.
- (b) Detailed view of the levitation furnace, and charging and casting unit.

## 1. Levitation Apparatus.

Using the levitation technique one can melt small quantities of conducting materials while suspending them in an electromagnetic field. The theories underlying levitation melting have been treated at length by Commentz<sup>16</sup> and by Fromm and Jehn<sup>17</sup> among others and will not be considered here. The levitation apparatus used in this investigation consists of the levitation furnace itself and the attached charging and casting unit.

### a. Levitation Furnace:

The levitation furnace was quite similar to that described by Strachan<sup>18</sup> and the external electrical circuit is illustrated in Figure 2. The 10KW, 400KC high frequency generator was matched to the low inductance levitation coil by insertion of a capacitor bank in parallel with the coil. In the resonant circuit formed, currents of about 400 amperes were measured under normal operating conditions. The coil itself, shown in Figure 3, was of the type described by Ward<sup>19</sup> and was connected to the capacitor bank by a coaxial lead to keep power losses to a minimum.

### b. Charging and Casting Unit:

The essential details of the unit are shown schematically in Figure 3. Basically it consists of a turntable, to hold the five charging cups and ingot molds, enclosed in an air-tight brass case. The turntable is operated from outside by a spindle passing through a double O-ring seal in the base plate of the case. Holes drilled in the turntable accommodate

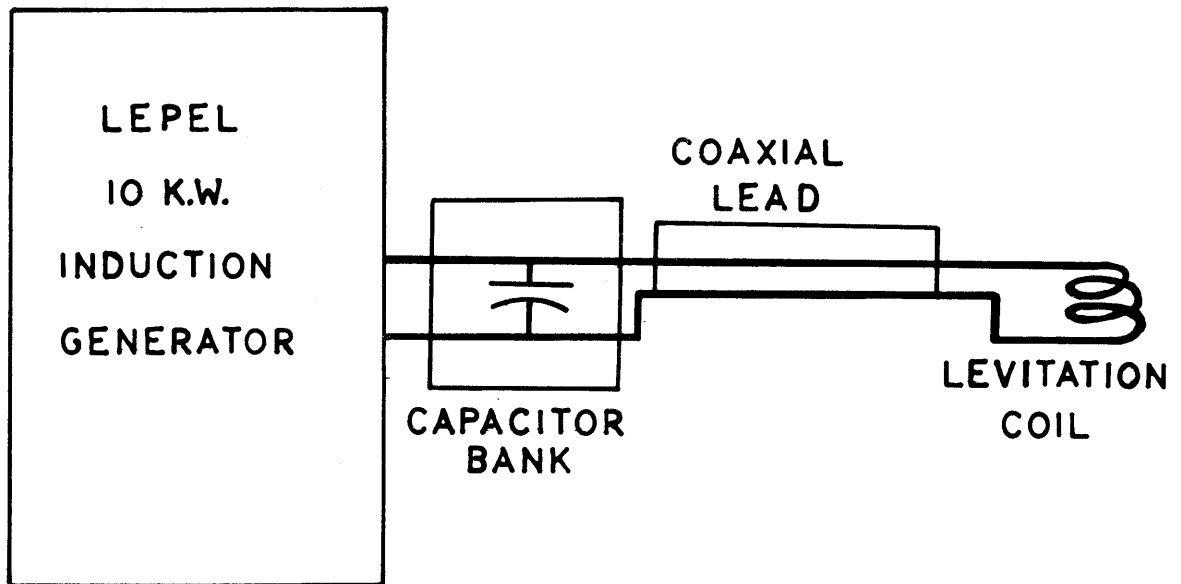


Figure 2. Electrical circuit of the levitation furnace.

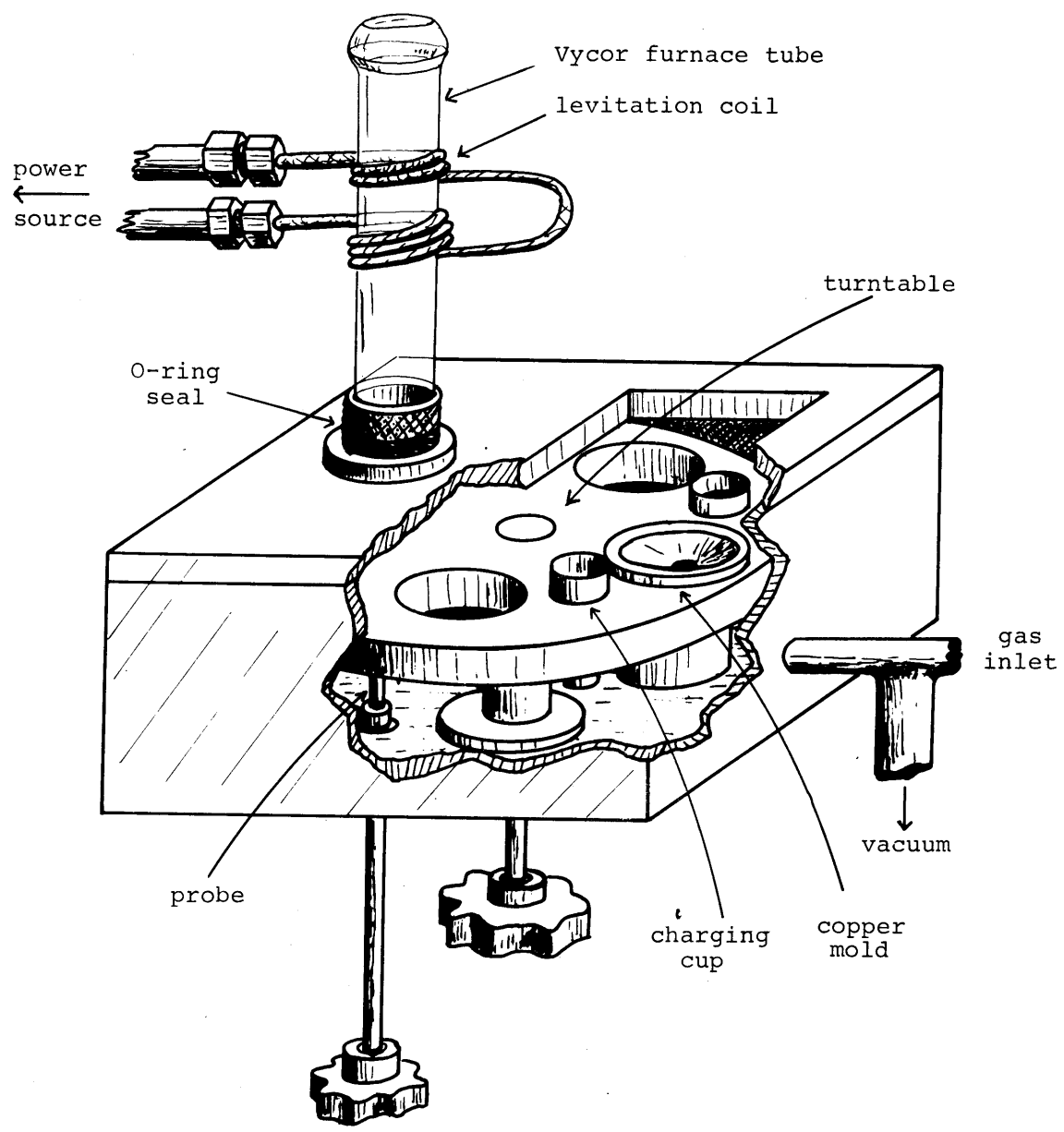


Figure 3. Cutaway view of the changing and casting unit and the levitation furnace.



the copper molds and boron nitride charging cups. The Vycor furnace tube is sealed into the top plate of the case by an O-ring seal designed for ease of assembly. Directly below the furnace tube a probe passing through the base plate by way of another double O-ring seal allows both vertical and rotational movement. A plexiglass window, fitted with an O-ring seal, affords access to the molds and charging cups. Gas enters through a copper tube, passing through a wall of the case and exits through a side arm of the furnace tube. A vacuum line is also fitted to the copper inlet tube to allow for evacuation of the case and the Vycor tube.

In order to charge the furnace, a charging cup is positioned directly above the probe by rotation of the turntable. The probe is then raised, supporting the cup and contained charge into the field of the coil, where levitation takes place. The cup is replaced onto the turntable by lowering the probe, and a mold stationed under the levitated droplet by further rotation of the turntable.

## 2. Gas Purification.

Gas flow rates up to  $200 \text{ ft}^3/\text{hr}$  were required for cooling purposes. Rather than build the extremely large furnaces, required to purify gas at these rates, small furnaces in conjunction with a reservoir system were used. A diagram of the gas purification train is presented in Figure 4.

Tank helium was passed through ascarite towers, to remove moisture, and through two copper furnaces to remove trace amounts of oxygen, before storage in a reservoir. A low flow

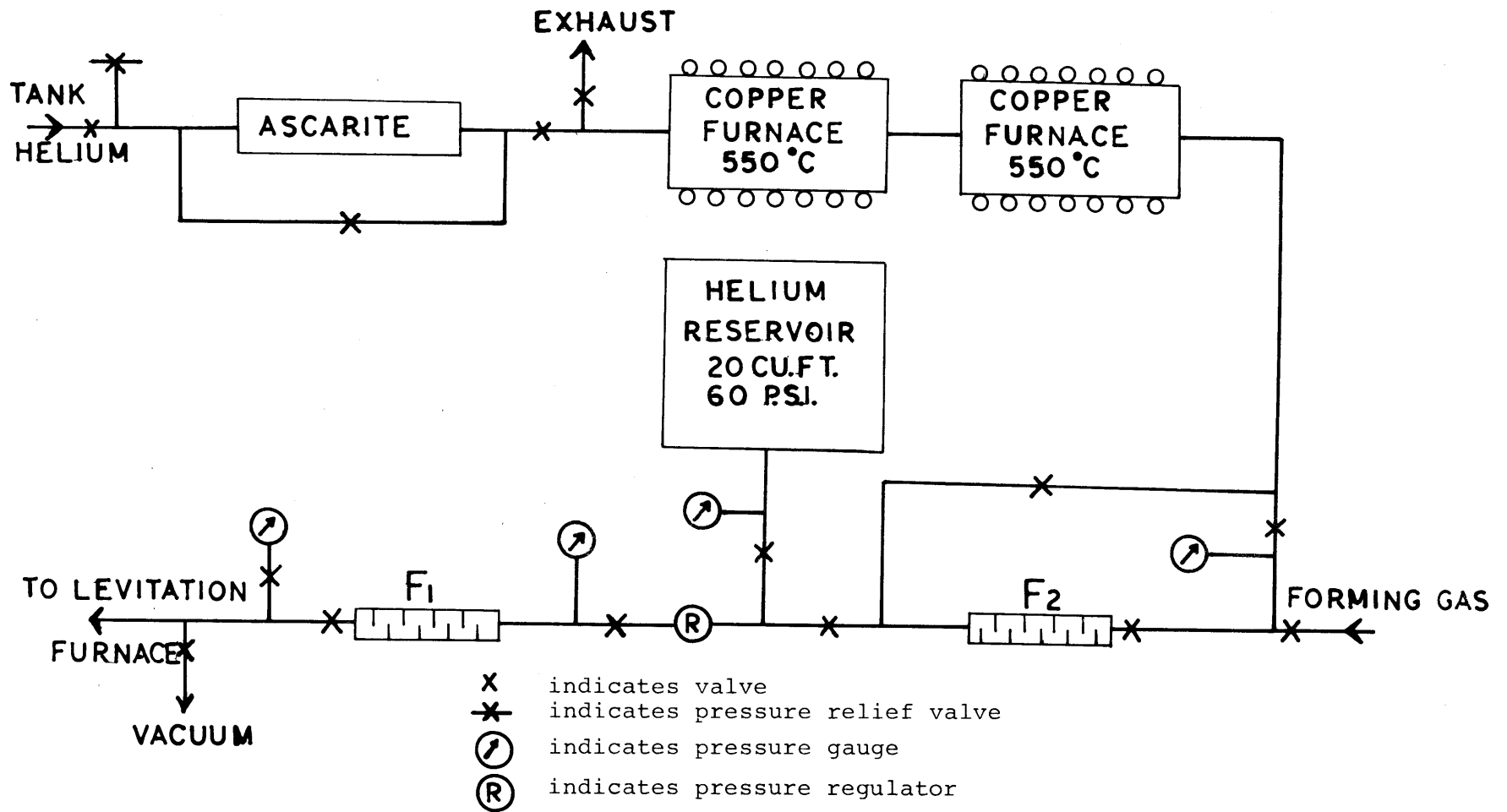


Figure 4. Gas purification and storage system.

rate, of approximately  $2 \text{ ft}^3/\text{hr}$ , was maintained by flowmeter-regulator  $F_2$  to ensure that the gas reached equilibrium in the furnaces. During an experimental run, the reservoir was discharged through the levitation furnace, at a rate controlled by flowmeter-regulator  $F_1$ . The vacuum line used to evacuate the levitation apparatus could also be used to evacuate the gas train if required. The copper furnaces were regenerated periodically with forming gas by regulation of the appropriate valves.

### 3. Temperature Measurement.

The temperature of the levitated specimen was monitored continuously by a Milletron two-color pyrometer or Thermo-O-Scope. The principle of a two-color pyrometer is to measure the ratio of the radiant energy in two wavebands. If the emitter is a gray body this ratio characterizes the temperature independent of the geometry, emittance and transmittance. The chief advantages of the two-color pyrometer in this study are, firstly; that changes in transmittance caused by fuming do not affect the recorded temperature appreciably, and secondly; the small changes in emissivity of a phase due to temperature variation have little effect.

The head of the pyrometer was sighted onto the top of the specimen through a prism as shown in Figure 5. The temperature could be read off the meter of the computation circuit and also it was recorded on a Honeywell strip chart recorder. Since small changes in transmittance and

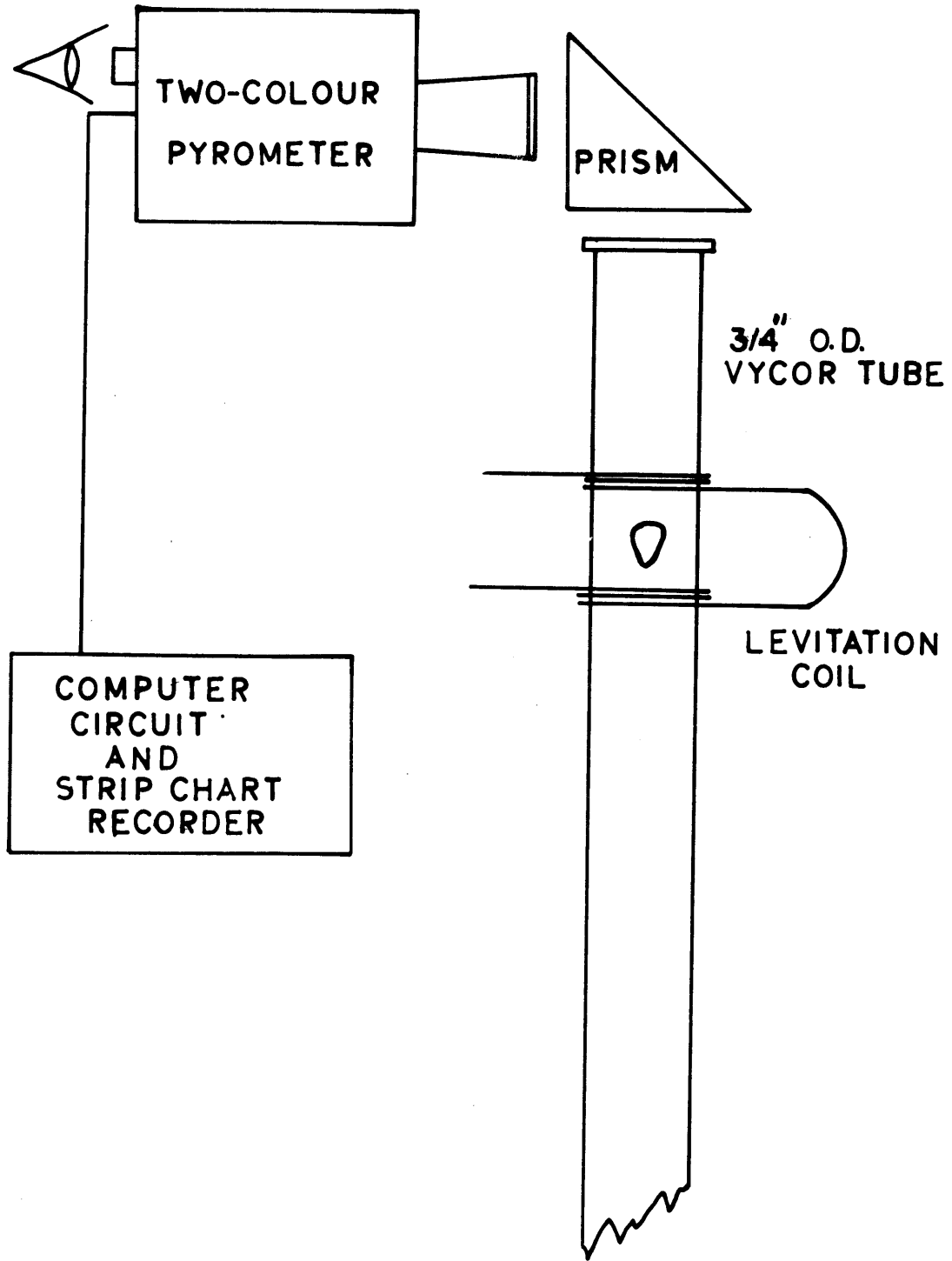


Figure 5. Temperature measurement and recording system.

emissivity can be disregarded the calibration of the pyrometer with the melting point of iron was sufficient to characterize the temperature over a range of 1300°C to 1700°C. The melting point of iron was found to be reproducible within a standard deviation,  $\sigma$ , of  $\pm 5^\circ\text{C}$ . Details of the calibration are given in Appendix A.

#### B. Materials

Materials used in this study consisted of iron, iron-oxide, and iron-sulphide. The form, source and analysis of each of these may be found in Appendix B.

## V. EXPERIMENTAL PROCEDURE

Two sets of experiments were performed, the first on iron-oxygen alloys and the second on iron-oxygen-sulphur alloys, as was explained in Chapter III. In both cases it was found possible to extend the range of investigation to temperatures at which the liquid iron phase was undercooled with respect to solid iron. Undercoolings greater than 200°C were often observed. Both sets of experiments were carried out in exactly the same way. Firstly samples of a known nominal composition were made up, the samples were then levitated and the temperature of appearance of the slag determined. The cast samples were sectioned for chemical and metallographic analyses.

### A. Sample Preparation

The Ferrovac-E rod was cleaned mechanically, pickled in hydrochloric acid and swaged down from half inch to five sixteenths of an inch diameter; a more convenient size for levitation. The rod was then sectioned transversely on a cut-off wheel to give samples weighing between 2 and 3 grams. A small hole was drilled into the axis of each sample and the samples again pickled, washed with water and acetone, and dried. The calculated quantities of oxide and sulphide, to give the required nominal composition, were introduced into holes which were then sealed using a hammer

and center punch. Up to five samples were placed in the boron nitride charging cups ready for levitation (Figure 3).

#### B. Levitation

The plexiglass window of the charging and casting unit was replaced and sealed. The unit and levitation furnace was evacuated and backfilled with helium four or five times and then helium was flushed through the system at a rate of  $5 \text{ ft}^3/\text{hr}$  for about half an hour. This reduced the oxygen partial pressure in the enclosure to a level where no oxidation of the samples occurred during the run. The power in the levitation coil was then run up to the maximum and the sample levitated in a manner described in Chapter IV.

Once levitated, the temperature of the sample was monitored continuously by the two-color pyrometer, recorded on the strip chart, and controlled by regulation of the gas flow rate. After melting and homogenizing for about one minute at  $1650^\circ\text{C}$  to  $1700^\circ\text{C}$  the temperature was dropped until the slag phase appeared on the surface of the sample. This point was easily recognizable as the emissivities of the iron and slag phases are different. The temperature at which the slag appeared was noted by stopping the strip chart recorder drive; the pen remaining at the temperature reached at that moment. The sample was allowed to heat up and homogenize and the cycle repeated several times. In this manner a reproducible solution temperature or slag appearance temperature was found. This temperature was not affected by

variation of the cooling rate over a range of 5°C/sec to 20°C/sec.

The change of emissivity, with the appearance of the second phase, did not affect the result as the temperature was determined by cooling through the homogeneous liquid iron range. In any case, if the chart drive was left running during the transition from one phase to two, no particular perturbation of the temperature reading was observed, indicating low sensitivity to the change of emissivity on the part of the pyrometer.

The experiment was concluded by homogenization of the sample at 1700°C and casting into a copper chill mold, Figure 3.

### C. Metallographic Examination and Chemical Analysis

Chemical analysis of the samples was considered advisable to check that no change in composition occurred during the run. As only a fraction of each sample was required for analysis, macrosegregation of either oxygen or sulphur would affect the result of this analysis. For this reason metallographic examination and chemical analysis of the top, middle and bottom sections of the casting were performed.



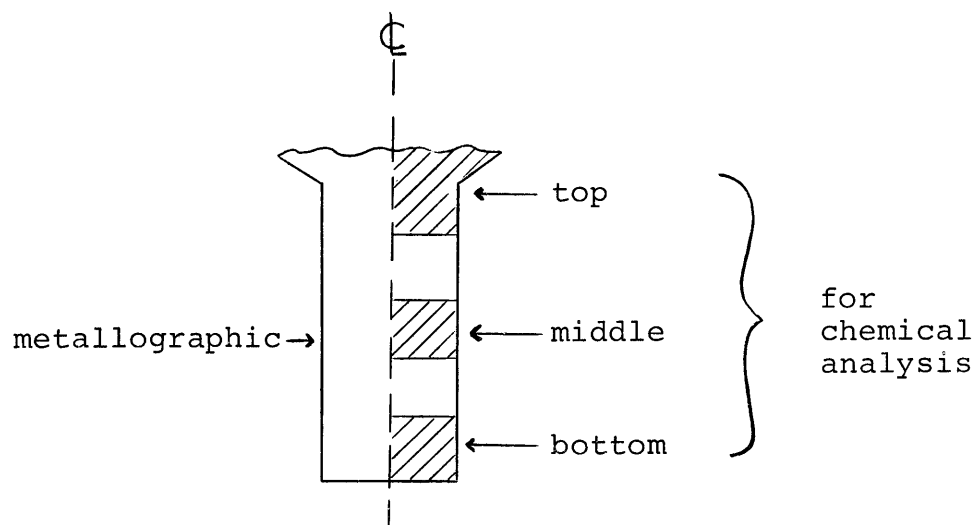


Figure 6: Longitudinal section of an ingot showing allocations of portions for analysis.

The cast samples were set in "E-Z Mount" plastic and sectioned in the manner shown in Figure 6. One half of the sample was examined metallographically and the other half was chemically analyzed. The metallographic examination included sulphur printing and optical microscopy of the polished and etched sections. Grinding and polishing techniques are described in Appendix C. Oxygen analysis was determined by inert gas fusion and sulphur analysis by conversion of sulphur to sulphur-trioxide by combustion, followed by titration against iodine.

## VI. RESULTS

### A. Metallography

The metallographic examination by optical microscopy and sulphur printing, described in Chapter V, revealed that all samples cast from 1700°C after homogenization were free from macrosegregation.

### B. Chemical Analysis

Five samples of both iron-oxygen and iron-oxygen-sulphur alloys, the top, middle and bottom sections of which were analyzed, showed no macrosegregation. For this reason only one analysis was made on subsequent samples. Fifteen of the iron-oxygen alloys and six of the iron-oxygen-sulphur alloys were analyzed. The results showed that the composition change during an experimental run was quite small. The difference between the nominal or "weighed out" composition and the "chemically analyzed" composition was less than 5% in all cases. Consequently the original nominal composition of an analyzed melt was taken to be the true composition.

### C. Oxide-Liquid Iron Phase Boundary

The results of "slag appearance temperature" experiments on the iron-oxygen and iron-oxygen-sulphur systems are presented in Tables 1 and 2.

Table 1  
Solubility of FeO in Liquid Fe-O Alloys

<u>wt pct oxygen</u>	<u>temp., °C</u>	<u>wt pct oxygen</u>	<u>temp., °C</u>
0.080	1340	0.165	1527
0.095*	1355	0.180*	1535
0.095*	1387	0.185*	1542
0.100	1385	0.200	1560
0.100	1395	0.200	1560
0.100	1415	0.200	1577
0.100*	1435	0.200	1580
0.110*	1405	0.220*	1587
0.110	1412	0.230	1610
0.120	1425	0.240	1600
0.120	1462	0.250	1627
0.120*	1470	0.280*	1650
0.140*	1495	0.300	1645
0.150*	1480	0.305*	1667
0.150	1497	0.345*	1702
0.150	1502	0.350*	1698
0.160	1510	0.360	1710
0.160*	1512	0.400	1730
0.160	1515		

\* Analyzed.

Table 2  
Solubility of FeO in Liquid Fe-O-S Alloys

<u>wt pct oxygen</u>	<u>wt pct sulphur</u>	<u>temp., °C</u>	<u>wt pct oxygen</u>	<u>wt pct sulphur</u>	<u>temp., °C</u>
0.150	0.10	1489	0.200	0.20	1542
0.150	0.20	1487	0.200	0.30	1535
0.150	0.20	1480	0.200*	0.30	1531
0.150	0.30	1478	0.200	0.40	1525
0.150	0.30	1473	0.200	0.50	1518
0.150	0.40	1472	0.250*	0.05	1610
0.150	0.50	1471	0.250	0.10	1619
0.150	0.50	1464	0.250	0.20	1598
0.175	0.05	1528	0.250	0.30	1594
0.175	0.10	1510	0.250*	0.39	1573
0.175	0.20	1516	0.250	0.50	1571
0.175	0.30	1506	0.300	0.05	1666
0.175	0.40	1502	0.300*	0.09	1663
0.175	0.50	1496	0.300*	0.19	1649
0.200	0.05	1558	0.300	0.30	1632
0.200	0.05	1554	0.300	0.40	1626
0.200	0.10	1558	0.300	0.50	1617
0.200*	0.10	1554			
0.200	0.10	1552			

\* Analyzed.

## VII. ANALYSIS AND DISCUSSION OF RESULTS

The results of the experimental determination of the solubility of oxygen in liquid iron were used to establish the veracity of the technique for measurement of the solubility of oxygen in iron-sulphur alloys. The data referring to oxygen solubility in undercooled iron was compared to those of Fischer and Ackermann<sup>11</sup> and also the standard free energy of formation of liquid FeO was estimated. The data from both the iron-oxygen experiments and the iron-sulphur-oxygen experiments were then combined to establish the form of the miscibility gap surface over a specified range of temperature and composition. Also the interaction coefficient  $e_O^S$  was determined as a function of temperature.

A. Solubility of Oxygen in Liquid Iron

Theoretically a straight line relationship is expected when the logarithm of the solubility is plotted versus the reciprocal of the absolute temperature over short intervals. Therefore, such a plot was made in Figure 7 using the data of Table 1. However, it is questionable whether the data given in this table truly represent the equilibrium solubility of oxygen in liquid iron. This is because under the experimental conditions described the iron-oxide phase would be expected to form by homogeneous nucleation, which requires a certain undercooling, or possibly by spinodal decomposition. The undercooling required for homogeneous nucleation may be

calculated knowing the interfacial energy between the iron and oxide liquids. However, no data of this kind is available. Fortunately, reliable data for the solubility of oxygen in liquid iron is available<sup>6-8</sup> and direct comparison of the experimental results with the accepted values can be used to resolve the question of undercooling.

The data of Taylor and Chipman<sup>7</sup> was used as reliable equilibrium data for comparison with the present study. A least squares analysis was used to determine the coefficients C and D of the straight line  $\log \%O = C + D/T$  for the data of both the present work and that of Taylor and Chipman. The computer program containing subroutines DLSQ used to make the fit is described elsewhere by Larson<sup>20</sup>. The resultant lines are shown, along with the data from this study in Figures 7 and 8. The error involved in the measurement of percent oxygen, estimated to be about 5%, overshadows the 10°C or 0.5% estimated error in temperature measurement so that resultant deviation can be attributed to error in oxygen analysis only, as a first approximation. Using this assumption the computer program was set up to determine statistically the standard single deviation in C and D and also in the line, given by the equation, over the experimental range. The statistical deviation in one measurement of  $\log \%O$  was calculated for comparison with the estimated value of 5% error. The equation and the various deviations are given in Table 3.

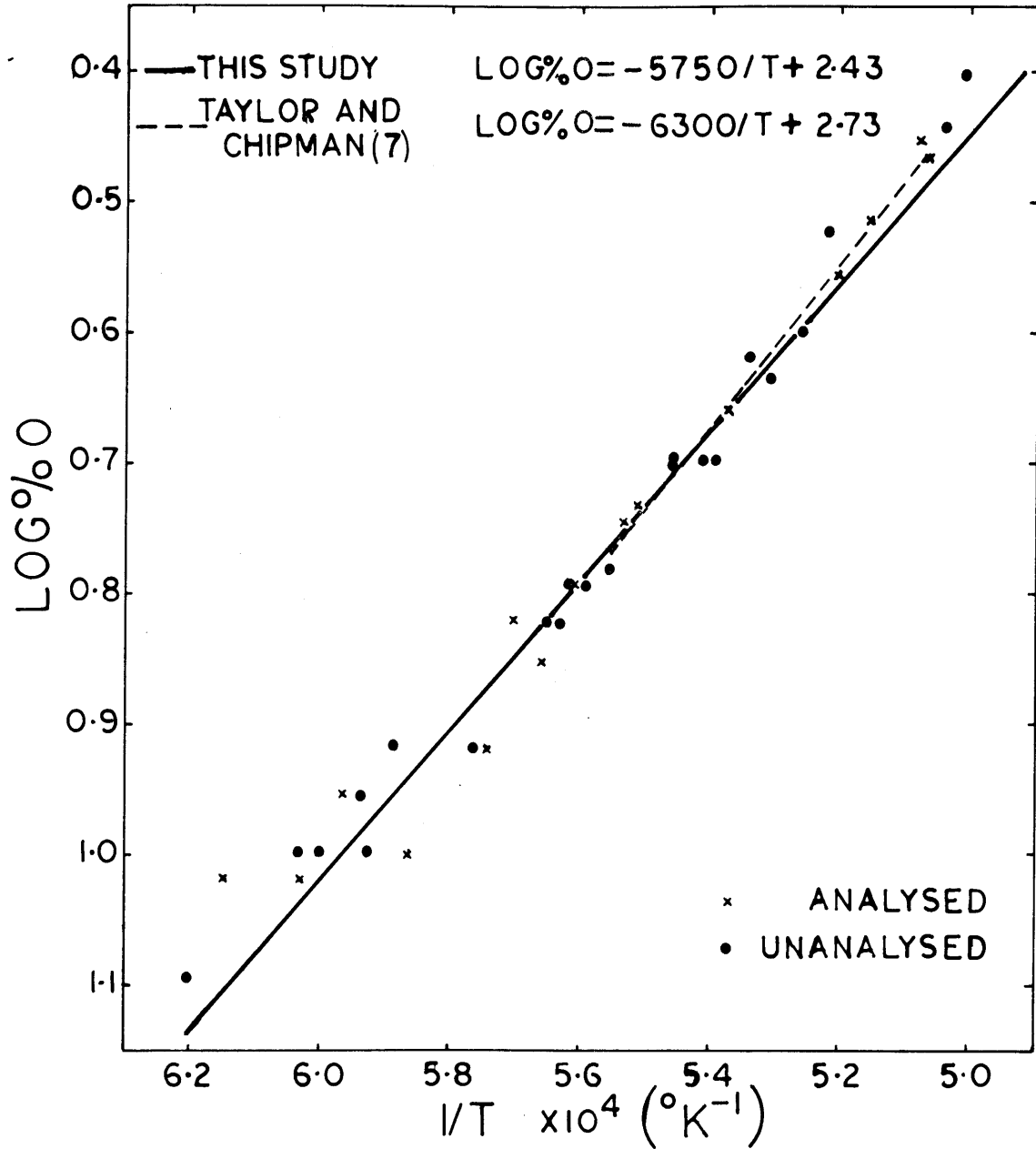


Figure 7. Solubility of FeO in liquid Fe-O alloys, a least squares fit of the data given in Table 1.

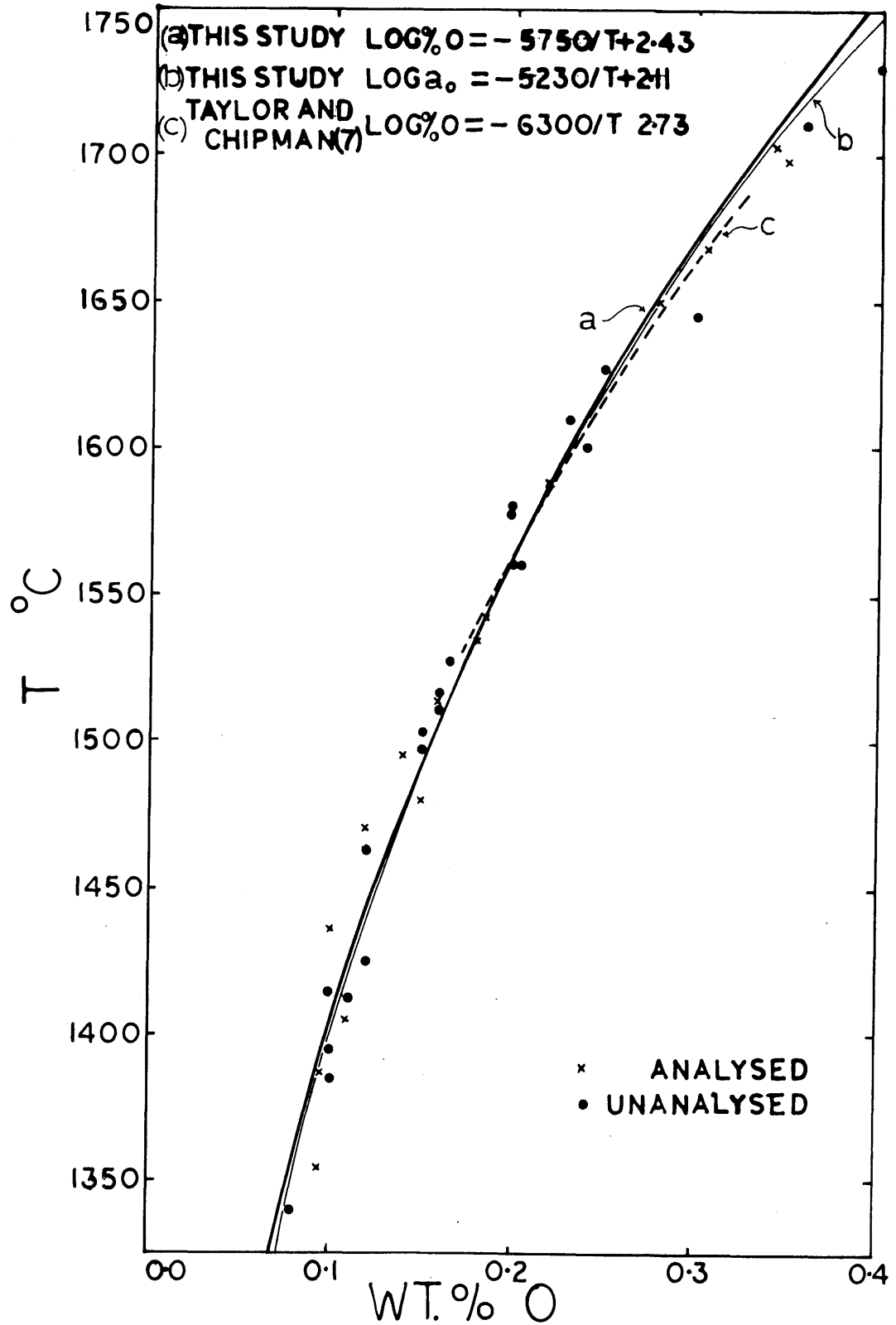


Figure 8. Solubility of FeO in liquid Fe-O alloys. Curve (a) from Figure 7, curve (b) calculated from Figure 9 taking  $e_o^O = -0.2$ .



Table 3  
Solubility of Oxygen in Liquid Iron

<u>source of data</u>	<u>log%O=C+D/T</u>	<u>temperature range, °C</u>	<u>standard deviations (<math>\sigma</math>)</u>			
			<u>S<sub>Y</sub></u>	<u>S<sub>L</sub></u>	<u>S<sub>C</sub></u>	<u>S<sub>D</sub></u>
Present work	2.43-5750/T (9)	1340-1730	0.030	0.01	0.1	150
Taylor and Chipman <sup>7</sup>	2.73-6300/T (10)	1530-1690	0.025	0.01	0.2	400

where  $S_Y$  = standard deviation in one measurement of log %O

$S_L$  = standard deviation of the line

$S_C$  = standard deviation of term C

$S_D$  = standard deviation of term D

The value of the standard deviation  $S_Y$  given corresponds to an error of the order of 5% and hence is in good agreement with the previously estimated experimental error. Comparison of the values of C and D for the present work and that of Taylor and Chipman<sup>7</sup> shows that they are within the same range when the standard deviations  $S_C$  and  $S_D$  are taken into account. Also one can see that the lines in Figure 7 overlap over the entire common range when the standard deviations ( $S_L$ ) are considered. Thus, the present work is in very good agreement with that of Taylor and Chipman<sup>7</sup>. The undercooling for homogeneous nucleation, therefore, must be too small for measurement using the present experimental technique.

Kozakevitch<sup>21</sup> estimates that the interfacial tension between an industrial blast furnace slag containing 1% S and

3% C is about 5 dyne/cm. This is about 160 times less than the interfacial tension between the same slag and sulphur free iron of the same carbon content<sup>21</sup>. For this reason the addition of sulphur to the melt in the present work would be expected to decrease the undercooling required for nucleation. Since no undercooling was recorded in the sulphur free experiments none would be expected in the presence of sulphur. Thus the experimental determination of the solubility of oxygen in iron-sulphur alloys should yield true equilibrium data.

#### B. Solubility of Oxygen in the Undercooled Iron

As can be seen from Figure 8 the measurement of oxygen solubility in liquid iron was extended into the temperature range where liquid iron is undercooled with respect to the solid. During these experiments it became apparent that the liquid FeO did not act as a nucleating agent for solid iron as both liquid FeO and undercooled liquid iron existed together for indefinite periods of time. It was also observed that the measured solubility agrees closely with the extrapolated solubility line of Taylor and Chipman<sup>7</sup>. The only other known experimental study of the solubility of oxygen in undercooled iron was made by Fischer and Ackermann<sup>11</sup>. However, they reported solubility of oxygen under a silica saturated slag and so direct comparison of the results is not possible. The results may be compared indirectly knowing the activity of FeO in the silica saturated slags and this is done in Appendix D.

### C. Free Energy of Formation of FeO

The activity of oxygen in liquid iron saturated with FeO may be found using the relation:

$$\log a_{\text{O}} = \log (\% \underline{\text{O}}) + e_{\text{O}}^{\text{O}} \% \underline{\text{O}} \quad (11)$$

The interaction coefficient  $e_{\text{O}}^{\text{O}}$  is taken<sup>22</sup> equal to -0.2. The activity relation was determined by adding the  $e_{\text{O}}^{\text{O}} \% \underline{\text{O}}$  term to each value of  $\log (\% \underline{\text{O}})$  obtained from the data and fitting a straight line to this "corrected" data by the least squares method already described. The data from this study and that of Taylor and Chipman<sup>7</sup> were treated in this way yielding:

For this study:

$$\log a_{\text{O}} = -5,230 (\pm 150)/T + 2.11 (\pm 0.07) \quad (12)$$

For Taylor and Chipman<sup>7</sup>:

$$\log a_{\text{O}} = -5,600 (\pm 350)/T + 2.31 (\pm 0.18) \quad (13)$$

A plot of equation (12) and the data from which it was derived is given in Figure 9. Equation (11) was used to calculate  $\% \underline{\text{O}}$  as a function of temperature using values of  $a_{\text{O}}$  from equation (12) taking<sup>22</sup>  $e_{\text{O}}^{\text{O}}$  equal to -0.2. The result, shown in Figure 9, fits the data somewhat better than the plot derived from equation (9).

Also, using the expression  $\Delta G^{\text{O}} = -RT \ln K$ , where  $K$  is the equilibrium constant, the standard free energy for the reaction:

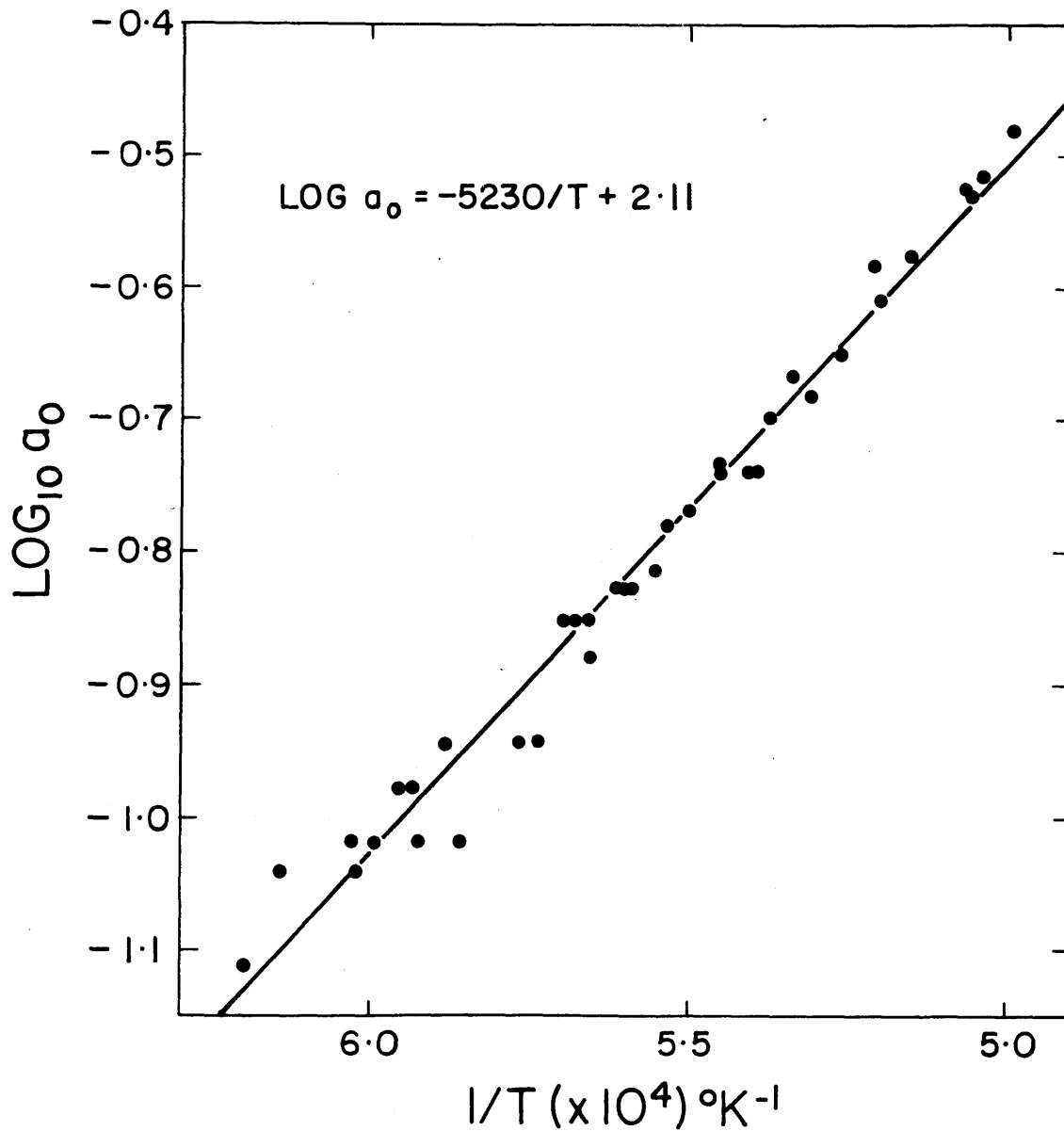


Figure 9. Activity of oxygen in liquid Fe-O alloys (from the data of Table 1 corrected using  $e_o^0 = -0.2$ ).



for which

$$K = \frac{a_{\text{FeO}}^1}{a_{\text{Fe}} \cdot a_{\text{O}}^1} \quad \text{may be found.}$$

For this study:

$$G^{\circ} = -23,950(\pm 600) + 9.66(\pm 0.32)T \text{ cal/gm-mole} \quad (15)$$

For Taylor and Chipman<sup>7</sup>:

$$G^{\circ} = -25,700(\pm 1,600) + 10.58(\pm 0.84)T \text{ cal/gm-mole} \quad \dots\dots (16)$$

#### D. Solubility of Oxygen in Liquid Iron-Sulphur Alloys

The data on the solubility of oxygen in iron-sulphur alloys given in Table 2 is shown graphically in Figure 10. Here the slag appearance temperature is plotted as a function of the sulphur content for the five different oxygen levels investigated. The points fall on a straight line within the accuracy of the experiment and so a straight line was drawn through each of the five sets of data using the least squares technique already described. The resultant equations are shown in Table 4.

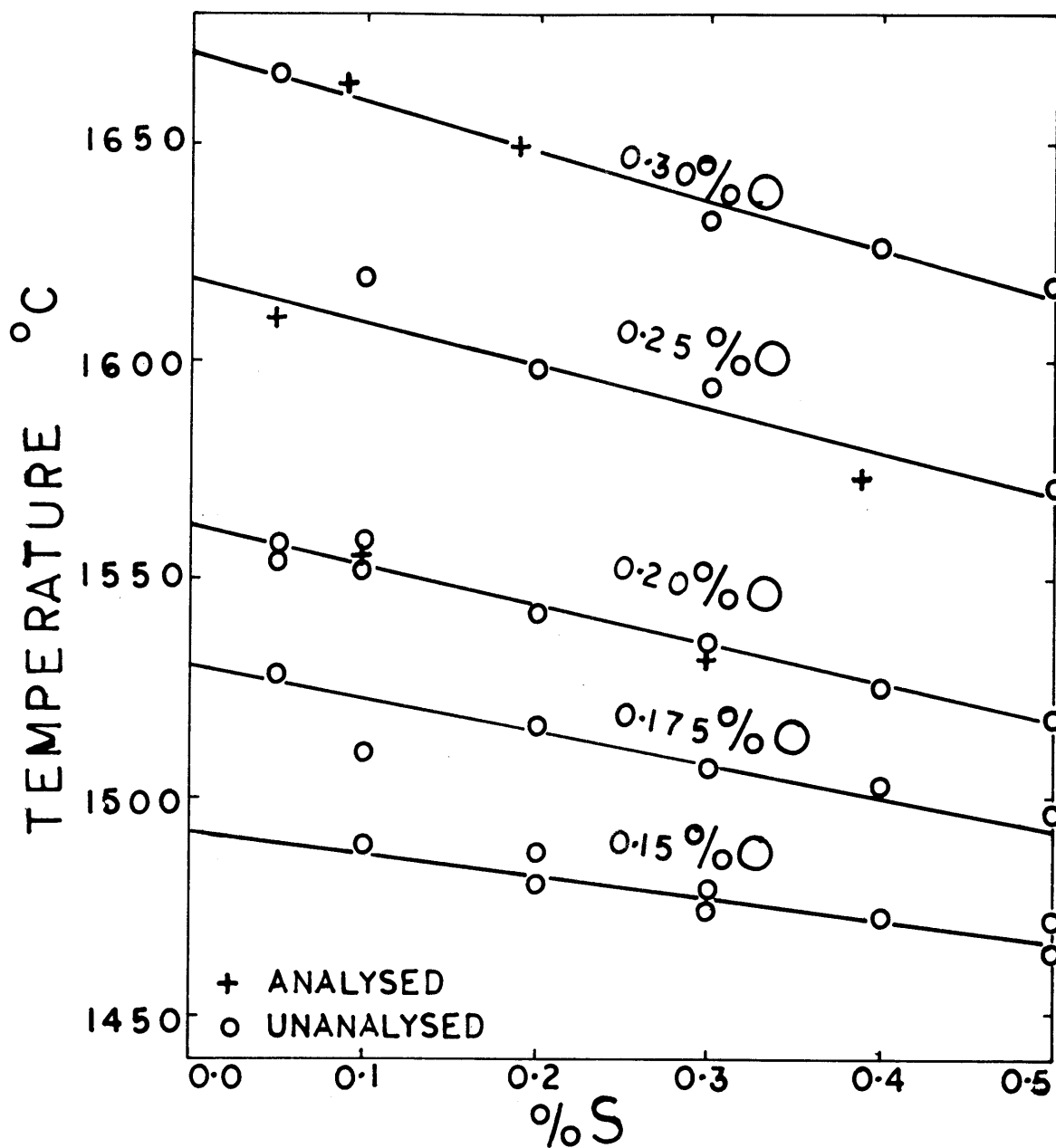


Figure 10. Iso-oxygen lines on the miscibility gap surface (least squares fits of the data of Table 2).

Table 4

Equations of Iso-Oxygen Lines on the Miscibility Gap

<u>percent oxygen</u>	<u>iso-oxygen line temperature (°C)</u>
0.15	T=1492 - 51wt.% <u>S</u>
0.175	T=1530 - 76wt.% <u>S</u>
0.20	T=1562 - 91wt.% <u>S</u>
0.25	T=1619 - 99wt.% <u>S</u>
0.30	T=1671 - 113wt.% <u>S</u>

These equations represent iso-oxygen lines on the surface of the miscibility gap over a limited range of temperature and sulphur content. The limit of this surface where it touches the iron-oxygen binary is also known. This limit is given by the equation for the solubility of oxygen in liquid iron. These data may be combined to yield an equation which defines the surface of the miscibility gap completely over the range investigated.

The equations in Table 4 are of the form:

$$T = T' - F \%S \quad (17)$$

where  $T'$  is the intercept at  $\%S = 0$  and  $F = [dT/d\%S]_{\%S \rightarrow 0}$

From the table it can be seen that  $F$  is a function of  $T'$ . In Figure 11,  $[dT/d\%S]_{\%S \rightarrow 0}$  is plotted versus the reciprocal of  $T'$  ( $^{\circ}K^{-1}$ ). A straight line represents the relation between  $[dT/d\%S]$  and  $1/T'$  adequately, within the accuracy of the data. The least squares fit shown in Figure 11 gives the relation:

$$[dT/d\%S]_{\%S \rightarrow 0} = -684 + 110 \times 10^4 (1/T') \quad (18)$$

or

$$F = A + B/T' \quad (19)$$

Also for iron-oxygen alloys wheres  $\%S = 0$  and thus  $T = T'$ , it was shown that:

$$\log \%O = -5750/T' + 2.43 \quad (20)$$

Or

$$\log \%O = C + D/T' \quad (21)$$

from (3)

$$T' = D/(\log \%O - C) \quad (22)$$

substituting (22) in (19)

$$F = A + (B/D)(\log \%O - C) \quad (23)$$

and substituting (22) and (23) in (17)

$$T = D/(\log \%O - C) + [A + (B/D)(\log \%O - C) \%S] \quad (24)$$

This is the equation of the surface of the miscibility gap from 0.0% to 0.5% sulphur and 0.15% to 0.30% oxygen.

Substituting the numerical values of the constants we find that:

$$T = \frac{-5750}{(\log \%O - C)} + \%S [-684 - 192(\log \%O - 2.43)] \quad (^\circ K) \quad \dots\dots (25)$$



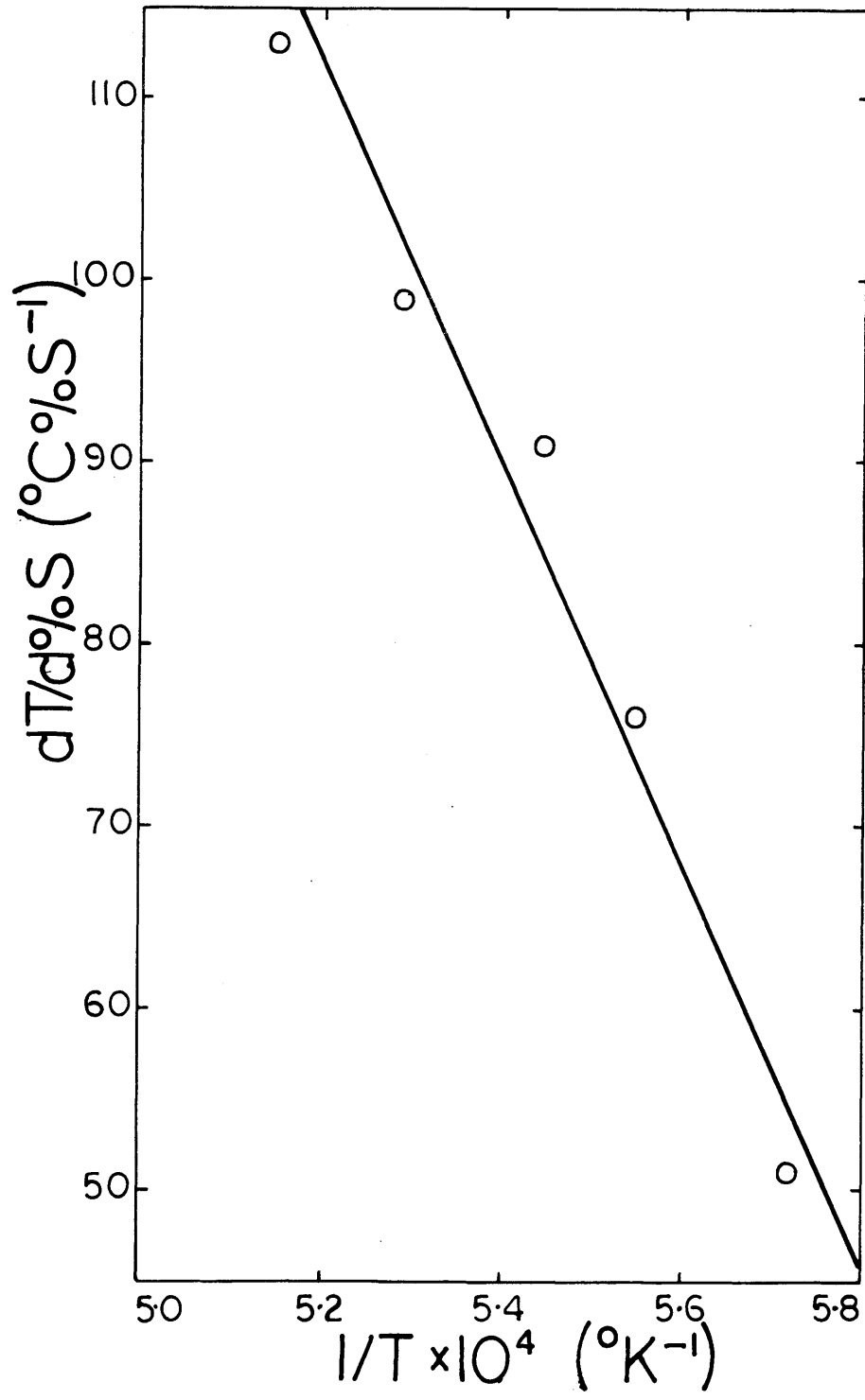


Figure 11. Slopes of the iso-oxygen lines of Figure 10 as  $\%S \rightarrow 0$  as a function of reciprocal temperature. The line shown is a least squares fit of the data.

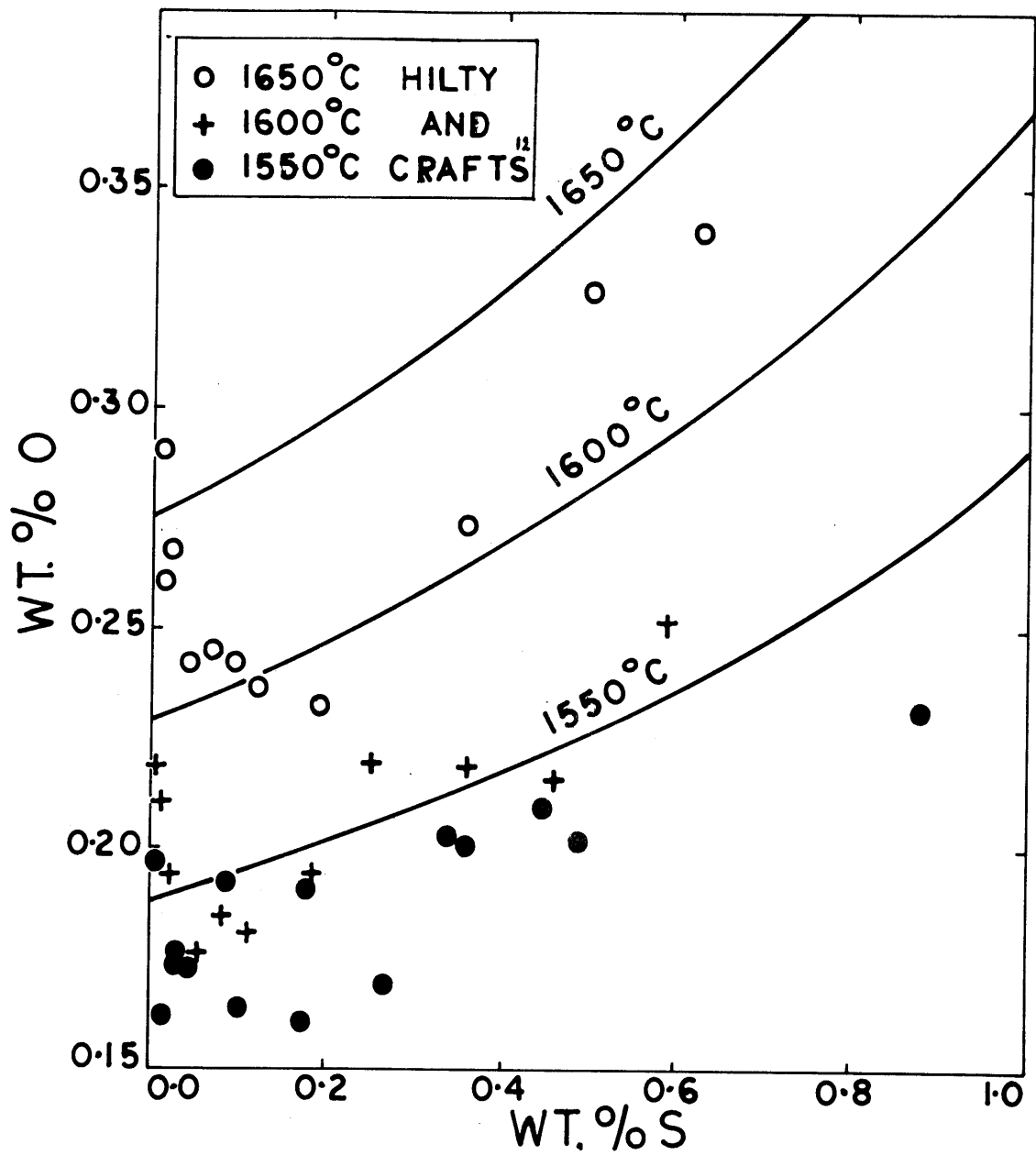


Figure 12. Solubility of FeO in Fe-O-S alloys (lines obtained from equation 25).

By use of equation (25) the effect of increasing amounts of sulphur on the solubility of oxygen in liquid iron at various temperatures can be shown graphically. In Figure 12 the 1550°C, 1600°C and 1650°C isotherms generated by equation (25) are shown. For purposes of comparison the data of Hilty and Crafts<sup>12</sup> obtained at these temperatures is also displayed. Their investigation involved rotating furnace heats made in magnesia crucibles under an argon atmosphere. The materials used were electrolytic iron, ferrous sulphide and ferric oxide.

Both the present data and that of Hilty and Crafts<sup>12</sup> show that substantial additions of sulphur, in excess of 0.2%, increase the solubility of oxygen in liquid iron considerably. However, Hilty and Crafts<sup>12</sup> show a slight decrease in oxygen content with small sulphur additions, up to about 0.1%, and they speculate that this results from a tendency to immiscibility in the Fe-S system itself. This study revealed no such decrease, a continuous increase being observed, albeit at a rate increasing with increasing sulphur content.

#### E. Interaction Coefficients

For dilute multicomponent solutions in solvent 1 the activity coefficient of solute 2 is given by the equation<sup>23</sup>:

$$\ln \gamma_2 = \ln \gamma_2^0 + \epsilon_2^{(2)} X_2 + \epsilon_2^{(3)} X_3 + \epsilon_2^{(4)} X_4 + \dots \quad (26)$$

where:  $\gamma_2 = a_2/X_2$

and the interaction coefficient

$$\epsilon_2^{(3)} = \left( \frac{\partial \ln \gamma_2}{\partial X_3} \right)_{X_1 \rightarrow 1} \text{ etc.}$$

where:  $X$  = mole fraction

Note that in this section  $\%O$  and  $\%S$  are replaced by  $\%O$  and  $\%S$  for the sake of simplicity and clarity.

If the infinitely dilute solution is taken as the reference state then  $\gamma_2^0 = 1$  and for the ternary system Fe-O-S,

$$\ln \gamma_O = \epsilon_O^O X_O + \epsilon_O^S X_S \quad (27)$$

Using weight percent and common logarithms this relation becomes:

$$\log f_O = e_O^O \%O + e_O^S \%S \quad (28)$$

where

$$f_O = a_O / \%O \text{ and } e_O^S = \left( \frac{\partial \log f_O}{\partial \%S} \right)_{\%Fe \rightarrow 100}$$

The two interaction coefficients are related by the following equation<sup>24</sup>:

$$\epsilon_O^S = 230 (M_S / M_{Fe}) e_O^S + (M_{Fe} - M_S) / M_{Fe} \quad (29)$$

where:  $M_S$  = molecular weight of sulphur

$M_{Fe}$  = molecular weight of iron

Substituting the numerical values of  $M_S$  and  $M_{Fe}$  we have:

$$\epsilon_O^S = 132 e_O^S + 0.43 \quad (30)$$

When sulphur is added to a binary solution of oxygen in liquid iron the chemical potential of oxygen is increased by the quantity  $F_O^{XS}$ ; the partial molal free energy of oxygen due to the addition of sulphur

$$F_O^{XS} = RT\varepsilon_{O^S}X_S \quad (31)$$

Corresponding enthalpy and entropy terms can be defined<sup>25</sup> as follows:

$$H_O^{XS} = \eta_{O^S}X_S \quad (32)$$

$$\text{where: } \eta_{O^S} = \left( \frac{\partial H_O^{XS}}{\partial X_S} \right)_{X_{Fe} \rightarrow 1}$$

$$S_O^{XS} = \sigma_{O^S}X_S \quad (33)$$

$$\text{where: } \sigma_{O^S} = \left( \frac{\partial S_O^{XS}}{\partial X_S} \right)_{X_{Fe} \rightarrow 1}$$

It follows that:

$$F_O^{XS} = RT\varepsilon_{O^S}X_S = H_O^{XS} - TS_O^{XS} = \eta_{O^S}X_S - T\sigma_{O^S}X_S \quad (34)$$

and

$$RX_S d\varepsilon_{O^S}/d\left(\frac{1}{T}\right) = \frac{d(F_O^{XS}/T)}{d\left(\frac{1}{T}\right)} = H_O^{XS} = \eta_{O^S}X_S \quad (35)$$

Using the experimental data and a number of the above equations,  $e_{O^S}$  and  $\varepsilon_{O^S}$  can be found as functions of temperature and the value of  $\eta_{O^S}$  can be deduced.

1. Calculation of the Interaction Coefficients  $e_O^S$  and  $\epsilon_O^S$  as Functions of Temperature.

For dilute solutions of sulphur and oxygen in liquid iron, it will be shown below that:

$$e_O^S = -(\frac{d\log\%O}{d\%S}) [1 + 2.3\%Oe_O^O] \quad (36)$$

Also the following equation representing the surface of the miscibility gap was generated.

$$T = \frac{D}{(\log\%O - C)} + [A + (B/D)(\log\%O - C)]\%S \quad (37)$$

Where A, B, C, and D are constants the values of which are known (see equations 24 and 25).

By use of these two equations,  $e_O^S$  can be found as a function of temperature.

Consider a dilute solution of oxygen and sulphur in liquid iron. As the sulphur content tends toward zero the equilibrium between liquid iron and the oxide slag phase, which contains only a small quantity of sulphur, may be represented by the equation:



The equilibrium constant

$$K = \frac{(a_{\text{Fe}} \cdot a_{\text{O}})}{a_{\text{FeO}}} \quad (40)$$

Now  $a_{\text{Fe}}$  is approximately equal to 1 and  $a_{\text{FeO}} \rightarrow 1$  as  $\%S \rightarrow 0$ .

Thus 
$$K = f_O \cdot \%O \quad (41)$$

where  $f_O$  is the activity coefficient of oxygen

Hence, 
$$\log f_O = \log K - \log \%O \quad (42)$$

Now from (28) above:

$$\log f_O = e_O^O \cdot \%O + e_O^S \cdot \%S$$

Equating

$$\log K - \log \%O = e_O^O \cdot \%O + e_O^S \cdot \%S \quad (43)$$

and

$$e_O^S = - \frac{d}{d\%S} [-\log K + \log \%O + e_O^O \%O]_T \quad (44)$$

$$e_O^S = - \left[ \frac{d(\log \%O + e_O^O \%O)}{d\%S} \right]_T \quad (45)$$

or

$$e_O^S = - \left[ \frac{d \log \%O}{d\%S} + e_O^O \frac{d\%O}{d\%S} \right]_T \quad (46)$$

$$e_O^S = - \left[ \frac{d \log \%O}{d\%S} + e_O^O \cdot \%O \frac{d\%O}{d\%S} \cdot \frac{1}{\%O} \right]_T \quad (47)$$

Therefore,

$$e_O^S = - \left( \frac{d \log \%O}{d\%S} \right)_T [1 + 2.3\%O e_O^O]_T \quad (48)$$

which is equation (36) given above.

Rearrangement of equation (37) gives:

$$\begin{aligned} & [-CT - D + AC \%S - (BC^2/D)\%S] + \\ & + \log \%O [T - A \%S + 2(BC/D)\%S] - \\ & - (\log \%O)^2 [(B/D)\%S] = 0 \end{aligned} \quad (49)$$

Differentiating with respect to  $\%S$ , at constant temperature, and rearranging yields:

$$\left(\frac{d \log \%O}{d \%S}\right)_T = \frac{\left[\frac{B}{D}(\log \%O)^2 + \left(A - \frac{2BC}{D}\right) \log \%O + \frac{BC^2}{D} - AC\right]}{\left[T - A \%S + \frac{2BC}{D} \%S - \frac{2B}{D} \%S \log \%O\right]} \quad (50)$$

And as  $\%S$  tends towards 0,

$$\left(\frac{d \log \%O}{d \%S}\right)_{T, \%S \rightarrow 0} = \frac{1}{T} \left[ (B/D) (\log \%O)^2 + (A - 2BC/D) \log \%O + BC^2/D - AC \right] \quad \dots (51)$$

Replacing the constants A, B, C, and D with their numerical values:

$$\left(\frac{d \log \%O}{d \%S}\right)_{T, \%S \rightarrow 0} = 1/T \left[ -192 (\log \%O)^2 + 247 \log \%O + 530 \right] \quad (52)$$

Substitution of (52) in (36) gives:

$$e_O^S = (1/T) [1 + 2.3e_O^0 \%O] [192 (\log \%O)^2 - 247 \log \%O - 530] \quad (53)$$

$e_O^0$  is believed to be relatively insensitive to temperature variation<sup>22</sup> and  $\%O$  is known as a function of temperature for oxygen saturated liquid iron. Hence  $e_O^S$  may be found for any temperature between 1450°C and 1700°C. Figure 13 shows  $e_O^S$  plotted against the reciprocal of the absolute temperature



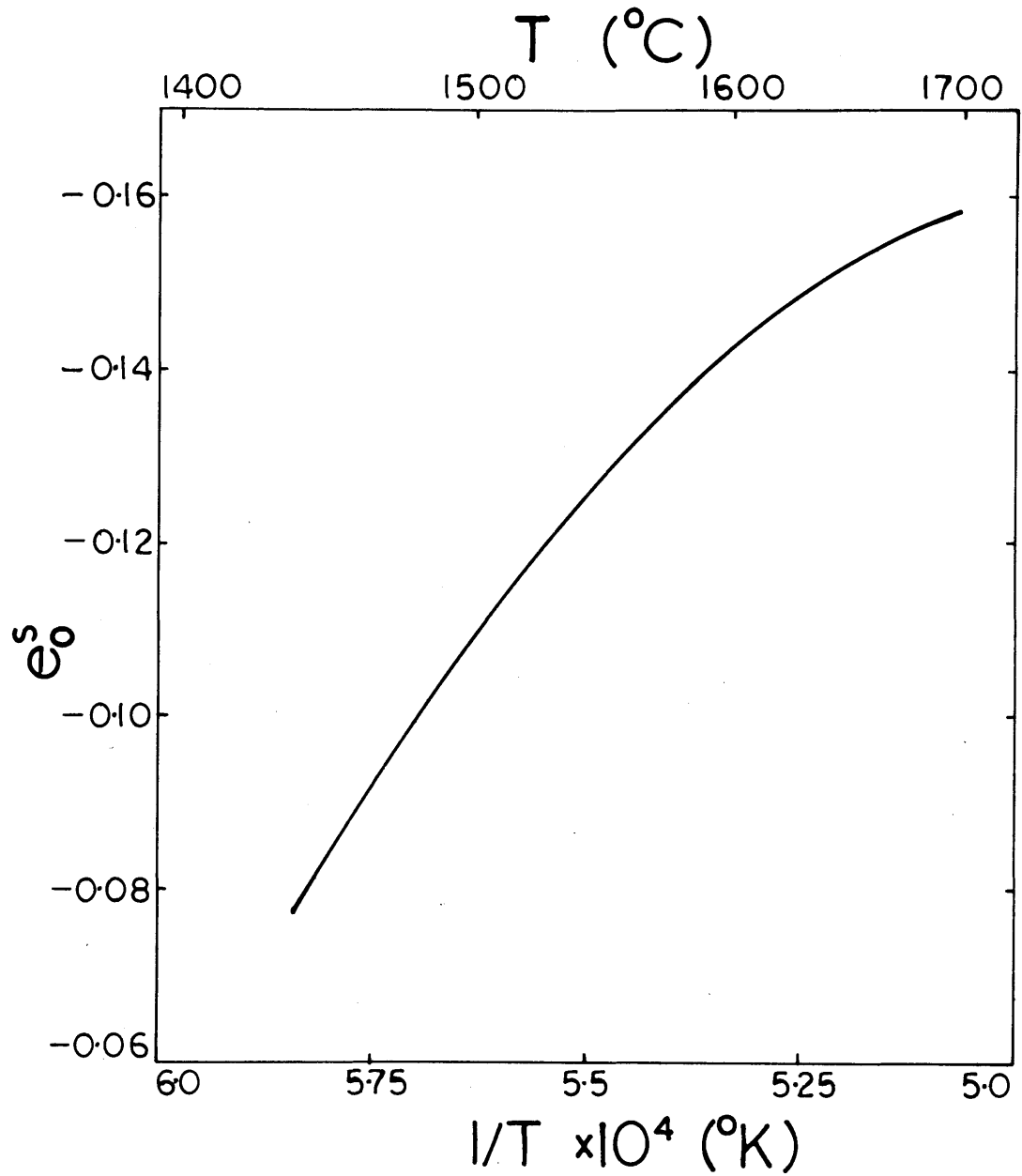


Figure 13. Interaction coefficient  $e_0^S$  as a function of reciprocal temperature (from equation 53).

using a value of  $-0.2$  for  $e_O^0$ . It can be seen that  $e_O^S$  doubles in value from  $-0.08$  to  $-0.16$ , over the temperature range  $1450^\circ\text{C}$  to  $1700^\circ\text{C}$ .

Substitution of (53) in (30) yields:

$$\epsilon_O^S = 132[1+2.3e_O^0\%O][192(\log\%O)^2-247\log\%O-530](1/T)+0.43 \dots\dots(54)$$

2. Calculation of  $\eta_O^S$ .

Knowing  $\epsilon_O^S$  as a function of temperature  $\eta_O^S$  can easily be found. From (33) we have:

$$RX_S \frac{d\epsilon_O^S}{d\left(\frac{1}{T}\right)} = \eta_O^S X_S$$

Therefore,

$$\eta_O^S = R \frac{d\epsilon_O^S}{d\left(\frac{1}{T}\right)} \quad (55)$$

Deriving (30) with respect to  $\frac{1}{T}$

$$\frac{d\epsilon_O^S}{d\left(\frac{1}{T}\right)} = 132 \frac{de_O^S}{d\left(\frac{1}{T}\right)} \quad (56)$$

From Figure 13 at  $1600^\circ\text{C}$

$$\frac{de_O^S}{d\left(\frac{1}{T}\right)} = 800 \text{ (}^\circ\text{C)}$$

Therefore,

$$\eta_O^S(1600^\circ\text{C}) = 210 \text{ K-cal/gm-mole.}$$

## VIII. SUMMARY AND CONCLUSIONS

The location of the miscibility gap in the liquid region of the Fe-FeO-FeS system close to the iron corner of the phase diagram was investigated. The method used involved homogenization of an Fe-O-S melt in the one phase region followed by cooling; the temperature at which the slag phase separated out of the homogeneous liquid iron pinpointed a spot on the surface of the miscibility gap. Supersaturation with respect to the slag phase could affect the accuracy of such a technique and so a check was carried out using simple Fe-O melts for which reliable equilibrium data exist. The solubility of oxygen in undercooled iron was also measured in the course of these experiments.

According to this study the solubility of oxygen in liquid iron, from 1340°C to 1730°C, is best represented by the equation:

$$\log \%O = -5750/T + 2.43 \quad (9)$$

This equation agrees with the well established equation of Taylor and Chipman<sup>7</sup> within the limits of experimental accuracy and is regarded as substantial evidence for the accuracy of the experimental technique itself.

The form of the miscibility gap surface in the Fe-FeO-FeS system, over a composition range of 0% to 0.5% S and 0.15% to 0.30% O was expressed as a function of the absolute temperature as follows:

$$T = -5750/(\log \%O - 2.43) + \%S[-684 - 192(\log \%O - 2.43)]$$

.....(25)

This equation shows that sulphur increases the solubility of oxygen in liquid iron at a rate which increases as the sulphur content builds up. The equation was also used in the calculation of the interaction coefficient  $e_O^S$ , the value of which was found to decrease from -0.08 at 1450°C to -0.16 at 1700°C.

PART II

INCLUSION FORMATION

## IX. LITERATURE SURVEY

A. On Non-Metallic Inclusions

Over the years a number of excellent summary articles and books on the subject of non-metallic inclusions have appeared in the literature<sup>28-32</sup> the most recent being a three volume report by Kiessling and Lange<sup>33</sup>. Only the work on sulphide inclusions and in particular on inclusions in the Fe-S-O system will be considered in any detail herein.

Until Wohrman<sup>32</sup> pointed out that sulphide inclusions are soluble in liquid iron, they were thought to be suspended particles. Wohrman also found that the size of inclusions increased with decreasing solidification rate. Many workers, including Benedicks and Lofquist<sup>30</sup>, and Sims and Lilliequist<sup>34</sup> accepted that iron sulphide tends to form continuous networks at primary grain boundaries or in the interdendritic fillings. This tendency is explained by Sims<sup>28</sup> in the following way. Since the Fe-S system freezes in the eutectic manner the sulphur must concentrate in the liquid, by segregation, until the eutectic composition is reached before any sulphide can form. Thus the sulphides will be located at the primary grain boundaries and interdendritic fillings where the last liquid solidifies. Sims, Saller and Boulger<sup>35</sup> classified sulphides, in deoxidized steels, into three groups: Type I, a globular form found in silicon killed steel; Type II, a grain boundary eutectic, typical in steels deoxidized with small amounts of

aluminum, zirconium or titanium; and Type III, angular sulphides common in strongly deoxidized steel containing residual aluminum and zirconium. Many explanations have been put forward to explain the formation of the three types. Recently, Dahl, Hengstenberg and Duren<sup>36</sup> suggested that they are all results of specific modifications to the Fe-MnS quasi-binary in the Fe-MnO-MnS system, produced by the alloying affects of the deoxidizer. Van Vlack and his co-workers<sup>37,38</sup> pointed out that the shape of the sulphide inclusions can be affected by changes in interfacial energies produced by addition of oxygen, aluminum or manganese. Crafts and his associates<sup>39,40</sup> have proposed a classification of oxide and sulphide inclusions into five types; silicate, eutectic, galaxy, alumina and peritectic. They explained the formation of these types by use of schematic solidification diagrams and supported their interpretations on the basis of micrographic analyses. Their treatment of the Fe-FeS-FeO system will be considered in more detail below.

#### B. On the Fe-FeS-FeO Phase Diagram

The importance of the phase diagram for the understanding of inclusion formation has long been recognized. In fact Benedicks and Lofquist<sup>30</sup> and also Wentrup<sup>31</sup> pointed out that all oxide and sulphide inclusions, excluding mechanically entrained matter, must result from specific modifications of the basic equilibria of the Fe-S-O system. The part of the diagram of particular interest is the Fe-FeS-FeO corner, the

liquidus surface of which plays a major role in determining the solidification paths of alloys in this system.

The three contiguous binary diagrams are of interest in establishing the ternary diagram. The Fe-FeO diagram is well established<sup>41</sup> and exhibits a wide solubility gap between liquid iron and liquid wustite as its dominant feature. The Fe-FeS diagram is of the eutectic type<sup>42,43</sup> with the eutectic point quite close to the sulphide phase. The binary FeO-FeS, while it is less well established, is thought to be of the simple eutectic type and liquidus surface has been defined.<sup>44</sup>

Qualitative sketches of the ternary system Fe-FeS-FeO were published by Benedicks and Lofquist<sup>30</sup>, and also Wentrup<sup>31</sup>, before Vogel and Fulling<sup>45</sup> made the first experimental determination. Their diagram, while only semi-quantitative, being established by a few observations mainly along two quasi-binary sections, resembles the later more accurate diagrams of Crafts and Hilty<sup>12</sup> and of Schurmann and von Hertwig<sup>46</sup> in all its major features. Crafts and Hilty<sup>12</sup> equilibrated mixtures of FeS and Fe<sub>2</sub>O<sub>3</sub> powders in iron crucibles by suspending them in a vertical-tube globar furnace in which an argon atmosphere was maintained. After two hours the samples were water quenched and then sectioned for chemical analysis and metallographic examination. The diagram built up from the results of these experiments is shown in Figure 14. The diagram is dominated by the miscibility gap in the liquid which extends from the Fe-FeO binary as far as 21.5 pct sulphur at an oxygen level of approximately 6 pct. The minimum temperature or plait point of



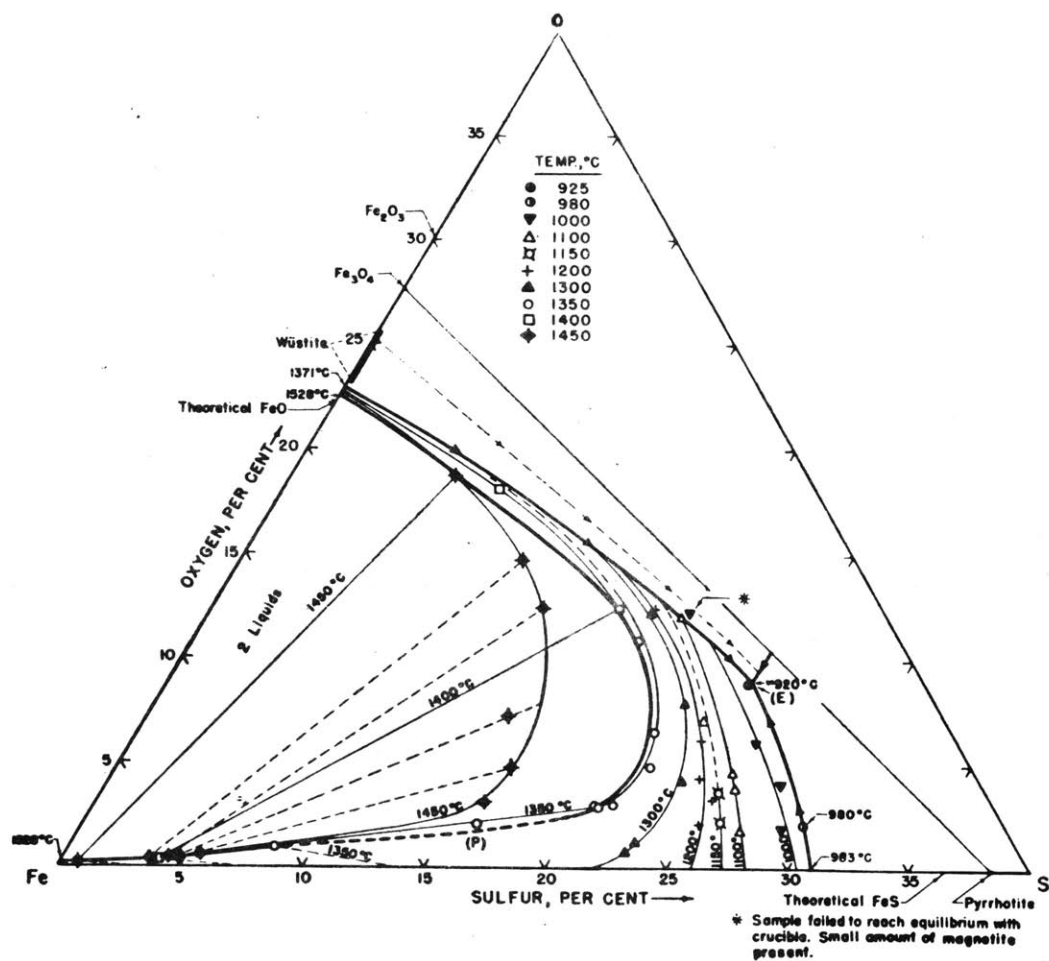


Figure 14. Liquidus surface of the Fe-FeO-FeS system according to Hilty and Crafts.<sup>12</sup>

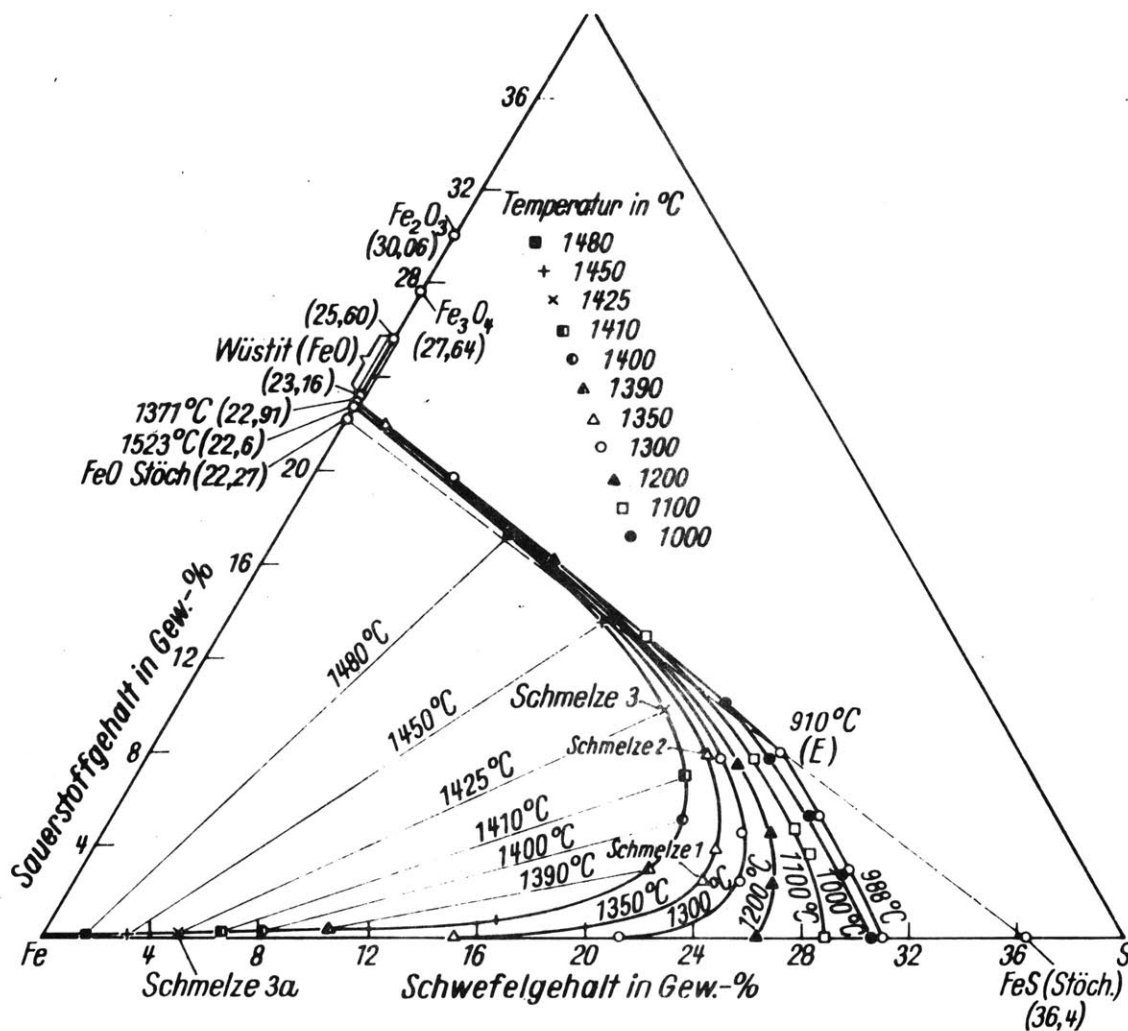


Figure 15. Liquidus surface of the Fe-FeO-FeS system according to Schurmann and von Hertwig.<sup>46</sup>

the miscibility gap is located at approximately 81.5 pct iron, 16.5 pct sulphur 2 pct oxygen and 1345°C. The pseudobinary eutectic lines, extending out from the eutectic points on the Fe-FeO, Fe-FeS and FeO-FeS binaries meet in a ternary eutectic point at 67 pct iron, 24 pct sulphur, 9 pct oxygen and approximately 920°C. Schurmann and von Hertwig<sup>46</sup> used the same technique of Hilty and Crafts<sup>12</sup>. Ol'Shanskii et al<sup>47,48</sup> determined the ternary eutectic composition and established the 1140°C, 1290°C and 1400°C isotherms but gave no tie-lines. The features of the diagrams and their differences are discussed in greater detail in Chapter XI.

### C. Inclusion Formation in the System Fe-FeS-FeO

Crafts and Hilty<sup>39</sup> used the ternary equilibrium diagram, which they had found experimentally, to explain the origin of inclusions in Fe-S-O alloys. Their schematic diagrams, Figures 16 and 17, show the solidification paths of two alloys superimposed on basal plane projections of the pseudobinary eutectic lines and the intersection of the miscibility gap with the iron liquidus surface. Figure 16 depicts an alloy, composition A, of a relatively high oxygen to sulphur ratio given by line I. Solidification commences when the temperature falls to that of the iron liquidus surface at point A. Further cooling results in the deposition of substantially pure iron, the composition of the liquid moving from A to c, where the miscibility gap is encountered. At this temperature a second liquid of composition d appears and as cooling proceeds there

is further deposition of iron from c to f together with a coprecipitation of oxide-rich liquid from d to g. On further cooling the oxide rich liquid moves along line I from g to h precipitating minor amounts of metal. Point h is on the iron-iron oxide pseudobinary eutectic line and as the temperature continues to fall the oxide rich liquid moves from h to E as coprecipitation of wustite and small quantities of metal occur. At point E freezing is completed with the appearance of the ternary eutectic of sulphide, oxide and minor amounts of metallic iron. By the time point d was reached solidification of the metal had been almost completed so that many of the droplets of oxide rich liquid, coprecipitated along with metal in the region cdgf would be enclosed by the growing metal phase. This mechanism would result in a metal matrix with small droplets of oxide rich inclusions located both at the grain boundaries and scattered randomly among them.

Figure 17 illustrates the solidification of an alloy, of composition B, with a relatively low O/S ratio given by line II. Crafts and Hilty<sup>39</sup> explained that as the alloy cools it splits up into two liquid phases, not indicated on the diagram, whose compositions are given approximately by the intercept of the appropriate isotherms with the tie-line ij. As the temperature falls to a point where the miscibility gap intercepts the metal liquidus surface, liquid i starts to precipitate iron and more second liquid phase of a composition given by point j. The solidification path from this point on is closely related to that of alloy A, Figure 16, except that at point n, on the

pseudobinary eutectic line, FeS and Fe precipitate from the sulphide rich liquid phase instead of wustite and iron as was the case for alloy A. Crafts and Hilty maintain that by the time point m is reached in Figure 17 the alloy consists of a spongy agglomerate of metal crystals, the individual crystals being more or less completely enveloped by liquid of composition l and that the crystals themselves contain droplets of liquid varying in composition from j to l. This mechanism is considered responsible for the intergranular inclusions observed in alloys of low O/S ratio.

The other possible freezing mechanism, which operates when the oxygen to sulphur ratio is so low that the miscibility gap is avoided entirely, is the simplest of the three. Initial freezing of the metal is followed by the sulphide-metal pseudobinary eutectic reaction and finally the ternary eutectic reactions. The inclusions in this case are entirely intergranular sulphides.

Thus, Crafts and Hilty<sup>39</sup> propose three possible mechanisms for solidification in the ternary Fe-FeS-FeO system. Mechanism 1, occurring when O/S ratio is greater than that corresponding to the ternary eutectic compositions, leads to globular inclusions, both random and intergranular, in which the wustite phase predominates. Mechanism 2, for an O/S ratio between those of the ternary eutectic and the plait point P, leads to intergranular sulphide rich inclusions with a few sulphide rich inclusions randomly distributed. Mechanism 3, for O/S ratios less than that of the plait point P gives simple intergranular sulphides.

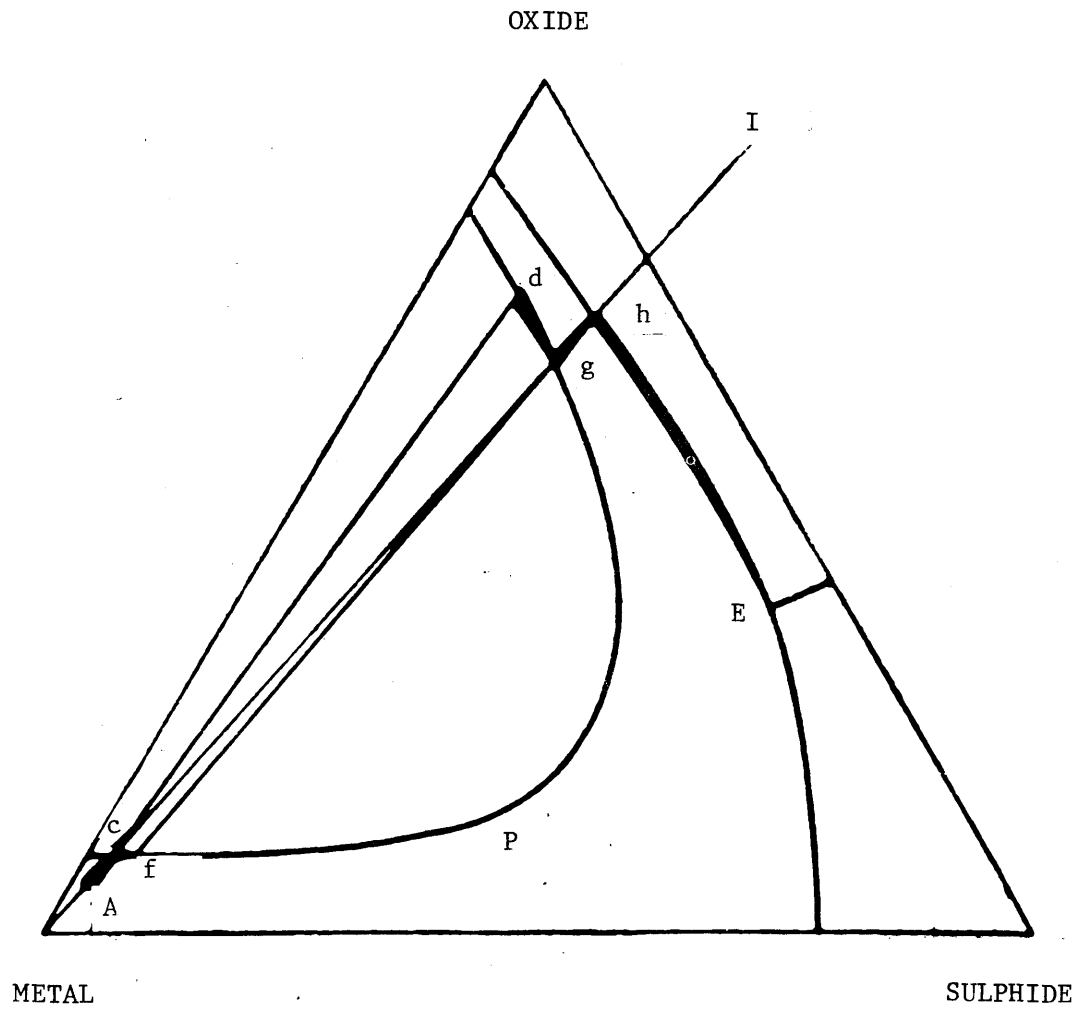


Figure 16. Schematic representation of inclusion formation in the Fe-FeO-FeS system at a high O/S ratio according to Crafts and Hilty.<sup>39</sup>

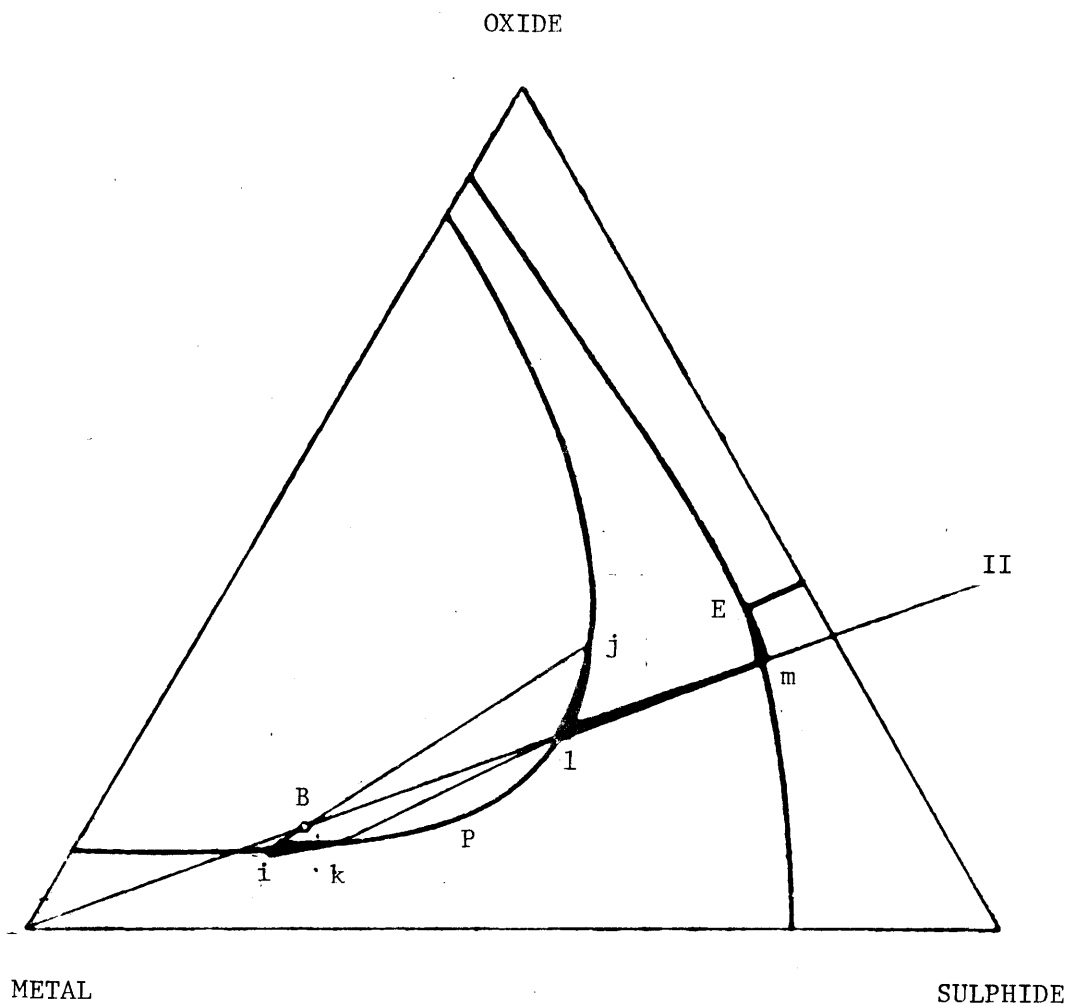


Figure 17. Schematic representation of inclusion formation in the Fe-FeO-FeS system at a low O/S ratio according to Crafts and Hilty.<sup>39</sup>

#### D. On Solute Redistribution in Dendritic Solidification

During the solidification of Fe-S-O alloys the separation of new solid and liquid phases leads to segregation of sulphur and oxygen. This solute redistribution is of paramount importance in the formation of inclusions.

The classical quantitative treatment of solute redistribution in binary alloys has been performed by Gulliver<sup>49</sup>, Scheil<sup>50</sup> and Pfann<sup>51</sup>, among others. A closed volume element is considered during "non-equilibrium solidification" and when a constant partition ratio is used the following equation, sometimes called the Scheil equation, is generated:

$$C_S^* = kC_O(1 - f_S)^{k-1} \quad (57)$$

where:  $C_S^*$  = interface composition of the solid when the weight fraction of the solid within the considered volume element is  $f_S$  (wt. fraction or wt. pct)

$k$  = equilibrium partition ratio

$C_O$  = initial alloy composition within the volume element (wt. fraction or wt. pct)

The assumptions used in the derivation of the above equation are as follows:

1. No mass flow in or out of the volume element.
2. Negligible undercooling before nucleation, or from effects of kinetics or curvature.
3. Diffusion in the liquid is complete.
4. Diffusion in the solid is negligible.
5. The equilibrium partition ratio applies at the surface and is constant throughout freezing.



According to Brody and Flemings<sup>52</sup> the first three of these assumptions are justified for a wide range of boundary conditions and they support this statement with experimental evidence<sup>53</sup>. However, limited diffusion in the solid may occur and constancy of the partition ratio is not always an accurate assumption. Accordingly, they developed an analytical solution and a numerical analysis procedure to take these factors into account.

In the case of multicomponent systems the interactions between elements may affect the distribution coefficient. Kuwabara<sup>54</sup> has developed a thermodynamic model for the treatment of this case which allows calculation of the true  $k$  values.

## X. OUTLINE OF INVESTIGATION

Although it has long been recognized that most inclusions in steel are either oxides or sulphides, or a combination of both, there has been surprisingly little research into inclusion formation in the basic iron-iron oxide-iron sulphide system. The present study was undertaken, therefore, to shed some light on the solidification of iron-sulphur-oxygen alloys and the attendant mode of formation of the sulphide and oxide inclusions.

To this end, and based on the existing phase diagram of the system, two possible models for solidification were set up. The first, bearing a close resemblance to the mode of solidification suggested by Crafts and Hilty<sup>39</sup>, follows a continuous series of equilibrium steps between phases which are completely homogeneous within themselves. The second model is based on the postulated continual entrapment and isolation of liquid rich in oxygen and sulphur, which is formed because of the miscibility gap in the liquid region of the phase diagram. The first model is referred to as "equilibrium" model and the second, the "isolation" model for the sake of brevity.

The models were used to predict the composition and morphology of the inclusions formed during solidification of alloys having a range of oxygen/sulphur ratios. Small samples of the alloys of various compositions, melted in a levitation furnace, were solidified and the resulting microstructures were examined. Comparison of the results with those predicted by the models allowed the selection of the model best fitting the real case.

## XI. SOLIDIFICATION MODELS

A. The Fe-FeO-FeS Phase Diagram

The solidification models described in this work are based on the ternary equilibrium diagram of the Fe-FeO-FeS system. The validity and accuracy of the diagram is, therefore, worthy of consideration.

Two more or less complete determinations of the liquidus surface have been made as well as a number of more limited observations. Hilty and Crafts<sup>12</sup>, and Schurmann and von Hertwig<sup>46</sup> used virtually identical techniques, the results of which are shown in Figures 14 and 15 respectively. The diagrams show the same features, i.e., a large miscibility gap extending from the Fe-FeO binary and three pseudobinary eutectic lines from the Fe-FeO, Fe-FeS and FeO-FeS binary eutectic points meeting at a ternary eutectic point. Two points of considerable importance are the plait point of the miscibility gap and the ternary eutectic point. The plait point corresponds to the location of the lowest temperature on the critical curve separating liquids  $L_1$  and  $L_2$ . The locations of these points, given by the various workers, are shown in Table 5.

It can be seen from the table that, whilst there is fair agreement on the location of the ternary eutectic, the position of the plait point is in some doubt. All three values listed are to some extent estimates; that of Vogel and Fulling<sup>45</sup> having the least data to back it up. The estimates of Hilty

Table 5  
The Fe-FeO-FeS Phase Diagrams

<u>source</u>	<u>wt.%Fe</u>	<u>wt.%S</u>	<u>wt.%O</u>	<u>O/S</u>	<u>T(°C)</u>
(a) Location of the ternary eutectic point.					
Hilty & Crafts <sup>12</sup>	67.0	24.0	9.0	0.375	920
Schurmann & von Hertwig <sup>46</sup>	68.8	23.2	8.0	0.345	910
Ya I. Ol'Shanskii <sup>47</sup>	67.5	25.0	7.5	0.300	920
(b) Location of the plait point.					
Hilty & Crafts <sup>12</sup>	81.5	16.5	2.0	0.121	1340
Schurmann & von Hertwig <sup>46</sup>	82.9	16.4	0.7	0.043	1382
Vogel & Fulling <sup>45</sup>	77.8	20.9	1.3	0.062	1320

and Crafts<sup>12</sup> and Schurmann and von Hertwig<sup>46</sup> show large discrepancies in the temperatures and oxygen levels; the latter leading to a large difference in the O/S ratio. This ratio is of some importance when solidification is considered and so the accuracy of the oxygen content must be taken into account. A detailed examination of the data of Hilty and Crafts<sup>12</sup> and Schurmann and von Hertwig<sup>46</sup> reveals that the differences in temperature and oxygen level recur throughout. This state of affairs is illustrated by Figure 18 which shows a plot of the sulphur content of the liquid iron, at the intersection of the miscibility gap and the iron liquidus surfaces, versus the

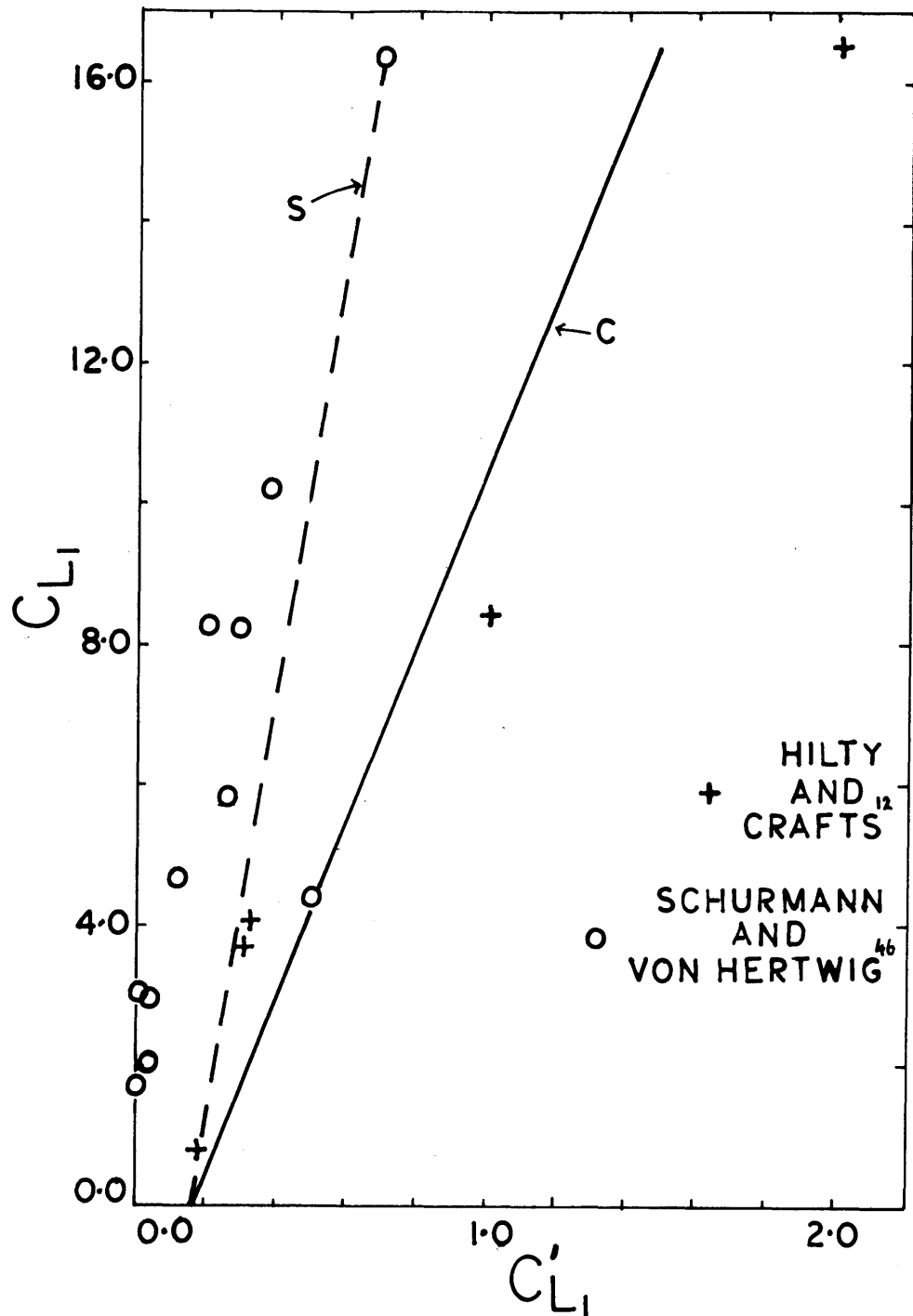


Figure 18. Sulphur content ( $C_{L1}$ ) versus oxygen content ( $C'_{L1}$ ) in liquid iron ( $L_1$ ) at the intersection of the miscibility gap and iron liquidus surfaces. Lines C and S are the linear interpolations of the data of Hilty and Crafts<sup>12</sup> and Schurmann and von Hertwig<sup>46</sup> respectively used as a basis of the solidification models.

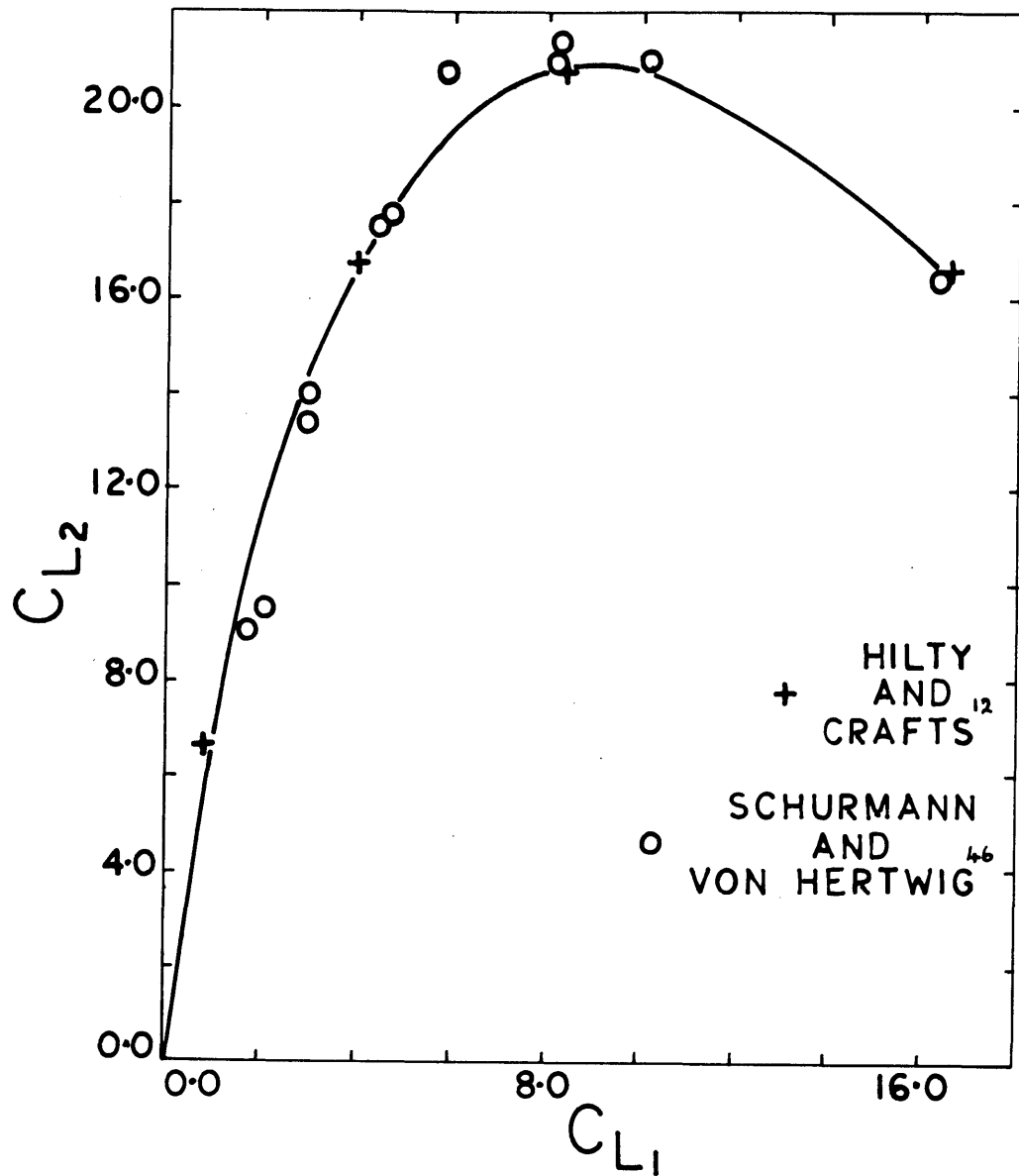


Figure 19. Sulphur content ( $C_{L_2}$ ) of the liquid slag phase ( $L_2$ ) versus the sulphur content ( $C_{L_1}$ ) of liquid iron ( $L_1$ ) at the intersection of the miscibility gap and iron liquidus surfaces. The line shown is the interpolation of the data used as a basis of the solidification models.

oxygen content of the same liquid. The two sets of data diverge widely and any such plot involving the oxygen content of either the liquid metal or slag shows the same behavior. On the other hand if the sulphur content of the liquid slag is plotted as a function of the sulphur content, of the liquid metal in equilibrium with it, both sets of data lie on the same line (see Figure 19). The differences in temperatures, as reported on the two phase diagrams, while significant, have a lesser effect on the models and as a result are not so important. A possible explanation for the discrepancies in oxygen contents is to be found in the method employed by Schurmann and von Hertwig<sup>46</sup>. They did not analyze either the slag or metal for oxygen but relied on the subtraction of the analyzed percentages of iron and sulphur from 100 to give the oxygen content. In all probability this is the major cause of the discrepancies between the two phase diagrams and for this reason the data of Hilty and Crafts<sup>12</sup> are considered the more reliable of the two. They are used as a basis for most of the detailed description of the solidification models except in certain cases where both phase diagrams are considered.

#### B. The Models

The object of the construction of the solidification models is to predict the composition and location of inclusions found in simple Fe-S-O alloys. The models are based on the ternary Fe-FeO-FeS phase diagram and are derived by means of a mass

balance applied to the phase equilibria together with some simplifying but reasonable assumptions. The Fe-FeO-FeS phase diagram is dominated by the liquid miscibility gap and the three-phase monotectic reaction associated with this gap has a major effect on the solidification of all iron melts having an O/S ratio greater than about 0.09. The derivation of the models is quite similar to that of the familiar Scheil equation<sup>50</sup> except that a three-phase equilibrium rather than a two-phase equilibrium is considered. The models differ in that two possible modes of behavior are taken into account during the progress of the monotectic reaction. Strictly speaking, only melts which encounter the miscibility gap are considered by the models outlined below. This is not a great restriction, however, as it encompasses most of the range of Fe-S-O alloys. Alloys having an O/S ratio less than 0.09 are considered qualitatively for the sake of completeness.

All symbols used in relation to the models are listed and defined in Table 6.

#### Model 1: The "Equilibrium" Solidification Model

A closed volume element of solidifying metal is considered just as in the derivation of the Scheil equation<sup>50</sup>. The following assumptions are used:

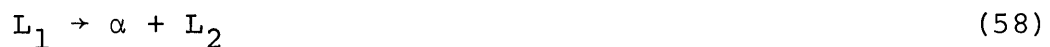
1. There is no mass flow in or out of the volume element.
2. Negligible undercooling is required before nucleation, of both solid iron and the liquid slag  $L_2$ , or is caused by kinetic or curvature effects.



3. Diffusion in the liquids is complete.
4. Equilibrium is maintained between the liquid metal ( $L_1$ ) and the liquid slag ( $L_2$ ).
5. There is no solubility of oxygen or sulphur in solid iron.

Assumptions (1), (2), and (3) are the same as those made in the derivation of the Scheil equation. Assumption (4) is the basis for the difference between this "equilibrium" model and Model 2, the "isolation" model. It means that the two liquid phases must remain in contact throughout the monotectic reaction. The validity of assumption (5) is discussed in Appendix E.

During solidification, the liquid metal phase,  $L_1$ , breaks down into relatively pure solid iron,  $\alpha$ , and a liquid slag phase,  $L_2$ , rich in oxygen and sulphur. That is to say:



A mass balance taking into account the compositions of these phases can be written in order to follow the progress of solidification. Figure 20 is of help in visualizing the mass balance.

Table 6

## Definition of Symbols

$\alpha$	solid iron phase
$L_1$	liquid iron phase
$L_2$	oxygen-sulphur rich liquid slag phase
$C_O, C'_O$	initial sulphur, oxygen content of the melt, wt.%
O/S	oxygen/sulphur ratio of a phase by weight
$C_\alpha, C'_\alpha$	sulphur, oxygen content of $\alpha$ , wt.%
$C_{L_1}, C'_{L_1}$	sulphur, oxygen content of $L_1$ , wt.%
$C_{L_2}, C'_{L_2}$	sulphur, oxygen content of $L_2$ , wt.%
$f_\alpha, f_{L_1}, f_{L_2}$	weight fraction of $\alpha, L_1, L_2$ within the volume element
$C^*_{L_2}, C'^*_{L_2}$	sulphur, oxygen content of $L_2$ at the $L_1/L_2$ interface, wt.%
$df_\alpha, df_{L_1}, df_{L_2}$	change in the weight fraction of $\alpha, L_1, L_2$ during a differential step in solidification
$dC_{L_1}, dC'_{L_1}$	change in the sulphur, oxygen content of $L_1$ during solidification of small quantity, $df_\alpha$ , of iron
$dC^*_{L_2}, dC'^*_{L_2}$	change in the sulphur, oxygen content of $L_2$ at the $L_1/L_2$ interface during solidification of a small quantity, $df_\alpha$ , of iron

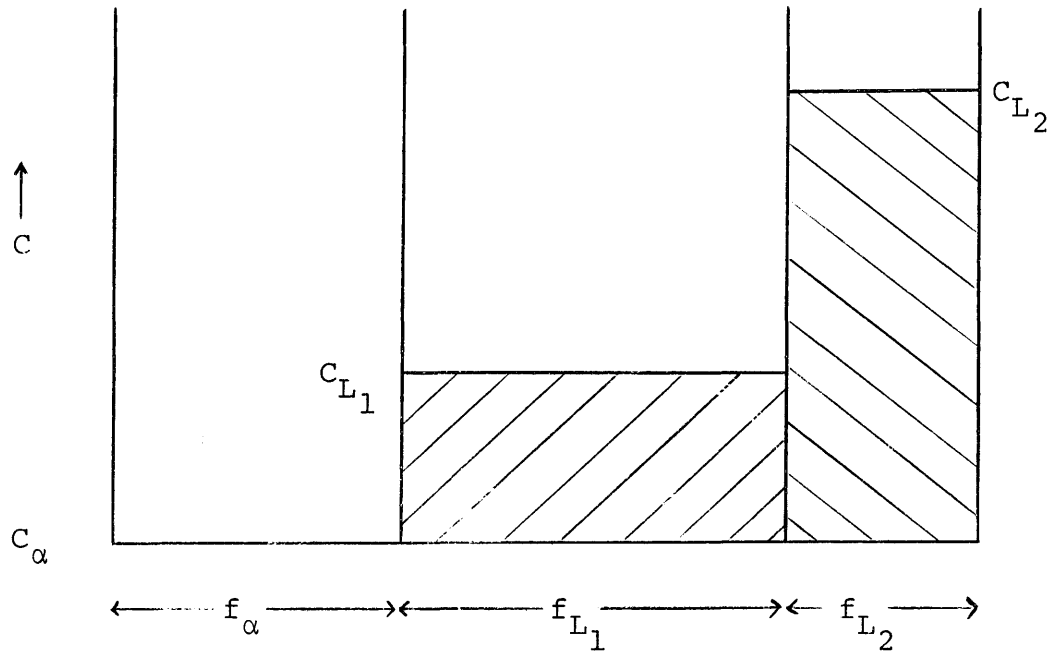


Figure 20. Composition and fraction of the three phases,  $\alpha$ ,  $L_1$  and  $L_2$  at a point in the monotectic three phase reaction.

The diagram is a schematic representation of the composition and fraction of each phase in the closed volume element during the monotectic reaction. Three such diagrams could be drawn; for sulphur, oxygen and iron, but one is sufficient for purposes of illustration.

In general, for sulphur

$$C_{\alpha} f_{\alpha} + C_{L_1} f_{L_1} + C_{L_2} f_{L_2} = C_0 \quad (59)$$

and for oxygen

$$C'_{\alpha} f_{\alpha} + C'_{L_1} f_{L_1} + C'_{L_2} f_{L_2} = C'_0 \quad (60)$$

Also

$$f_{\alpha} + f_{L_1} + f_{L_2} = 1 \quad (61)$$

(Note all symbols are defined in Table 6.)

$$\text{Since from assumption (5), } C_{\alpha} = C'_{\alpha} = 0 \quad (62)$$

$$C_{L_1} f_{L_1} + C_{L_2} f_{L_2} = C_0 \quad (63)$$

$$C'_{L_1} f_{L_1} + C'_{L_2} f_{L_2} = C'_0 \quad (64)$$

Solving for  $f_{\alpha}$ ,  $f_{L_1}$  and  $f_{L_2}$  in (61), (63) and (64)

$$f_{L_1} = \frac{C'_0 C_{L_2} - C_0 C'_{L_2}}{C'_{L_1} C_{L_2} - C_{L_1} C'_{L_2}} \quad (65)$$

$$f_{L_2} = \frac{C'_0 C_{L_1} - C_0 C'_{L_1}}{C_{L_1} C'_{L_2} - C'_{L_1} C_{L_2}} \quad (66)$$

$$f_{\alpha} = 1 - f_{L_1} - f_{L_2} \quad (67)$$

Also the initial and final conditions for the three phase monotectic reaction are known:

$$\text{Initial condition, } f_{\alpha} = 0, f_{L_1} = 1, f_{L_2} = 0 \quad (68)$$

$$\text{Final condition } f_{L_1} \text{ (or } f_{L_2} \text{)} = 0 \quad (69)$$

(The final state  $f_{L_1} = 0$  is used here and the alternate state  $f_{L_2} = 0$  is considered in Appendix G.)

If the tie lines connecting  $L_1$  and  $L_2$  are known as a function of temperature, then, for any given starting composition ( $C_0, C'_0$ ), the weight fractions of the three phases may be calculated as a function of composition, of either  $L_1$  or  $L_2$ , and as a function of temperature. A few tie lines are given by both Hilty and Crafts<sup>12</sup>, and Schurmann and von Hertwig<sup>46</sup>; intermediate tie lines and the corresponding temperatures were obtained by interpolation. A straight line interpolation was used from the Fe-FeO monotectic point, which is well defined, to the estimated plait point for three reasons, viz the data are close to linear, they are quite scattered, and there are not many data points. The data points and the straight line interpolation from both Hilty et al<sup>12</sup> and Schurmann et al<sup>46</sup> are shown in Figure 18. The actual values for the tie lines used in the models are listed in Appendix F.

It is of course quite possible that the miscibility gap does not intersect the iron liquidus surface in a straight line up to the plait point. In this case the position of the plait point becomes quite critical in deciding the behavior of the immiscible liquids  $L_1$  and  $L_2$ , and in fact the monotectic reaction may end with the consumption of the slag phase,  $L_2$ . The possibility is considered in greater detail in Appendix G.

A computer program, which is set out in Appendix H, was used to simulate the course of the three phase reaction, from  $f_{L_1} = 1$  to  $f_{L_1} = 0$ , for any initial composition on the intersection of the miscibility gap and iron liquidus surfaces. The program is based on equations (65), (66), and (67) and the

output lists  $f_{\alpha}$ ,  $f_{L_1}$  and  $f_{L_2}$  as functions of compositions of  $L_1$  and  $L_2$  and of the temperature.

The results of the program follow the same general pattern in all cases considered and they are illustrated here by reference to a particular melt of O/S ratio 0.16. Figure 21 shows a graph of the computer output;  $f_{\alpha}$ ,  $f_{L_1}$ ,  $f_{L_2}$  being plotted as a functions of the temperature. It can be seen that the  $L_1$  phase is consumed by the time the temperature falls to  $1360^{\circ}\text{C}$  at which point the O/S ratio of  $L_2$  reaches 0.16; the original melt O/S ratio. At this time the alloy consists of 90% pure solid iron and 10% liquid slag  $L_2$ . Taking into account the difference in scales used for  $f_{\alpha}$  and  $f_{L_2}$  in the graph, it is apparent that the rate of formation of  $\alpha$  is much greater than that of  $L_2$  for nearly all the range considered. In fact, inspection of the computer output reveals that the initial rate of  $\alpha$  formation is about three orders of magnitude greater than that of  $L_2$ .

Solidification of this type may also be followed qualitatively, but quite graphically, on a schematic phase diagram. The solidification of a melt, the O/S ratio of which is greater than that of the ternary eutectic point, is illustrated in this manner in Figure 22. The original composition of the melt is given by point a on the phase diagram and has an O/S ratio  $C_0/C'_0$  represented by line I. As the homogeneous liquid cools it reaches the temperature, for this composition, where the miscibility gap and iron liquidus surfaces intersect. At this point the three-phase

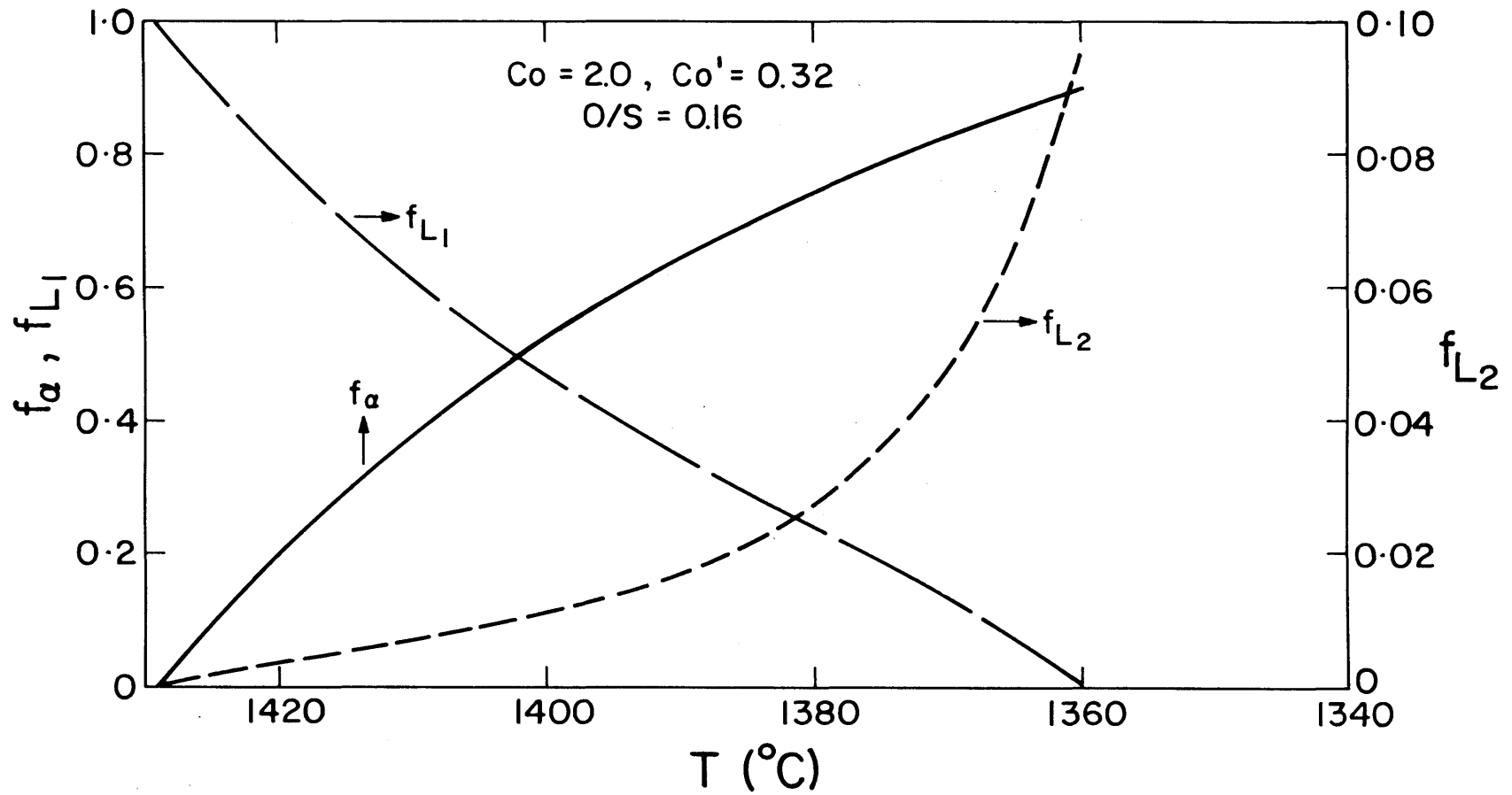


Figure 21. Fractions of iron ( $f_{\alpha}$ ),  $L_1$  ( $f_{L1}$ ) and  $L_2$  ( $f_{L2}$ ) versus temperature during the three-phase monotectic reaction according to the equilibrium solidification model.

monotectic reaction commences and pure iron ( $\alpha$ ) and liquid slag ( $L_2$ ) start to precipitate from the liquid ( $L_1$ ). As the temperature falls further  $L_1$  moves in composition from a to c, diminishing in quantity as it precipitates more iron and liquid  $L_2$ , the composition of which moves from b to d to maintain equilibrium according to the tie lines shown. By the time  $L_2$  reaches d, a point which has the same O/S ratio,  $C_0/C'_0$ , as the overall composition of the alloy,  $L_1$  is consumed. The same general pattern holds for all alloys in that on the arrival of  $L_2$  at position d, or its equivalent, the three-phase monotectic reaction is completed.

With the exhaustion of  $L_1$  and the completion of the monotectic reaction the computer simulation of solidification ends. The process of solidification from this point on may be followed quantitatively by a simple mass balance which is given detailed consideration in Appendix K. However, the events may be followed in a qualitative way by referring to Figure 22. As the temperature falls, at the end of the monotectic reaction,  $L_2$  deposits more iron and its composition moves across the iron liquidus surface maintaining a constant O/S ratio until one of the pseudobinary eutectic lines or the ternary eutectic point is reached. In Figure 22 the overall melt composition is such that the Fe-FeO pseudobinary is intersected at point f. The composition of the remaining liquid  $L_2$  which reaches the pseudobinary eutectic line, is governed therefore by the O/S ratio of the original melt. On further cooling  $L_2$  deposits FeO or FeS, depending on which



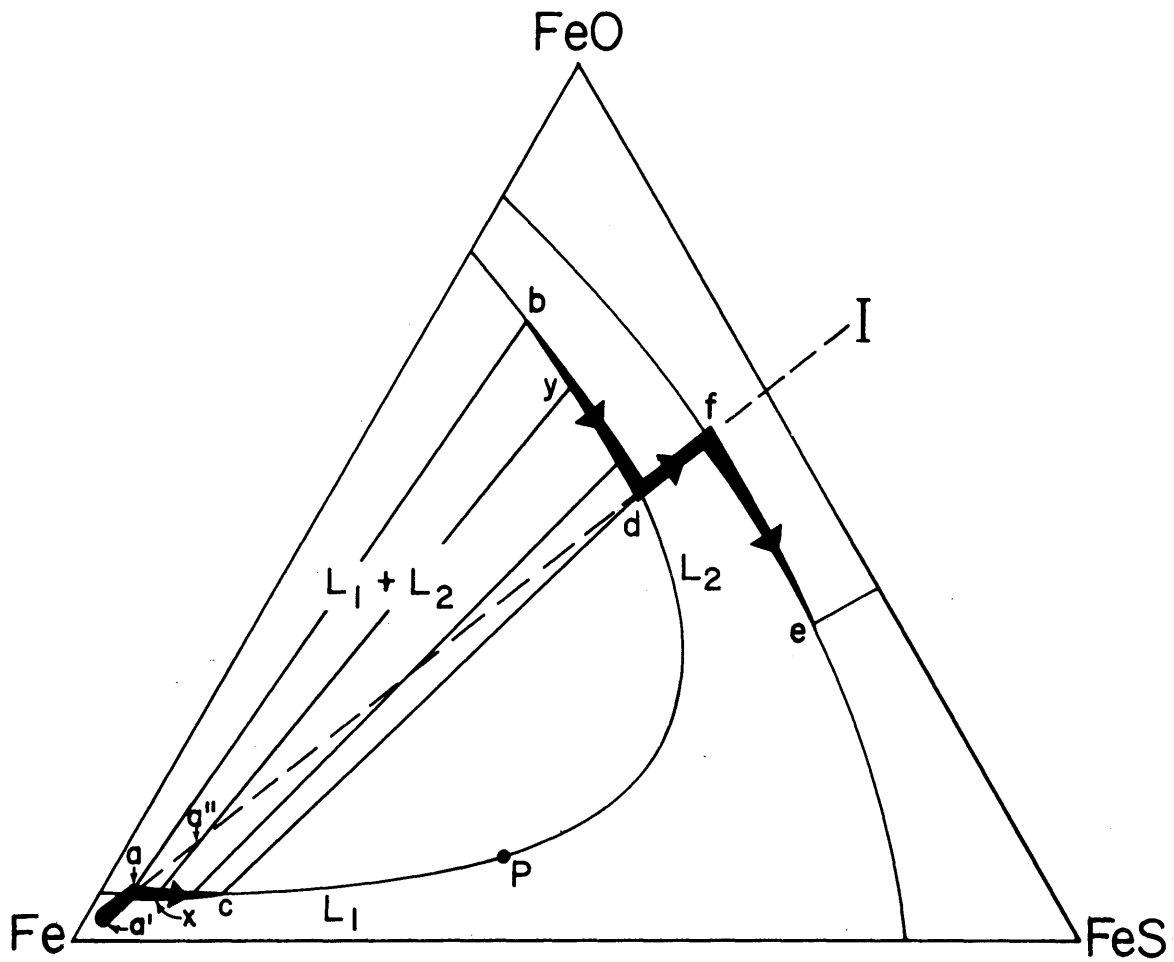


Figure 22. Schematic representation of inclusion formation in the Fe-FeO-FeS system according to the equilibrium solidification model.

pseudobinary eutectic is concerned, and minor quantities of solid iron; moving down the eutectic valley to where the last liquid solidifies as a ternary eutectic.

The inclusions in the solidified metal result from the freezing of the oxide-sulphide rich liquid  $L_2$  as it moves in composition from d to e. Consequently the composition of the inclusions is uniquely defined by the original O/S ratio of the melt. This is true for all alloys considered; the initial compositions of which correspond to some position on the intersection of the miscibility gap surface with the iron liquidus. It is also true for alloys richer or poorer in oxygen than those lying exactly on this line.

Alloys poorer in oxygen than those lying on the line of intersection, such as alloy a', reach the iron liquidus surface before they are saturated with oxygen. Thus they precipitate pure solid iron and the O/S ratio of the liquid is maintained until it reaches the miscibility gap at a. The freezing process from then on is just as was described above for alloy a, the only difference being that more iron and less included matter will be present in the final solidified material.

Now consider an alloy of composition a" which becomes saturated with oxygen before it cools to the iron liquidus and splits up into two liquids  $L_1$  and  $L_2$ . The composition of these liquids are defined by a tie line at a higher temperature than the tie lines shown in Figure 22. Cooling to the iron liquidus changes the compositions of the liquids to those given by the tie line xy. At this point precipitation

of iron begins and subsequent solidification is the same as described above for an alloy of composition a. In this case, however, the fraction of inclusions is greater but their composition is exactly the same. This is because the three phase reaction must end at the same point as it did for alloy a; the overall composition of the alloy having to remain inside the tie triangle formed by the composition coordinates of the solid iron,  $L_1$  and  $L_2$ . The extreme position that this triangle can assume is Fe-d-c which has line I through a", the original composition, as one of its sides. Consequently  $L_2$  leaves the miscibility gap at d just as it did in the case of alloy a.

In brief; the inclusions in Fe-S-O melts solidified according to the dictates of the "equilibrium" model all have the same compositions. These compositions are determined by the O/S ratios of the melts several of which are considered quantitatively in Appendix K. Figure 23 summarizes the results of this Appendix, showing the volume percent of FeO, FeS and ternary eutectic in the inclusions as a function of the O/S ratio of the melt. The particular curves shown are based on the interpolated data of Hilty and Crafts<sup>12</sup>. Since the inclusions are formed by the freezing of  $L_2$  at the end of the three-phase monotectic reaction they would be expected to form a continuous envelope around the iron dendrites.

It has been shown that under conditions of "equilibrium" solidification the intervention of the monotectic reaction does not change the O/S ratio of the liquid remaining at the

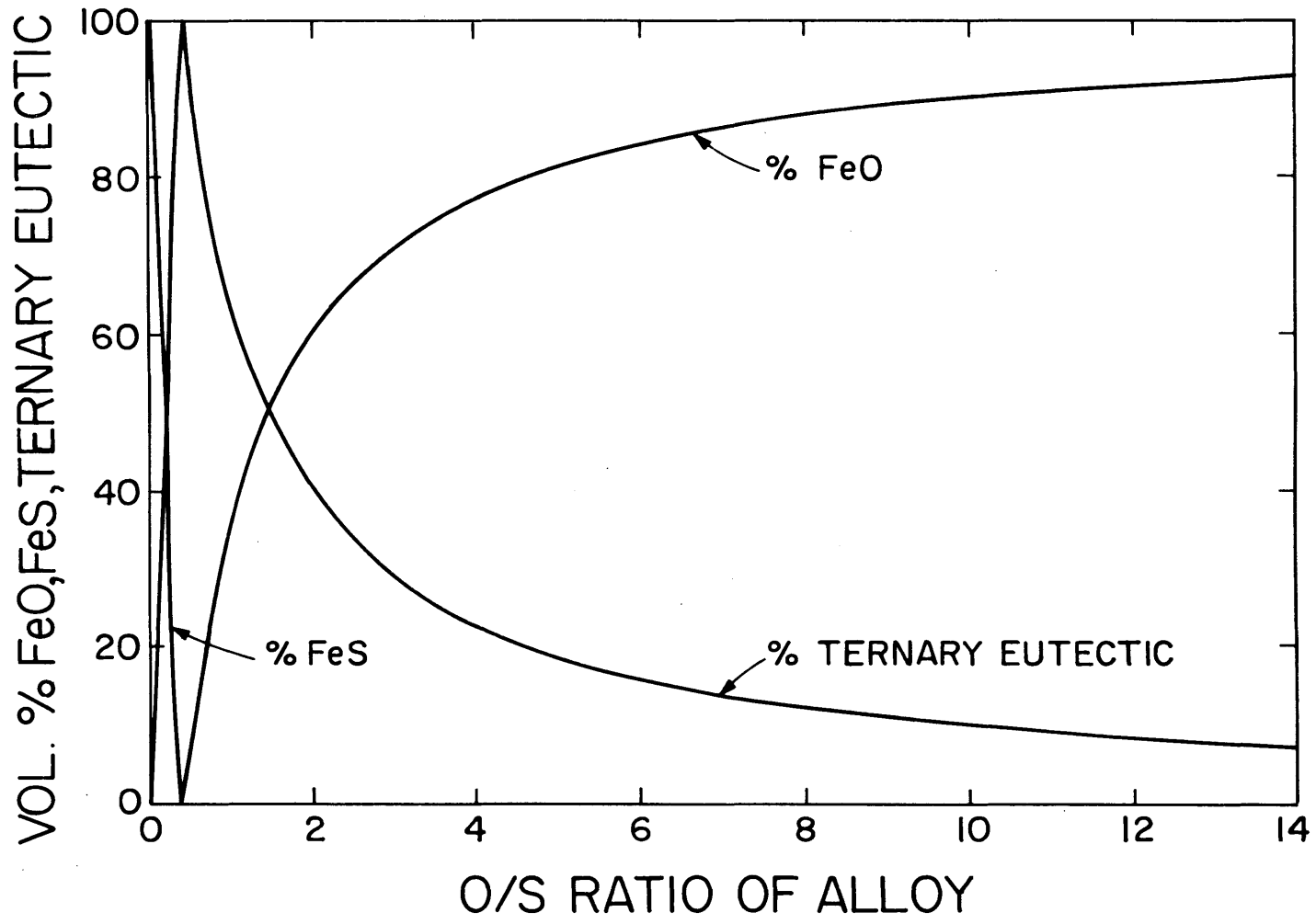


Figure 23. Inclusion composition versus O/S ratio of the melt for equilibrium solidification.

end of the reaction from the original O/S ratio of the melt. Thus, the composition and quantity of inclusions would be the same whether the miscibility gap existed or not. That is to say; the mere precipitation of pure iron from the original melt, in a simple two-phase reaction, would result in remaining liquid enriching in solute, while maintaining the original O/S ratio, and eventually reaching one of the pseudobinary eutectic lines at the same point and in the same quantities as  $L_2$ , produced by the more complex monotectic reaction. This is, of course, a direct result of the assumption of equilibrium conditions. For this reason melts of O/S ratio less than 0.09, which do not encounter the miscibility gap during solidification, resemble alloys of higher O/S ratio as far as location of the inclusions is concerned. Also the composition of these inclusions may be read off the graph in Figure 23 just as in the case of alloys of a higher O/S ratio.

#### Model 2: The "Isolation" Solidification Model

This model was derived by considering the solidification of a closed volume element of metal using the following assumptions:

1. There is no mass flow in or out of the volume element.
2. Negligible undercooling is required before nucleation, of both solid iron and the liquid slag,  $L_2$ , or is caused by kinetic or curvature effects.

3. Diffusion in the liquids is complete.

4. There is no solubility of oxygen or sulphur in solid iron.

5. Equilibrium is maintained at all interfaces but isolation of pools of  $L_2$  by the solidifying iron prevents the maintenance of equilibrium between  $L_1$  and  $L_2$ .

Assumptions (1), (2), (3) and (4) are the same assumptions as were made in the construction of the "equilibrium" solidification model. The new assumption (5) is the basis of the proposed model. In Model 1 it was assumed that  $L_1$  and  $L_2$  remain in contact throughout the monotectic reaction allowing maintenance of equilibrium. In the present model it is assumed that as  $L_2$  forms it is continually entrapped as small pools in the solidifying iron. Although equilibrium is maintained at all interfaces, the solid iron, separating  $L_1$  and the entrapped  $L_2$ , acts as barrier to mass transport and prevents the maintenance of equilibrium between the two liquids.

A possible mechanism by which the entrapment of  $L_2$  could take place is illustrated in Figure 24. The reaction under consideration is  $L_1 \rightarrow \alpha + L_2$ . As the solid iron ( $\alpha$ ) precipitates, the liquid  $L_1$  becomes enriched at the  $L_1/\alpha$  interface and consequently mass transport considerations make this interface the most favorable site for nucleation and growth of  $L_2$ . As no data on the interfacial energies involved are available the exact shape that  $L_2$  would assume is a matter for conjecture. Formation of a continuous film at this stage

would tend to prevent further growth of the iron dendrite and so a droplet form or "divorced" monotectic is a more likely configuration. Another conceivable morphology would be rods of  $L_2$  in the  $\alpha$  matrix. Figure 24 illustrates one step in the formation of a "divorced" monotectic structure, as a droplet of  $L_2$  is entrapped by the rapidly advancing  $\alpha/L_1$  interface. It should be born in mind that inspection of the computer results from Model 1 indicates that in the initial stages of solidification the growth rate, i.e., rate of change of weight fraction of the  $\alpha$  phase, is about three orders of magnitude greater than that of the  $L_2$  phase. In the drawing of Figure 24 it was tacitly assumed that:

$$\gamma_{\alpha L_1} + \gamma_{L_1 L_2} \leq \gamma_{\alpha L_2}$$

where  $\gamma_{ij}$  is the interfacial energy between phases  $i$  and  $j$ .

A mass balance, taking into account the compositions of the three phases as they change during solidification, may be written with the aid of Figure 25.

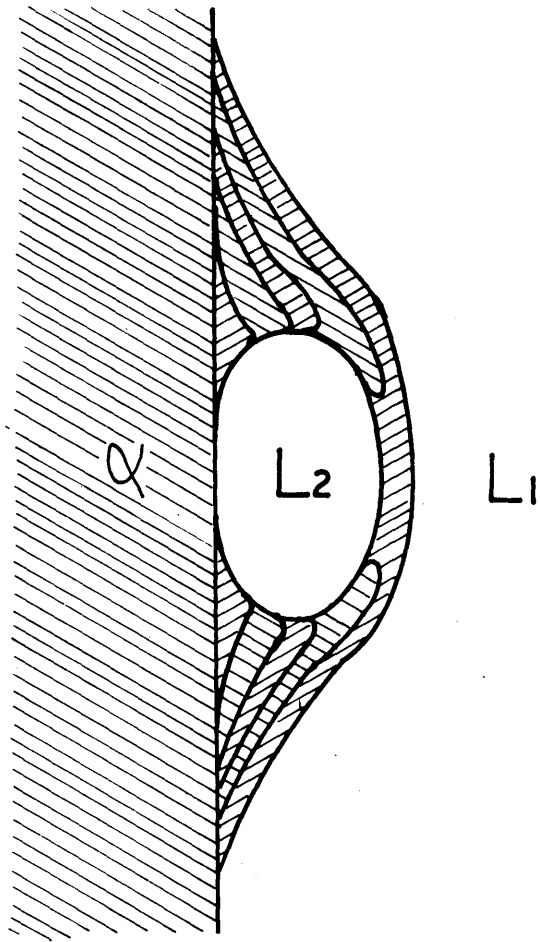


Figure 24. Schematic illustration of the entrapment of liquid slag  $L_2$  by the advancing  $\alpha$ - $L_1$  interface.



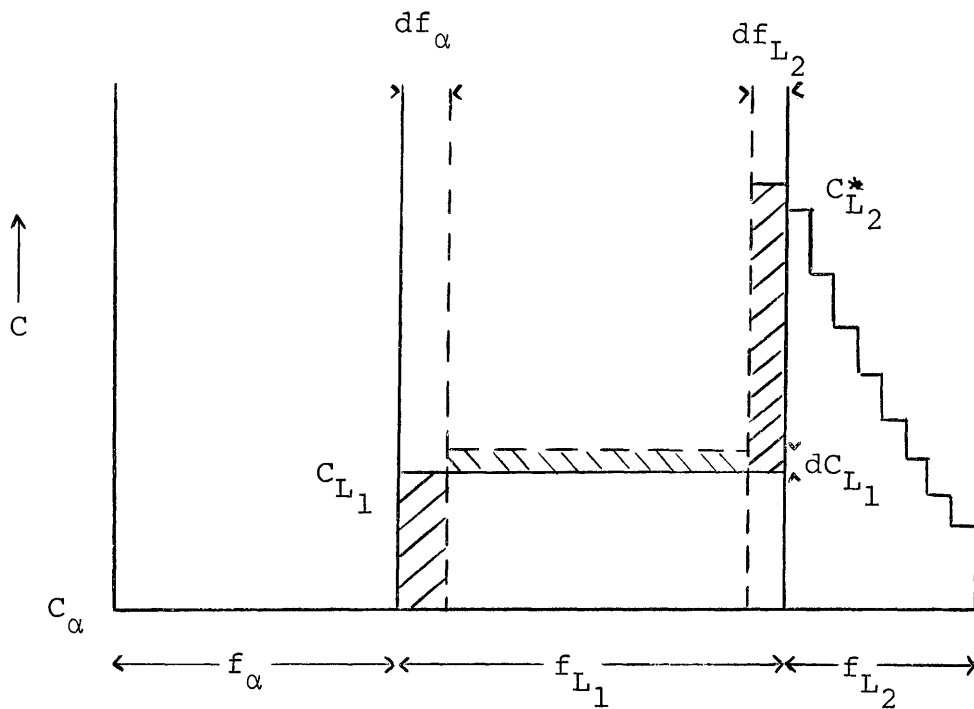


Figure 25. Compositions  $C_\alpha$ ,  $C_{L_1}$ , and  $C_{L_2}$  and fractions  $f_\alpha$ ,  $f_{L_1}$ , and  $f_{L_2}$  of the three phases  $\alpha$ ,  $L_1$  and  $L_2$  and their increments due to freezing of a differential quantity  $df_\alpha$  of  $L_1$ .

The various symbols used in this figure are listed in Table 6. As a small quantity  $df_\alpha$  of  $L_1$  freezes, the solute elements are redistributed between the remaining  $L_1$  and a quantity  $df_{L_2}$  of  $L_2$  whose composition  $C_{L_2}^*$ ,  $C_{L_2}'$  is given by the appropriate tie line at the temperature under consideration. Remembering that  $C_\alpha$  and  $C_\alpha'$  are both zero and neglecting terms involving products of two differential quantities, this redistribution can be written as follows:

For sulphur

$$C_{L_1} df_{\alpha} = (C_{L_2}^* - C_{L_1}) df_{L_2} + f_{L_1} dC_{L_1} \quad (70)$$

and for oxygen

$$C_{L_1}' df_{\alpha} = (C_{L_2}' - C_{L_1}') df_{L_2} + f_{L_1}' dC_{L_1}' \quad (71)$$

Also

$$f_{\alpha} + f_{L_1} + f_{L_2} = 1 \quad (72)$$

hence

$$df_{\alpha} = -(df_{L_1} + df_{L_2}) \quad (73)$$

Substituting (73) in (70) and rearranging:

$$-C_{L_1} (df_{L_1} + df_{L_2}) + (C_{L_1} - C_{L_2}^*) df_{L_2} = f_{L_1} dC_{L_1} \quad (74)$$

Eliminating terms and rearranging gives:

$$df_{L_2} = -(1/C_{L_2}^*) (f_{L_1} dC_{L_1} + C_{L_1} df_{L_1}) \quad (75)$$

Similarly

$$df_{L_2} = -(1/C_{L_2}') (f_{L_1}' dC_{L_1}' + C_{L_1}' df_{L_1}') \quad (76)$$

Equating (75) and (76) and rearranging:

$$df_{L_1} = -f_{L_1} \left[ \begin{array}{c} \frac{dC_{L_1}}{C_{L_2}^*} - \frac{dC'_{L_1}}{C_{L_2}^{*'}} \\ \frac{C_{L_1}}{C_{L_2}^*} - \frac{C'_{L_1}}{C_{L_2}^{*'}} \end{array} \right] \quad (77)$$

Solving for  $df_{L_1}$  in (75) and rearranging

$$df_{L_1} = -(1/C_{L_1}) (C_{L_2}^* df_{L_2} + f_{L_1} dC_{L_1}) \quad (78)$$

Similarly

$$df_{L_1} = -(1/C'_{L_1}) (C_{L_2}^{*' } df_{L_2} + f_{L_1} dC'_{L_1}) \quad (79)$$

Equation (78) and (79) and rearranging yields:

$$df_{L_2} = -f_{L_1} \left[ \begin{array}{c} \frac{dC_{L_1}}{C_{L_1}} - \frac{dC'_{L_1}}{C'_{L_1}} \\ \frac{C_{L_2}^*}{C_{L_1}} - \frac{C_{L_2}^{*' }}{C'_{L_1}} \end{array} \right] \quad (80)$$

A computer program was written to simulate the progress of the monotectic reaction in terms of  $df_{\alpha}$ ,  $df_{L_1}$ ,  $df_{L_2}$ ,  $f_{\alpha}$ ,  $f_{L_1}$ , and  $f_{L_2}$ . Equations (73), (77) and (80), the initial and final conditions, specified in equations (68) and (69) and interpolated tie lines relating  $C_{L_1}$ ,  $C'_{L_1}$ ,  $C_{L_2}^*$  and  $C_{L_2}^{*'}$  at small intervals  $dC_{L_1}$ ,  $dC'_{L_1}$  were used in the program. The method of forward differences was used and the actual program is given in Appendix I. The tie lines generated from the data of both

Hilty and Crafts<sup>12</sup> and Schurmann and von Hertwig<sup>46</sup> are given in Appendix F.

The solidification of five alloys with O/S ratios in the range 0.11 to 4, and having compositions on the line of intersection of the miscibility gap and iron liquidus surfaces, was considered by means of the computer programs. By comparing the output of this program with that obtained from the "equilibrium" program for the same alloys the two models may be contrasted. In Figure 26 the course of the three phase monotectic reaction, revealed by the computer output, is followed for the same alloy as that used to illustrate "equilibrium" solidification. In this case the liquid  $L_1$  is not consumed by the time  $L_2$  reaches the O/S ratio of the original melt but exists right down to the plait point at 1340°C where the composition of  $L_2$  becomes the same as that of  $L_1$ . This same general pattern of solidification is followed by all alloys under "isolation" conditions. Each succeeding generation of  $L_2$  formed has a composition given by the equilibrium tie line joining it to  $L_1$  from which it forms. However, the  $L_2$  does not remain in equilibrium with the enriched  $L_1$  but is trapped and removed from the equilibrium. This is true for each generation of  $L_2$  and consequently the fraction of  $L_2$ ,  $f_{L_2}$ , in Figure 26 refers to a cumulative total of all  $L_2$ , of decreasing O/S ratio, formed since the initiation of the three phase monotectic reaction.

The results of the computer program were used to build up a picture of "isolation" solidification. Figure 27 shows

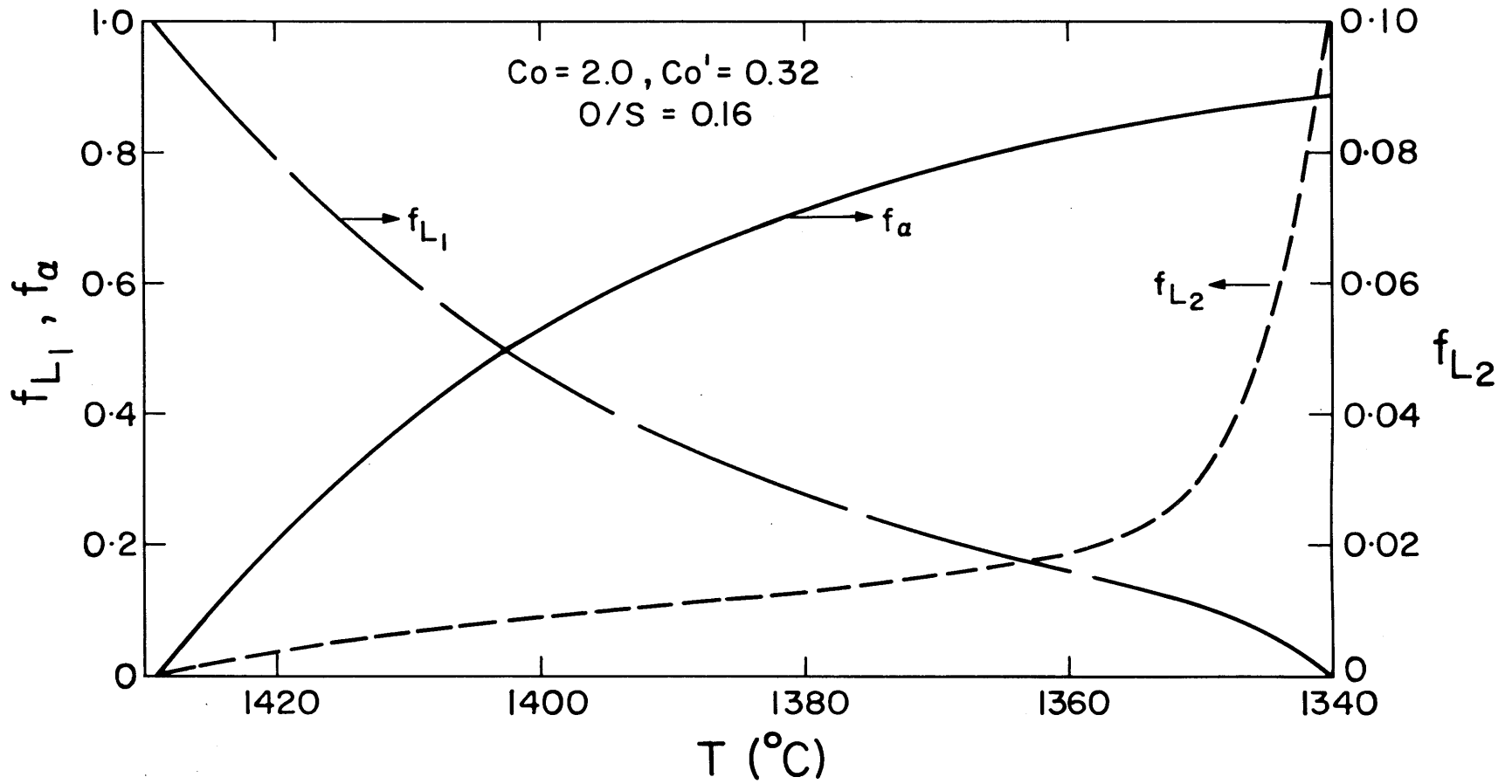


Figure 26. Fractions of iron ( $f_{\alpha}$ ),  $L_1$  ( $f_{L_1}$ ) and  $L_2$  ( $f_{L_2}$ ) as functions of temperature during the three-phase monotectic reaction according to the isolation solidification model.

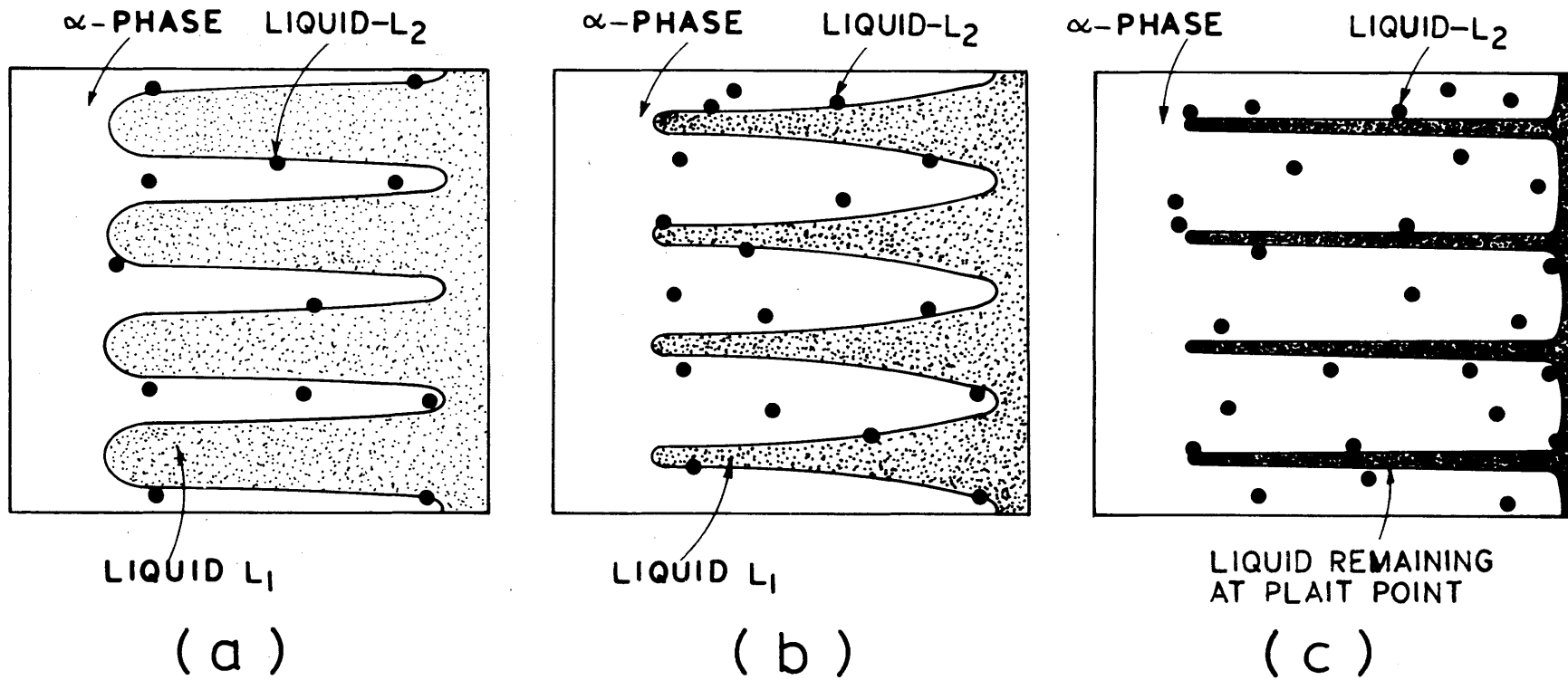


Figure 27. Schematic illustration of solidification in a small dendrite "volume element" of an Fe-FeO-FeS alloy according to the "isolation" model; (a) showing solid iron phase,  $\alpha$ , growing dendritically and the liquid slag phase, L<sub>2</sub>, becoming entrapped by the  $\alpha$ -phase, (b) continuation of this process as the liquid metal L<sub>1</sub> becomes enriched in oxygen and sulphur, (c) final stage of the three-phase monotectic reaction; the remaining interdendritic liquid having reached the plait point.

schematically how solidification of one dendrite "volume element" proceeds. As the dendrite grows, droplets of  $L_2$  form at its surface and are entrapped as its growth continues. The first  $L_2$  to form has the highest O/S ratio and each succeeding generation which is formed and trapped has a lower ratio than the preceding one. The three-phase reaction, and consequently the entrapment, ceases when the remaining liquid  $L_1$  reaches the lowest O/S ratio on the miscibility gap surface, at the plait point. In this process a whole series of pools of  $L_2$  of successively lower O/S ratios are left behind in an iron dendrite which is enveloped by a liquid of composition corresponding to that of the plait point.

The course of solidification may also be followed schematically on the phase diagram shown in Figure 28. This shows the compositions of the  $L_2$  pools formed from  $L_1$  as it moves toward the plait point P. As each pool is entrapped it starts to freeze as an independent system. Precipitation of iron in these pools causes the composition of the remaining liquid to move down the iron liquidus surface toward one of the pseudobinary eutectic lines. This is true of all the  $L_2$  formed up to and including the lowest O/S ratio liquid generated as the plait point is reached. The solidification of pools of  $L_2$  proceeds in exactly the same way as a pool of the same O/S ratio produced by "equilibrium" solidification. In this case, however, a whole spectrum of inclusion compositions based on the O/S ratios of the  $L_2$  pools is produced. The lower limit of the O/S ratio is clearly that

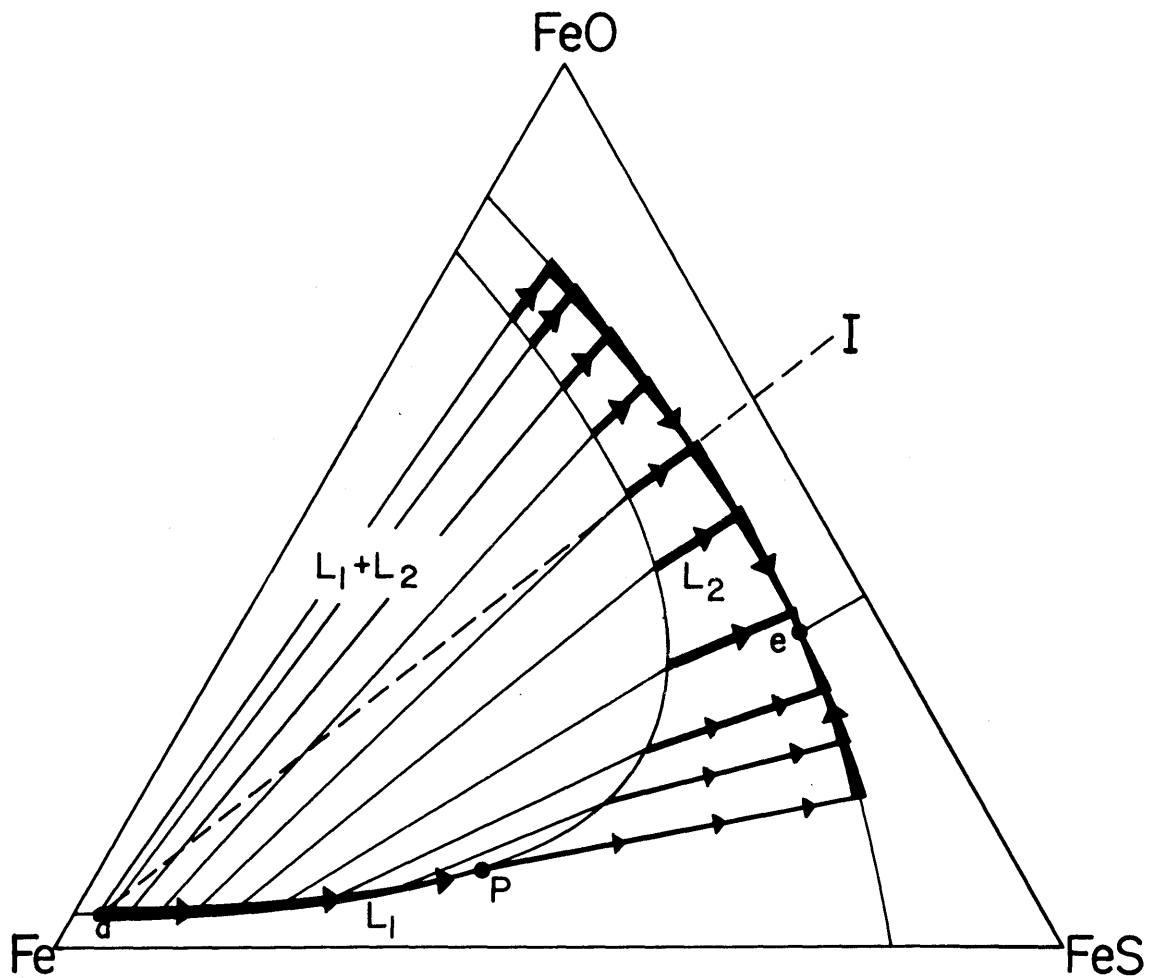


Figure 28. Schematic illustration of the course of solidification on the Fe-FeO-FeS phase diagram leading to inclusion formation according to the isolation solidification model.



of the plait point, i.e., 0.09. The upper limit is the O/S ratio of the  $L_2$  in equilibrium with the original melt composition, and the associated O/S ratio, at the iron liquidus surface. This number can simply be read off the graph in Figure 29. This is a plot of the O/S ratio in  $L_2$  versus the O/S ratio in  $L_1$  at the intersection of the miscibility gap and iron liquidus surfaces. For example the highest O/S ratio in  $L_2$  produced by a melt with an O/S ratio of 0.8 would be 8.5.

Figure 23 shows the final composition of the inclusions as a function of the O/S ratio of the  $L_2$  from which they formed and so the range of inclusion compositions given by "isolation" solidification of any alloy may be found. Taking an alloy with an O/S ratio of 0.8 as an example it can be seen that the inclusions would vary from oxide/ternary eutectic type inclusions, with a maximum of 89% FeO to sulphide/ternary eutectic type inclusions with a maximum of 67% FeS. A few inclusions of pure ternary eutectic would of course be included within the range.

Figure 30 shows the fraction of the total amount of  $L_2$  precipitated during the monotectic reaction, having an O/S ratio greater than that of the ternary eutectic point,  $F_{L_2}^{TE}$ , as a function of the O/S ratio of the original melt. This fraction constitutes the liquid which solidifies as inclusions of the oxide/ternary eutectic type. It can be seen that the higher the O/S ratio of the melt, the greater is the proportion of oxide/ternary eutectic type inclusions.

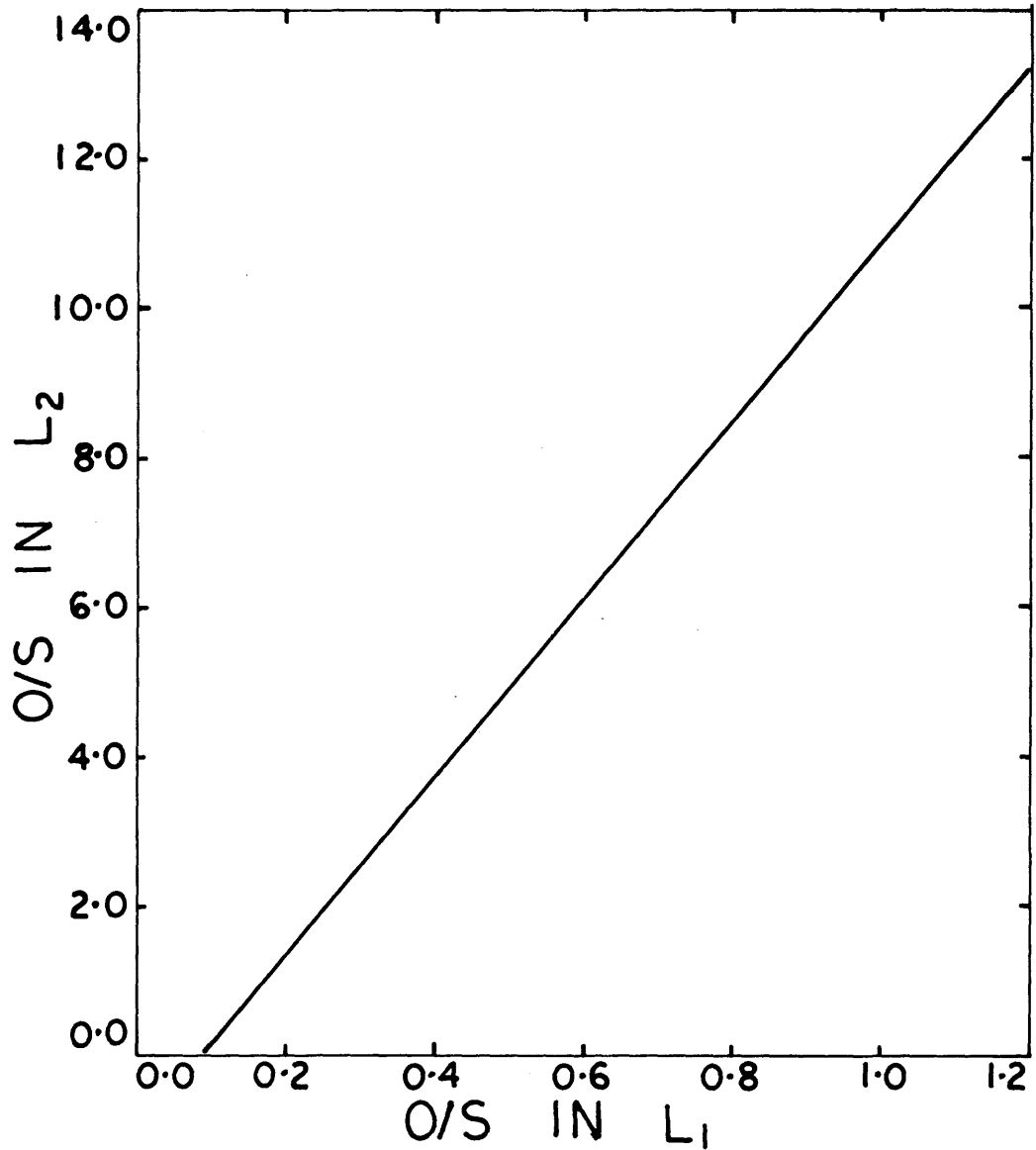


Figure 29. O/S ratio of the liquid slag  $L_2$  versus the O/S ratio of the liquid iron  $L_1$  at the intersection of the miscibility gap and iron liquidus surfaces (from the data of Hilty and Crafts<sup>12</sup>).

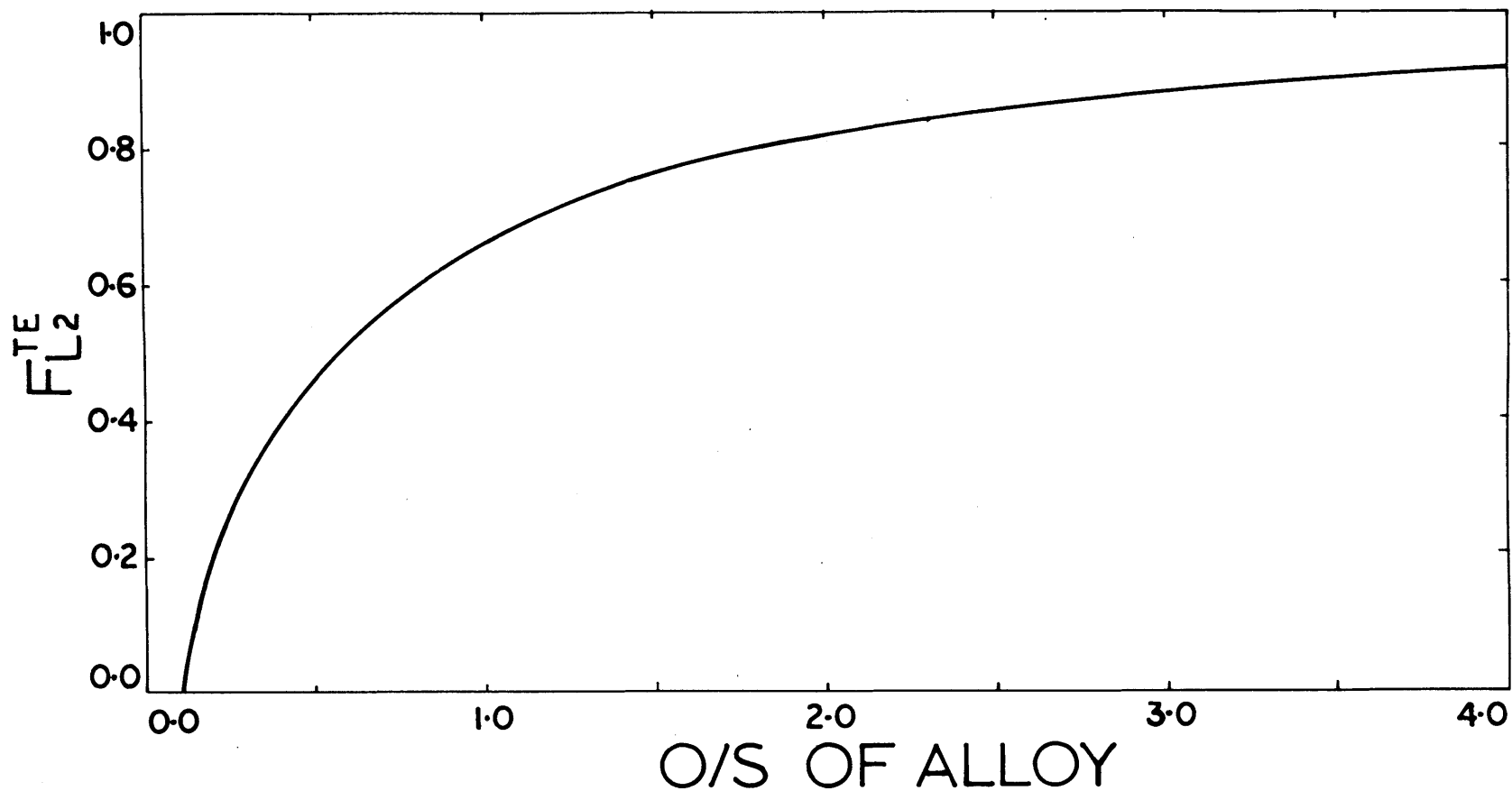


Figure 30. Fraction of the total amount of liquid slag ( $L_2$ ) precipitated during the monotectic reaction having an O/S greater than that of the ternary eutectic,  $F_{L_2}^{TE}$ , as a function of the O/S ratio of the melt.

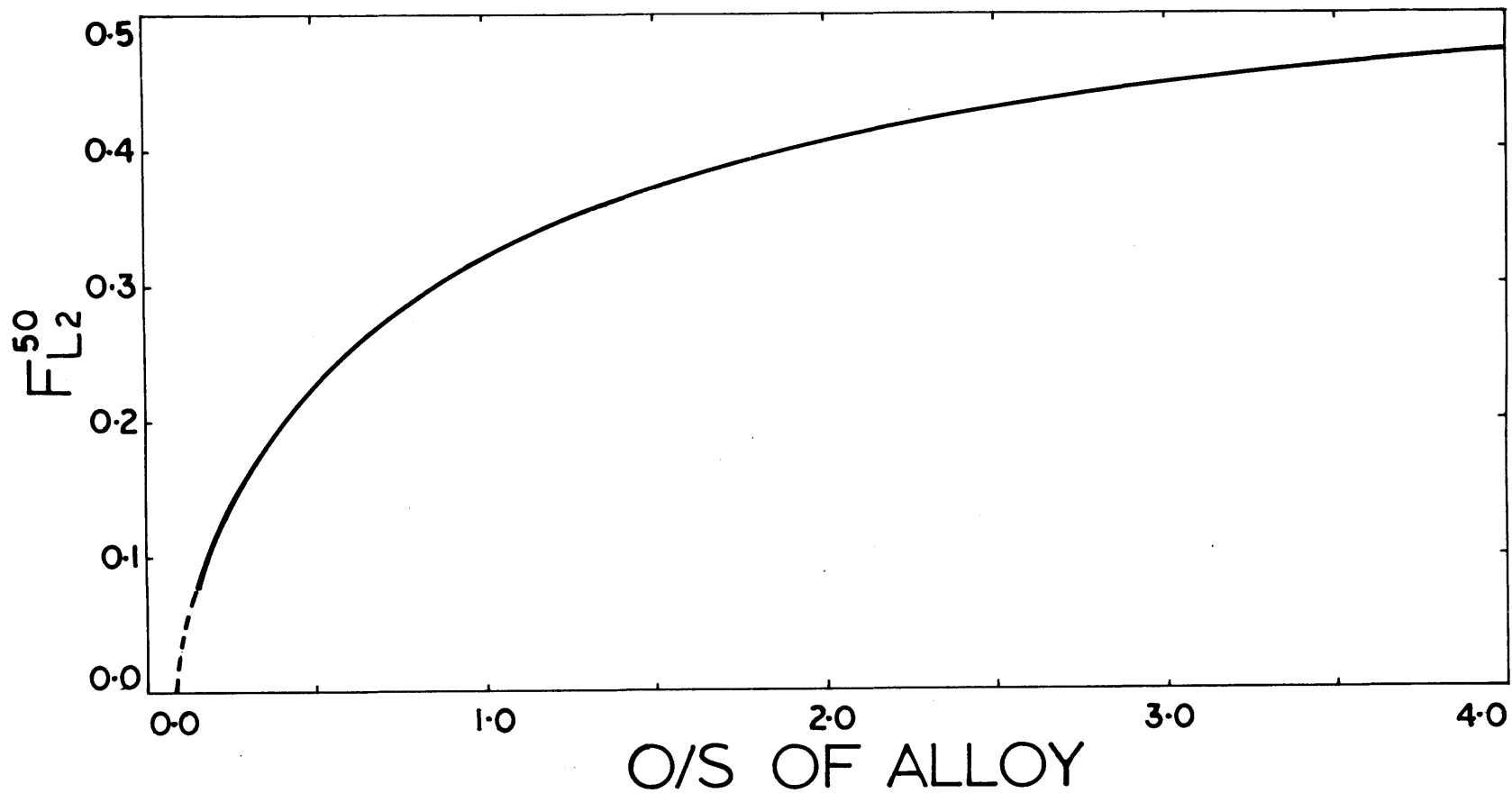


Figure 31. Fraction of the total amount of liquid slag ( $L_2$ ) precipitated during the monotectic reaction which is precipitated before the alloy is half solidified,  $F_{L_2}^{50}$ , versus the O/S ratio of the melt.

Figure 31 shows the fraction of the total amount of  $L_2$  precipitated during the monotectic reaction, which is precipitated before the alloy is half solidified, as a function of the O/S ratio of the melt. From this plot it is apparent that the higher the O/S ratio the greater the proportion of  $L_2$  entrapped in the early part of solidification. Thus in general, alloys of higher O/S ratio contain a greater proportion of oxide rich inclusions, which form from  $L_2$  isolated early in solidification, than do alloys of a lower O/S ratio.

The analysis, as it has been presented, strictly applies only to melts whose compositions lie exactly on the line of intersection of the miscibility gap and iron liquidus surfaces. For alloys poorer in oxygen than those on this line it can be shown that, as long as there is no solubility of sulphur or oxygen in solid iron, the same range of compositions of the inclusions will be produced as by an alloy of the same O/S ratio lying on the line. The reasoning behind this statement is the same as that given for the parallel case in "equilibrium" solidification.

In the case of an alloy richer in oxygen than the one of the same O/S ratio, the composition of which is on the line, the solution is not so simple. Until the iron liquidus surface is reached the two liquids formed when the miscibility gap was intersected remain in equilibrium and so Figure 22 may be used to illustrate the case. The first  $L_2$  to be entrapped during solidification of alloy "a" would have a composition  $y$

rather than b, which would be the case for an alloy of the same O/S ratio but whose composition lies on the line of intersection of the miscibility gap and iron liquidus surfaces. The pattern of solidification followed after this first entrapment would be exactly the same as was discussed above. Thus the range of composition of  $L_2$  entrapped to form the inclusions is restricted. The highest O/S ratio entrapped will correspond to compositions between b and d depending on the composition of the original melt between a and d, on line I. For compositions lying close to the line of intersection, however, the inclusion composition range would be the same, to a first approximation, as for melts on the line. In general, for alloys lying far out on the oxygen rich side of the line, either the oxygen, or sulphur content as well as the O/S ratio must be considered in order to specify the inclusion composition range exactly.

Alloys having O/S ratios of less than that of the plait point solidify in exactly the same way as was described by the "equilibrium" model because they do not encounter the miscibility gap during solidification.

### 3. Comparison of Models

Alloys solidifying according to the models described above would show two major differences in their microstructures. These differences would be seen in inclusion composition and morphology.

#### a. Inclusion Composition

If the "equilibrium" mode of solidification were followed, all inclusions would have the same composition at the end of solidification. This composition may be read off Figure 23; knowing the O/S ratio of the melt. The FeO or FeS content of the inclusions, as a function of the melt O/S ratio, is replotted in Figure 32. In this graph the phase diagram data of both Hilty and Crafts<sup>12</sup> and Schurmann and von Hertwig<sup>46</sup> are used to give two possible lines. The data of Schurmann and von Hertwig<sup>46</sup> were treated in exactly the same way as has been described for that of Hilty and Crafts to obtain the line shown and labeled S.

If the "isolation" mode of solidification were followed the inclusions would show a range of composition corresponding to a range of O/S ratios. The lower limit of the O/S ratio is given by the composition of the plait point in all cases and the inclusions formed from this liquid should contain about 67% FeS by volume, according to the phase diagram of Hilty and Crafts<sup>12</sup>. The composition of the inclusions of the highest O/S ratio is plotted in Figure 32 using the data of both Crafts and Hilty<sup>12</sup> and Schurmann and von Hertwig<sup>46</sup>. The composition is represented as a volume percent of FeO or FeS; the inclusions with the highest O/S ratio in a particular alloy containing the maximum volume percent FeO or minimum volume percent of FeS. For example; the inclusions in an alloy solidifying in this way from a melt of O/S ratio 0.2 would vary in composition from 52% FeO to 67% FeS or from 72% FeO to

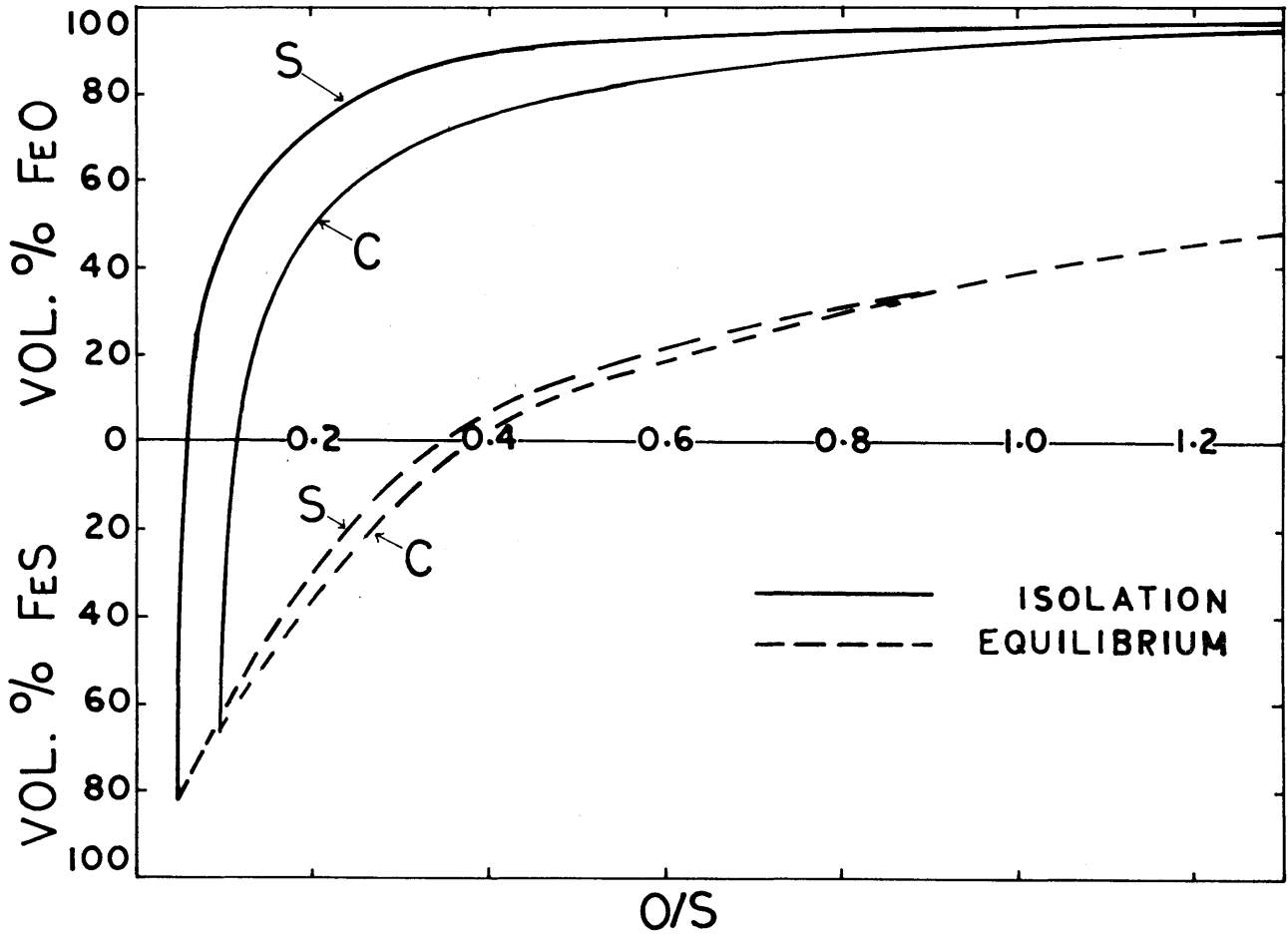


Figure 32. Maximum volume percent of FeO or minimum volume percent of FeS dendrites in the inclusions as a function of the O/S ratio of the melt predicted by the equilibrium and isolation solidification models, based on data of Hilty and Crafts<sup>12</sup> (C) and Schurmann and von Hertwig<sup>46</sup> (S).



82% FeS. The former figures originate from the curve based on the phase diagram of Hilty and Crafts<sup>12</sup> and the latter on the phase diagram of Schurmann and von Hertwig<sup>46</sup>. On the other hand if this alloy had solidified according to the "equilibrium" mode all inclusions would contain 36 to 30 volume percent FeS. It can be seen that while the use of the two sets of data; of Crafts and Schurmann, yield numerically slightly different results the qualitative results are exactly the same. A wide divergence exists between the predicted results of the two models; "equilibrium" and "isolation".

#### b. Morphology and Distribution of Inclusions

Equilibrium solidification would lead to all inclusions being positioned interdendritically. The most likely form for these inclusions to assume would be sheetlike envelopes around dendrite arms.

"Isolation" solidification, on the other hand, could produce globular inclusions within the dendrite arms as well as interdendritic sheets enveloping the arms. The interdendritic material would be high in sulphur and consist of inclusions of the FeS/ternary eutectic type. The globular inclusions inside the dendrite arms would be comparatively high in oxygen; typically of the FeO/ternary eutectic type. The inclusions with the highest O/S ratio; being entrapped first, should be deepest set into the dendrite arms. Alloys of relatively high O/S ratio solidify with a greater proportion of the included material in the form of high O/S ratio globular

inclusions than alloys of low O/S ratio. Conversely, alloys of relatively low O/S ratio solidify with a greater proportion of the included material in the form of low O/S ratio interdendritic inclusions than alloys of high O/S ratio.

It should be recognized that all melts having O/S ratios below that of the plait point give interdendritic inclusions of uniform composition during freezing. This is because the monotectic reaction does not occur during the solidification of these alloys.

## XII. EXPERIMENTAL TECHNIQUES

### A. Apparatus

Two accessories were added to the apparatus which otherwise was exactly the same as that described in Chapter IV of Part I. Firstly, small brass buckets were made and used in place of the copper molds in certain experiments. Secondly, a device for inducing nucleation of solid iron was introduced. It consisted of fine iron wires loosely held in a boron nitride mount which was designed to take the place of the charging cups on the turntable. The device could be manoeuvred in the same way as the charging cups.

### B. Materials

The materials used were exactly the same as those described in Chapter IV.

### C. Experimental Procedure

The object of the experiments was to determine the validity of either or both of the solidification models over a range of freezing rates. In order to do this, samples of various O/S ratios were solidified at different rates and examined metallographically to reveal the composition and morphology of the inclusions.

The samples were made up to the required oxygen and sulphur content ready for levitation in the same way as

described in Chapter V. Levitation melting and homogenization were also accomplished in the manner indicated in Chapter V. However, the cooling and casting procedures varied to some extent from those already described. Preliminary experiments, in which the samples were cast into copper chill molds from the homogenization temperature indicated that the high freezing rates obtained in this manner lead to inclusions so fine that composition determination of any sort was impossible. Accordingly two methods which gave lower cooling rates were used. The first method developed was solidification of the levitated specimen in situ by use of a high flow rate of coolant gas. Flow rates up to  $200 \text{ ft}^3/\text{hr}$  ( $1574 \text{ cm}^3/\text{sec}$ ) were used and cooling rates, as measured by the two-color pyrometer, of between  $1^\circ\text{C}/\text{sec}$  and  $20^\circ\text{C}/\text{sec}$  were achieved with relative ease. The cooling rate was kept constant as far as possible from the liquidus temperature to about  $1000^\circ\text{C}$  at which point the solid metal spheroid was dropped into a brass bucket. If nucleation of the solid iron presented a difficulty it was induced by prodding the slightly undercooled droplet with a fine iron wire. In order to achieve higher cooling rates a second method was used which involved cooling a sample down by gas flow, almost to the liquidus temperature, and then dropping it into a copper chill mold. The size of the inclusions formed indicated that the cooling rate was intermediate between the gas quench and the copper chill mold quench from the homogenization temperature. Unfortunately the cooling rate could not be measured but a rough estimate

could be made. In this way samples of various O/S ratios were solidified over a range of freezing rates. In order to avoid the possible complication of the precipitation of liquid  $L_2$  and its segregation to the surface, the composition of the samples were chosen to avoid saturation of the liquid metal  $L_1$  with slag  $L_2$  above the iron liquidus temperature.

#### D. Metallography

The procedure for sectioning and polishing the samples is discussed in Chapter V. Metallographic examination of the polished sections was used to reveal the morphology and composition of the inclusions.

The morphology of the inclusions could be studied with ease by examination under the microscope and inspection of photomicrographs of selected sections. The three dimensional aspect of the inclusions was revealed by carefully polishing down a section containing the inclusions and taking photographs of the section at intervals during the polishing. Micro-hardness indentations were used to locate the inclusion under consideration and the dimensions of the indentation before and after polishing were used in calculations of the depth of the material removed by the polishing. Inspection of consecutive photomicrographs allowed the change in shape of the inclusions with depth of penetration into the metal matrix to be followed. Consequently the three dimensional configuration of the inclusions could be revealed.

Three methods commonly used to identify the composition of inclusions are: (1) electron probe microanalysis, (2) electrolytic extraction followed by chemical analysis, and (3) optical metallography. The electron probe technique does not lend itself to the quantitative analysis of sulphur, and even the qualitative identification of oxygen is difficult, if not impossible, with equipment available today. Electrolytic extraction and chemical analysis of inclusions could reveal only an average inclusion composition, and hence composition variation cannot be studied by this means. Therefore, the only possibility remaining is optical microscopy which, for this particular system, is quite a viable technique. This is because only three phases are present in the solidified samples: iron, wustite and FeS and the microscopic appearance of these phases is very well known.<sup>33,55</sup> Also once the nature of the phase is established its composition can be characterized within close limits as solid solution between the phases is known to be quite limited.<sup>33</sup> The actual volume fractions of the phases in the inclusions were measured by a point counting method applied to photomicrographs of the inclusions. A fine grid was used because the structure of the inclusions was microscopically coarse and non-spherical. This point counting technique is discussed in Appendix J.

## XIII. RESULTS

The composition, morphology and spacial distribution of the inclusions were investigated by the methods of optical metallography described in Chapter XII. Both qualitative and quantitative data were used to describe the variation of these three aspects of the inclusions with the O/S ratio, the oxygen and sulphur levels, and the freezing rate of the melt.

A. Composition of the Inclusions

1. Qualitative Phase Identification

Examination of the microstructures of the alloys revealed two distinct types of inclusions from the point of view of composition. The difference between them is illustrated in Figure 33. Photomicrograph a shows an inclusion containing dark gray material in a two phase medium gray matrix. Photomicrograph b shows inclusions containing light gray dendritic material in a two phase matrix of the same color as that in photomicrograph a. The bulk phase containing the inclusions is iron which appears very light gray or white in the unetched microstructures, depending on the lighting conditions. Black areas are either dust, microporosity or holes opened up by fragmentation of a brittle phase during polishing.

Inspection of the Fe-FeS-FeO phase diagram shows that only three phases can result from solidification of iron rich alloys containing sulphur and oxygen. These are iron, wustite and iron sulphide. Also solid solution between all three

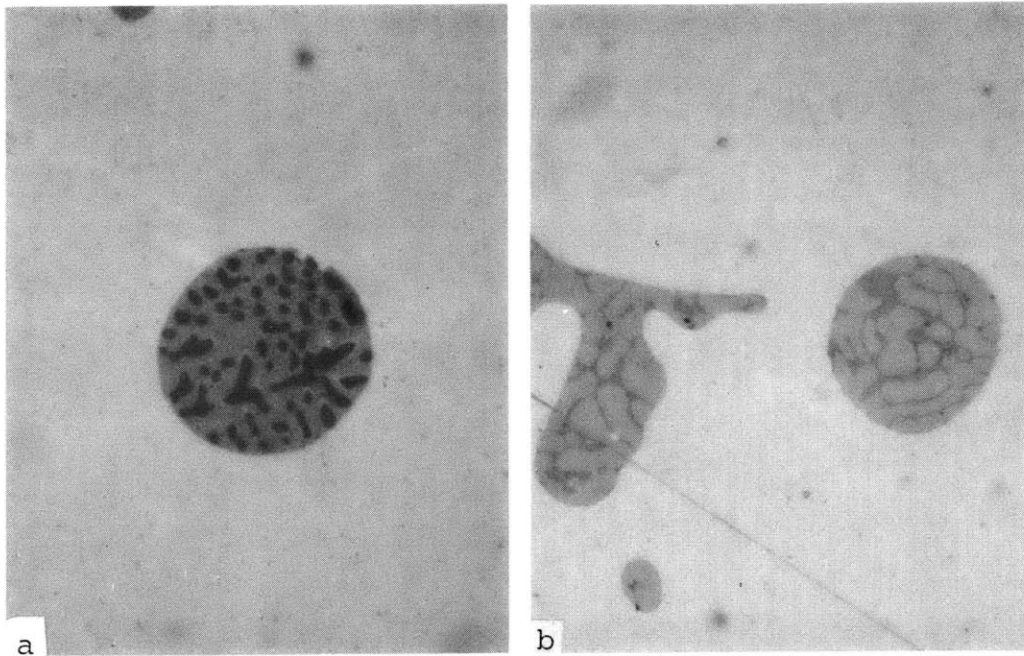


Figure 33: Photomicrographs of Fe-S-O alloys showing typical inclusions, unetched, 1000X.

- (a) Inclusion contains wustite dendrites in an iron sulphide-wustite eutectic matrix.
- (b) Inclusions contain iron sulphide dendrites in an iron sulphide-wustite eutectic matrix.



phases is quite limited<sup>33</sup>. The appearance of the phases is well documented<sup>33,55</sup> and consequently the various field in the photomicrographs of Figure 33 may be identified.

The dark gray dendritic material was identified as wustite; the light gray dendritic material as iron sulphide and the matrix containing them as a eutectic of wustite and iron sulphide. Sometimes minute quantities of iron appear in the inclusions and in fact close inspection of the irregularly shaped inclusion in Figure 33b reveals two small white spots of iron.

## 2. The Range of Inclusion Composition

Having established the identity of the various phases in the inclusions, and knowing the compositions of these phases, the composition of the inclusions can be estimated visually or determined quantitatively by a point counting technique.

### a. Qualitative Observations of Inclusion Composition.

In general for alloys of O/S ratio greater than 0.05 a range of inclusion compositions was observed in all samples no matter what cooling rate was chosen. Figure 34 illustrates the range of inclusion compositions found in an alloy of O/S ratio equal to 1.25 solidified in the levitation coil at a rate of about 1°C/sec. The various phases in these inclusions are easily recognizable with the magnification of 1000X used here. The large inclusions in photomicrographs a, b, c, d, e, f, and g of Figure 34 contain wustite, in progressively

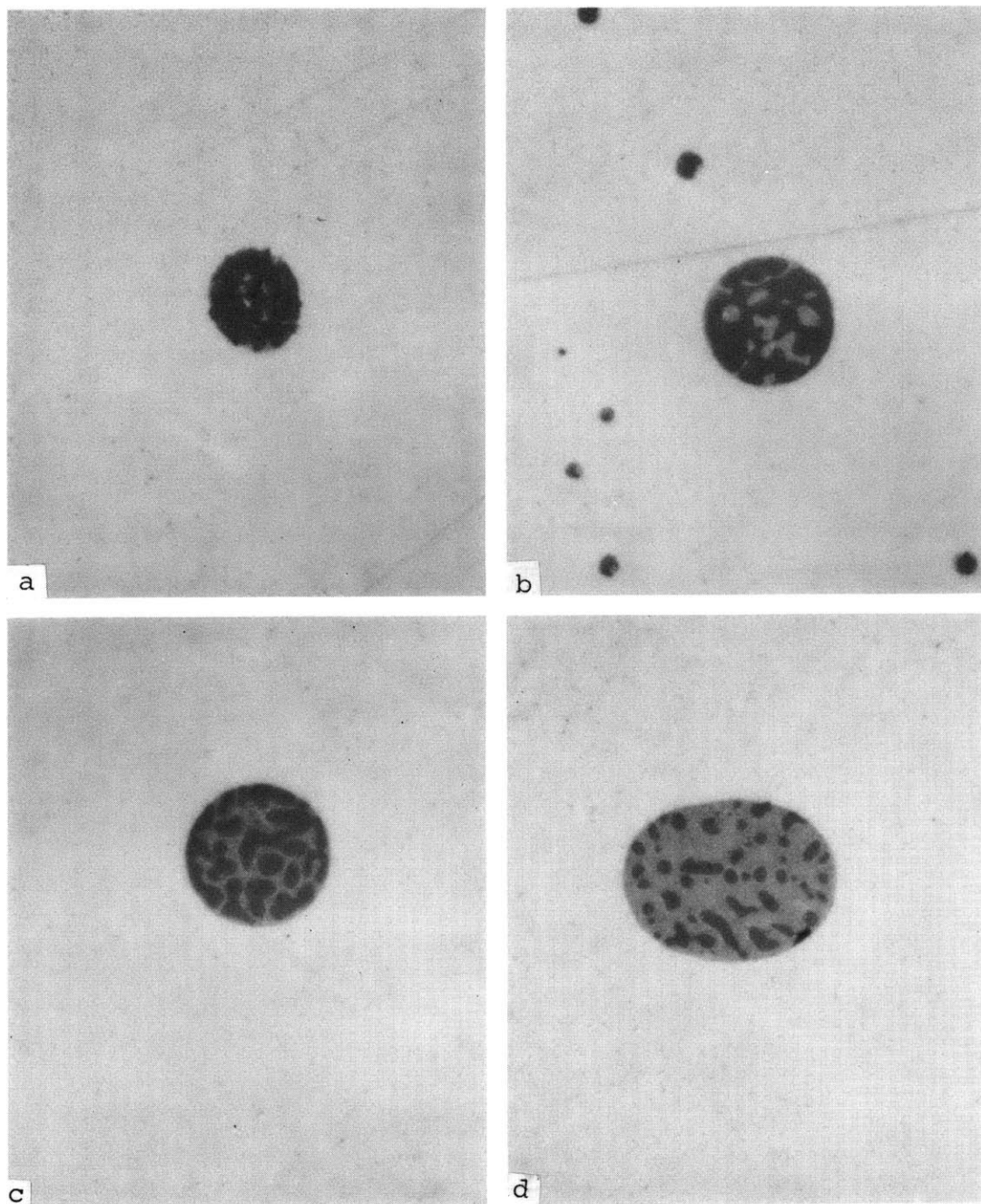


Figure 34: Photomicrographs of an Fe-0.14% S-0.175% O alloy ( $O/S = 1.25$ ) solidified at  $1^{\circ}\text{C}/\text{sec}$ , unetched, 1000X. Shows inclusions of progressively decreasing O/S ratio.

- (a)-(g) Contain decreasing fractions of wustite dendrites in an iron sulphide-wustite eutectic matrix.
- (h) Contains iron sulphide-wustite eutectic only.
- (i)-(l) Contain increasing fractions of iron sulphide dendrites in an iron sulphide-wustite eutectic matrix.

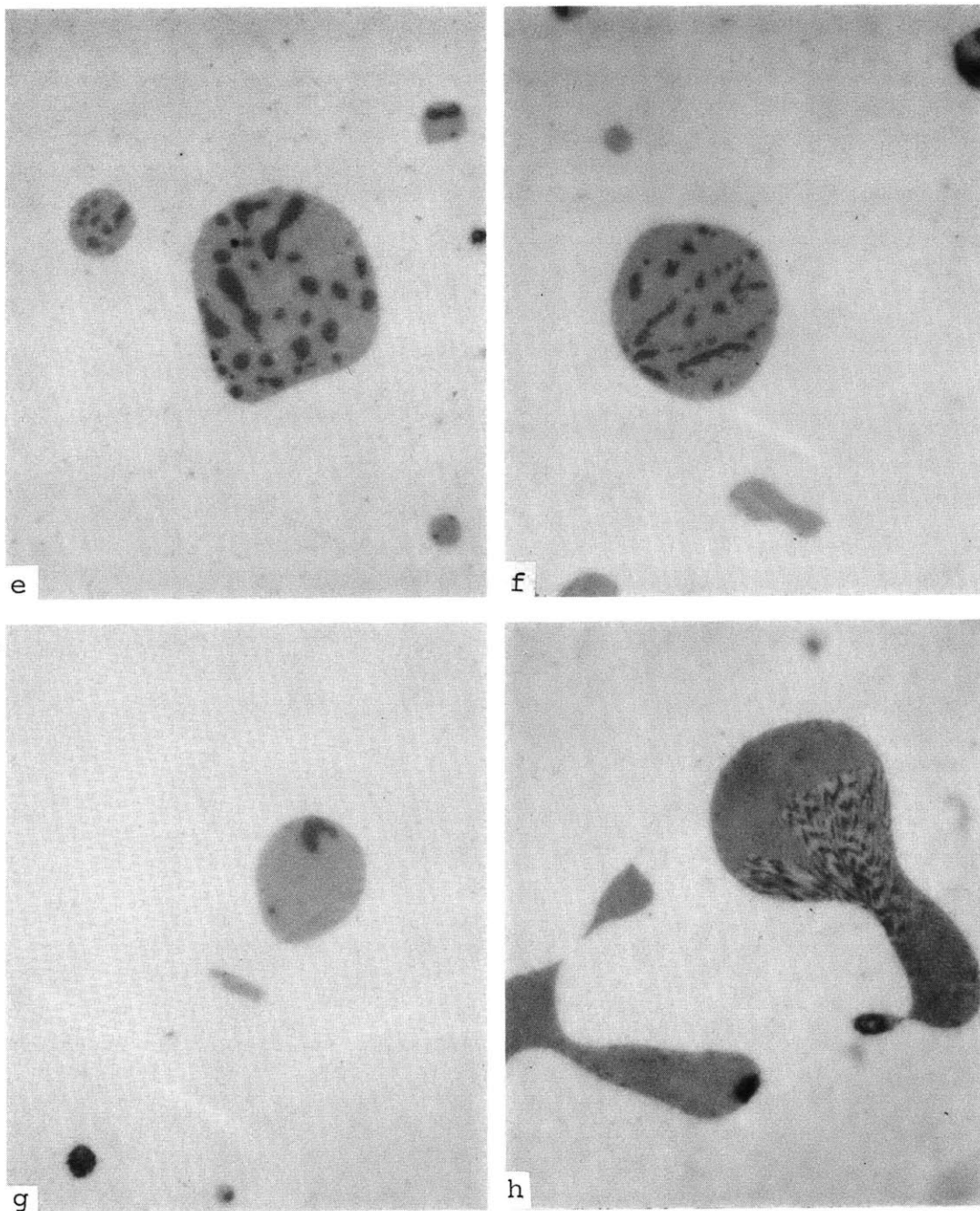


Figure 34 (cont'd)

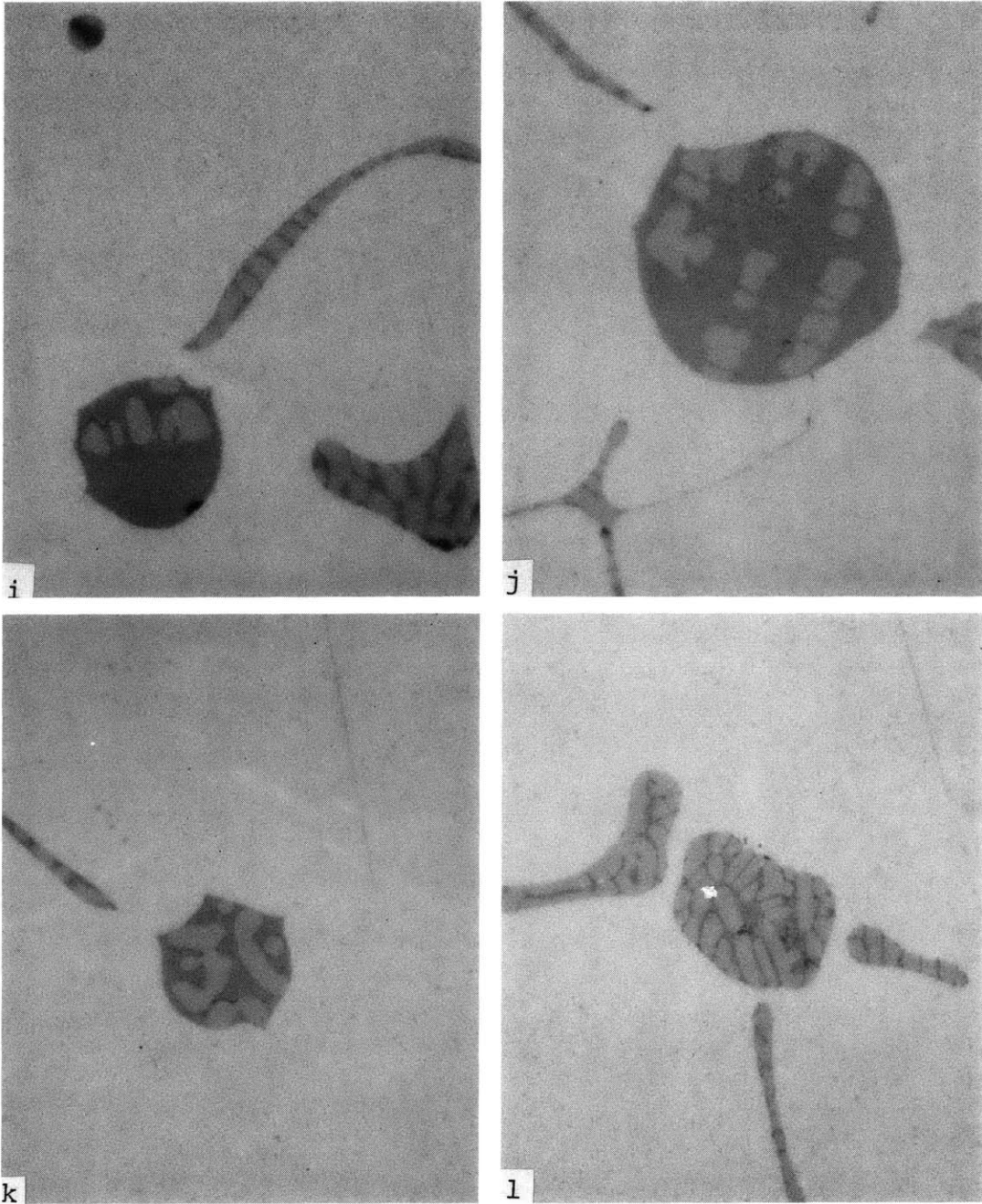


Figure 34 (cont'd)

smaller fractions, in a matrix of wustite-iron sulphide eutectic. Photomicrograph h of Figure 34 shows an inclusion made up entirely of the wustite-iron sulphide eutectic. The large inclusions in photomicrographs i, j, k, and l of Figure 34 contain iron sulphide in progressively larger fractions in a wustite-iron sulphide eutectic matrix. All samples contain iron sulphide rich inclusions, similar to those shown in Figure 34(l), no matter what the overall O/S ratio of the alloys is. However, only samples with an O/S ratio greater than about 0.1 contain inclusions rich in wustite like that shown in Figure 33a. No variation of inclusion composition was observed in samples having an O/S ratio of less than 0.05. Also samples having the same O/S ratio but different oxygen and sulphur contents appeared to possess the same range of inclusion compositions.

b. Quantitative Observations of Inclusion Composition

The range of composition of the inclusions was determined as a function of O/S ratio of the alloy at a constant cooling rate. Also the composition of the inclusions richest in oxygen was measured for alloys of many different O/S ratios again at constant cooling rate. Included in these measurements were some for alloys of the same O/S ratios but different oxygen and sulphur levels. Finally the range of inclusion compositions of alloys of identical O/S ratios but which were solidified at different rates, was determined. The point counting technique used to determine composition is described and its reproducibility is discussed in Appendix J.

(i) Composition Range at Constant Cooling Rate.

The volume percentages of wustite and iron sulphide were measured for inclusions in samples of three different O/S ratios, solidified in the coil at a rate of approximately  $1^{\circ}\text{C}/\text{sec}$ . The results of these experiments together with the compositions and O/S ratios of the three alloys are given in Table 7. The extremes of the composition ranges are given by the highest wustite and iron sulphide contents of the inclusions. Sample 102-1 with an O/S ratio of 0.15, contains inclusions ranging in composition from 50 percent wustite to 80 percent iron sulphide. Sample 93-4; with an O/S ratio of 0.5, contains inclusions in the range of 85 percent wustite to 79 percent iron sulphide and sample 100-2, O/S ratio 1.25, shows a range of 95 percent wustite to 75 percent iron sulphide.

Within the limits of the accuracy of the measurements, the maximum concentration of iron sulphide observed in the inclusions of all three samples is the same, namely about 75 percent. However, the maximum wustite content increases with increasing O/S ratio from 50 percent at a ratio of 0.15 to 95 percent at a ratio of 1.25.

(ii) Maximum Wustite Content of the Inclusions.

Quantitative measurements of the wustite content of inclusions appearing to contain the maximum fraction of wustite, were made on a series of alloys of different O/S ratios, in order to show the increase of maximum wustite content with increasing O/S ratio. Also, similar measurements

Table

## Range of Inclusion Composition

sample number	102-1	93-4	100-2	100-2 (cont'd)
oxygen/sulphur ratio	0.15	0.50	1.25	
melt composition	0.40%S 0.06%O	0.30%S 0.15%O	0.14%S 0.175%O	
	inclusion composition vol. pct.	inclusion composition vol. pct.	inclusion composition vol. pct.	inclusion composition vol. pct.
	FeO or FeS	FeO or FeS	FeO or FeS	FeO or FeS
	50 FeO	85 FeO	95 FeO	17 FeO
	34 FeO	75 FeO	89 FeO	15 FeO
	20 FeO	54 FeO	82 FeO	9 FeO
	10 FeO	49 FeO	79 FeO	6 FeO
	6 FeO	42 FeO	76 FeO	
		26 FeO	68 FeO	{0 FeO
	{0 FeO	10 FeO	61 FeO	{0 FeS
	{0 FeS		50 FeO	
		{0 FeO	40 FeO	21 FeS
	20 FeS	{0 FeS	36 FeO	25 FeS
	51 FeS		26 FeO	30 FeS
	60 FeS	15 FeS	23 FeO	45 FeS
	75 FeS	40 FeS	20 FeO	49 FeS
	80 FeS	79 FeS		60 FeS
				75 FeS

were made on alloys of the same O/S ratio but which contained different total amounts of the alloying elements. This test would be expected to highlight any effect of the actual oxygen and sulphur contents as opposed to their ratio. The results of these measurements together with the O/S ratios and the melt compositions are presented in Table 8. One alloy, 98-1, showed a range of inclusion compositions but no inclusions containing wustite, apart from that in the eutectic matrix. In this case the inclusion containing the minimum fraction of iron sulphide is the richest in oxygen and so this minimum percent is recorded in Table 8. All alloys reported in this table were solidified at a rate of  $1^{\circ}\text{C}/\text{sec}$ .

Examination of the data in Table 8 shows that alloys of increasing O/S ratio contain inclusions increasingly rich in wustite. This result is therefore in agreement with the indications of the data given in Table 7. Also, the maximum wustite content, of inclusions in alloys of the same O/S ratio but different total oxygen and sulphur additions, are equal within the limits of the experimental uncertainty. Thus the important parameter to be considered is the O/S ratio rather than the actual level of oxygen or sulphur. This result also serves to illustrate the reproducibility of the composition measurements when applied to alloys of equal O/S ratio.

(iii) Effect of Cooling Rate.

In order to establish the effect of cooling rate on the range of composition of inclusions, melts of the same O/S ratio



Table 8

## Maximum Wustite Content of Inclusions

sample number	oxygen/sulphur content	melt composition		min. [FeS] or max. FeO (vol. pct.)
		%S	%O	
98-1	0.050	0.40	0.020	[15]
98-2	0.075	0.40	0.030	16
101-1	0.100	0.40	0.040	0
101-2	0.150	0.40	0.060	40
102-1	0.150	0.20	0.030	48
101-3	0.200	0.40	0.080	55
94-1	0.250	0.20	0.050	50
96-1	0.250	0.40	0.100	60
73-2	0.300	0.50	0.150	77
93-2	0.400	0.40	0.160	80
104-2	0.500	0.34	0.170	82
93-4	0.500	0.30	0.150	84
94-2	0.500	0.20	0.100	86
99-4	0.625	0.20	0.125	86
99-1	0.750	0.20	0.150	90
100-1	1.000	0.16	0.160	86
99-2	1.000	0.20	0.200	92
100-2	1.250	0.14	0.175	93
99-3	1.250	0.20	0.250	96

Table 9

## Effect of Cooling Rate of Inclusion Composition Range

sample number	93-4	94-5	75-3
oxygen/sulphur ratio	0.5	0.5	0.5
melt composition	0.30%S 0.15%O	0.20%S 0.10%O	0.30%S 0.15%O
cooling rate	$\sim 1^{\circ}\text{C}/\text{sec}$	$\sim 10^{\circ}\text{C}/\text{sec}$	between $20^{\circ}\text{C}/\text{sec}$ and $100^{\circ}\text{C}/\text{sec}$
	inclusion composition vol. pct.	inclusion composition vol. pct.	inclusion composition vol. pct.
	85 FeO 75 FeO 54 FeO 49 FeO 42 FeO 26 FeO 10 FeO { 0 FeO 0 FeS	83 FeO 65 FeO 60 FeO 57 FeO 47 FeO 35 FeO 32 FeO 25 FeO 12 FeO 6 FeO	86 FeO 80 FeO 56 FeO 47 FeO 31 FeO 10 FeO { 0 FeO 0 FeS 30 FeS 42 FeS 79 FeS
	15 FeS 40 FeS 79 FeS	{ 0 FeO 0 FeS 16 FeS 49 FeS 75 FeS	

Table 10

## Effect of Cooling Rate on Inclusion Composition Range

sample number	100-2	100-2 (cont'd)	100-3
oxygen/sulphur ratio	1.25	1.25	1.25
melt composition	0.14%S 0.175%O		0.14%S 0.175%O
cooling rate	~1°C/sec		between 20°C/sec and 100°C/sec
	inclusion composition vol. pct.	inclusion composition vol. pct.	inclusion composition vol. pct.
	95 FeO 89 FeO 82 FeO 79 FeO 76 FeO 68 FeO 61 FeO 50 FeO 40 FeO 36 FeO 26 FeO 23 FeO 20 FeO	17 FeO 15 FeO 9 FeO 6 FeO { 0 FeO 0 FeS 21 FeS 25 FeS 30 FeS 45 FeS 49 FeS 60 FeS 75 FeS	94 FeO 85 FeO 70 FeO 61 FeO 49 FeO 30 FeO 16 FeO 21 FeS 40 FeS 69 FeS

were solidified at different rates and the compositions of the inclusions determined by point counting. Alloys of two O/S ratios; 0.5 and 1.25, were used. The former alloys were solidified at three different rates; described here as slow, medium and fast, and the latter at two rates; slow and fast. The slow and medium rates were achieved by helium flow regulation and were measured with the two-color pyrometer. The fast cooling rate, achieved by dropping the melt, from a temperature close to the liquidus, into a copper mold, could not be measured but the smaller inclusion size produced indicated that it was very much faster than the slow or medium cooling rates. Suffice it to say that it was within a range of one to two orders of magnitude greater than the slow cooling rate.

The results of these experiments are produced in Tables 9 and 10 and from them it can be seen that the variation of freezing rate, within the specified limits, has no effect on the range of inclusion composition.

### 3. Summary of the Results on Inclusion Composition

Two distinct types of inclusions exist; those which contain wustite in a wustite-iron sulphide eutectic matrix and others which contain iron sulphide in the same matrix. Also, a few inclusions exist that are made up entirely of eutectic.

Inclusions in alloys of O/S ratios in excess of 0.05 always display a range of compositions between those rich in sulphur and other comparatively rich in oxygen. The

inclusions richest in sulphur have the same composition in all samples no matter what the O/S ratio, provided of course that it is above 0.05. This composition is about 75 percent iron sulphide by volume. On the other hand the inclusions richest in oxygen vary in composition with the O/S ratio. The maximum free wustite content of the inclusions increases from zero at an O/S ratio of about 0.08 to 95 percent at an O/S ratio of 1.25. For O/S ratios between 0.05 and 0.08 the inclusions richest in oxygen contain no wustite apart from that in the eutectic matrix but rather the minimum fraction of iron sulphide. Alloys with an O/S ratio of less than 0.05 have inclusions containing in excess of 75 percent iron sulphide but show no variation in composition.

The inclusion composition range was not affected by the level of oxygen or sulphur in themselves but only by the ratio of the two. Also variation of the freezing rate over two orders of magnitude had no effect on the composition range of the inclusions.

#### B. Inclusion Morphology and Distribution

The morphology and distribution of the two types of inclusions, wustite rich and iron-sulphide rich, were investigated by optical metallographic techniques outlined in Chapter XII. Also the effects of variation in O/S ratio and solidification rates of the alloys on these aspects were explored.

1. Morphology and Distribution of Wustite Rich and Iron Sulphide Rich Inclusions

Inclusions rich in wustite tend towards a spherical shape, in fact the higher the fraction of wustite the more nearly spherical they become. This tendency is illustrated in Figure 34 and the observation was confirmed by polishing through a wustite rich inclusion in steps of a few microns, taking pictures of the inclusion at each stage. Four cross sections of such an inclusion are shown in Figure 35. Photomicrographs a, b, c and d represent successive stages in the process and from them it can be seen that the cross section remained circular at all times. This fact together with the knowledge of the depth of the material removed during each step, which is shown in Figure 35, led to the conclusion that the inclusion was nearly spherical.

The situation regarding iron sulphide rich inclusions is not nearly so clear cut as can be seen from photomicrographs i, j, k and l of Figure 34 where sulphide rich inclusions in a variety of shapes are illustrated. Polishing down through inclusions of this type revealed that the majority of those appearing circular in cross section were more nearly ovoid or rod-like in three dimensions rather than spherical. The inclusions approaching the maximum sulphide content always appeared as stringers or sheets in two dimensions and polishing down through them revealed that nearly all of them were in fact sheets or envelopes. Such inclusions can be seen in photomicrographs i, j, k and l of Figure 34.

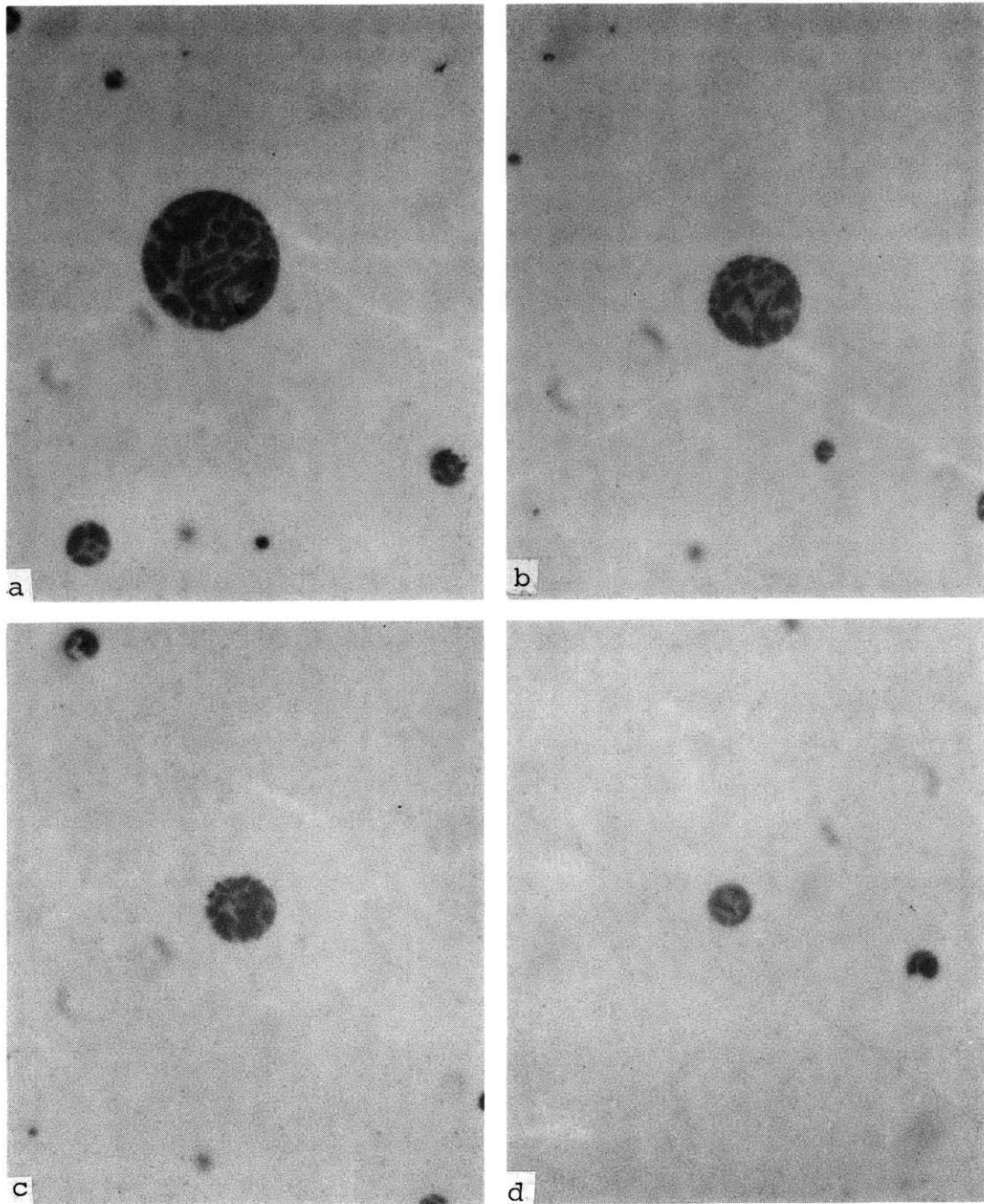


Figure 35: Photomicrographs of an Fe-0.14% S-0.175% O alloy ( $O/S = 1.25$ ) solidified at  $1^{\circ}\text{C}/\text{sec}$ , unetched, 1000X. Show successive sections through the same inclusions. Spacing between the sections is as follows:  
 $a \rightarrow b \sim 5$  microns,  $b \rightarrow c \sim 2$  microns,  $c \rightarrow d \sim 2$  microns.

The appearances of the two inclusion types are contrasted in Figure 36 a and b, which show both the near spherical wustite rich and the sheet and stringer type iron sulphide rich inclusions. The relative positions of the two types of inclusions are well illustrated by these photomicrographs. The sulphide rich material is concentrated in the interdendritic spaces and hence it almost envelopes the dendrite arms. On the other hand the spherical wustite rich inclusions are located inside the dendrite arms and are consequently surrounded by the sulphide rich inclusions.

Figures 36 c and d also show stringer-like sulphide rich inclusions, but in these photomicrographs the wustite rich inclusions are not so nearly spherical and they contain only a small fraction of wustite. The figure also illustrates the closeness of approach between the wustite rich and iron sulphide rich inclusions. Careful polishing down through the sections such as these revealed that the two inclusion types never in fact joined. However, sulphide rich inclusions like the oval shaped one in Figure 36c were found to be connected to the adjacent sulphide rich inclusions in nearly all instances. The wustite rich inclusions were found to be isolated by the iron matrix from all other inclusions including nearby inclusions of the same composition.

## 2. Effect of O/S Ratio

The above observations were made on alloys of high O/S ratio from 0.5 to 1.25. In order to determine the possible effects of O/S ratio on the morphology and distribution of the



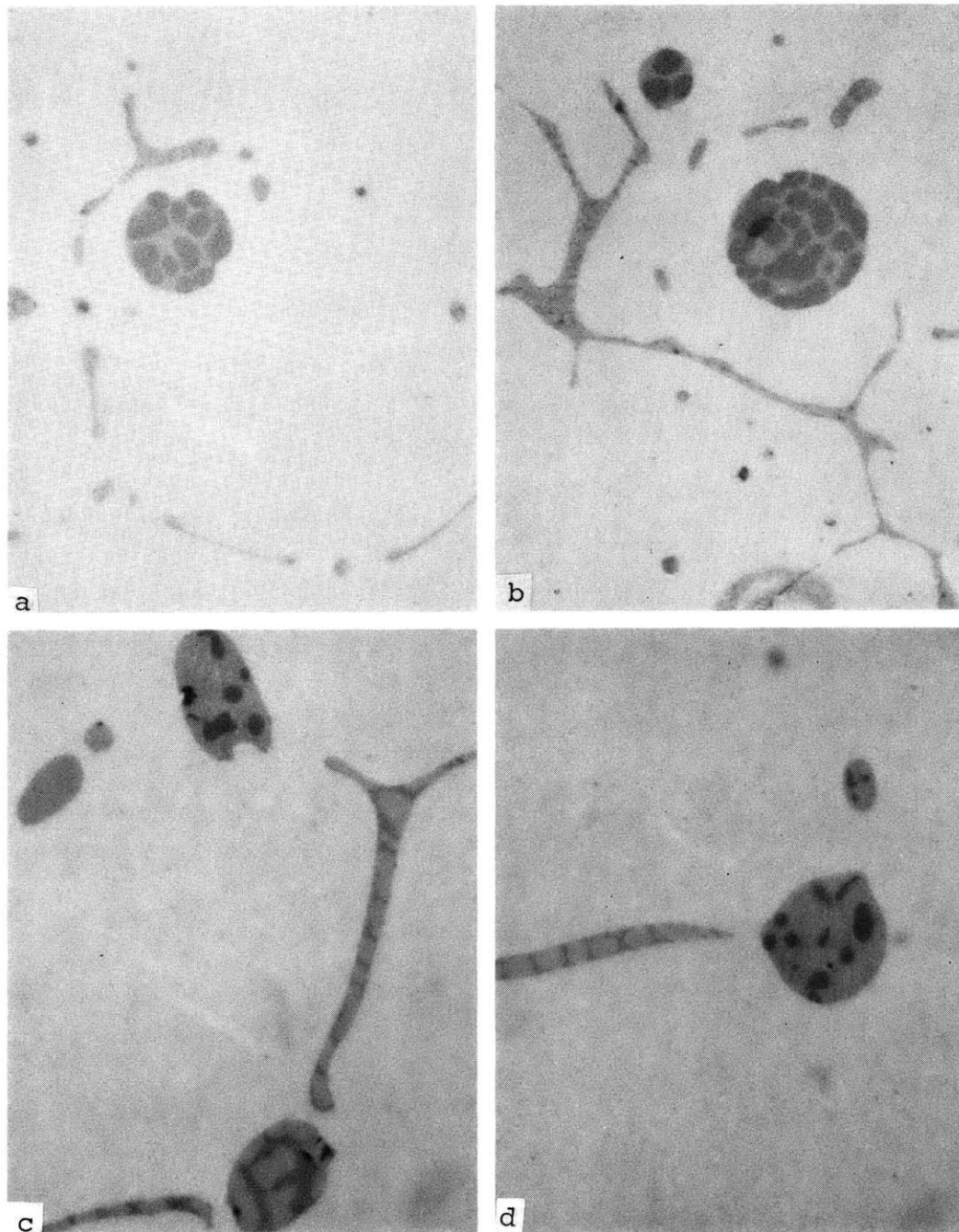


Figure 36: (a) and (b): Photomicrographs of an Fe-0.34% S-0.17% O alloy ( $O/S = 0.5$ ) solidified at  $1^{\circ}\text{C}/\text{sec}$ , unetched, 700X, showing the morphologies and relative positions of wustite rich and iron sulphide rich inclusions.

(c) and (d): Photomicrographs of an Fe-0.2% S-0.1% O alloy solidified at  $1^{\circ}\text{C}/\text{sec}$ , unetched, 1000X, showing the proximity of wustite rich and iron sulphide rich inclusions.

inclusions alloys of lower O/S ratios were examined in some detail.

No striking effect of O/S ratio on the two distinct types of inclusions was found. However, a tendency for more sulphide rich inclusions to appear spherical in form was noted at low O/S ratios. This trend is illustrated by Figure 37a which shows a number of spherical sulphide rich inclusions in an alloy of O/S ratio 0.125. On the other hand, the inclusions richest in sulphide, shown in Figure 37, remained sheet like in form and spherical wustite rich inclusions, such as the one illustrated in Figure 37c, still existed. At still lower O/S ratios, below 0.08, the wustite rich inclusions disappeared entirely leaving only a few roughly spherical sulphide rich inclusions surrounded by sheets of inclusions containing the maximum amount of iron sulphide. At O/S ratios below 0.05 all the inclusions were of the interdendritic sheet-like sulphide rich variety.

The O/S ratio has a noticeable effect on the proportion of inclusions which may be classified as spherical or sheet-like. This effect is illustrated by Figure 38 which shows alloys of two different O/S ratios at a magnification of 100X. Figure 38a shows an alloy of O/S ratio 0.10 in which the greater proportion of the inclusions are of the interdendritic sheet-like type. Figure 38b shows an alloy of only slightly higher O/S ratio, viz. 0.17, but it is plain that the greater proportion of inclusions appear spherical at least in cross section. A large number of the sheet-like

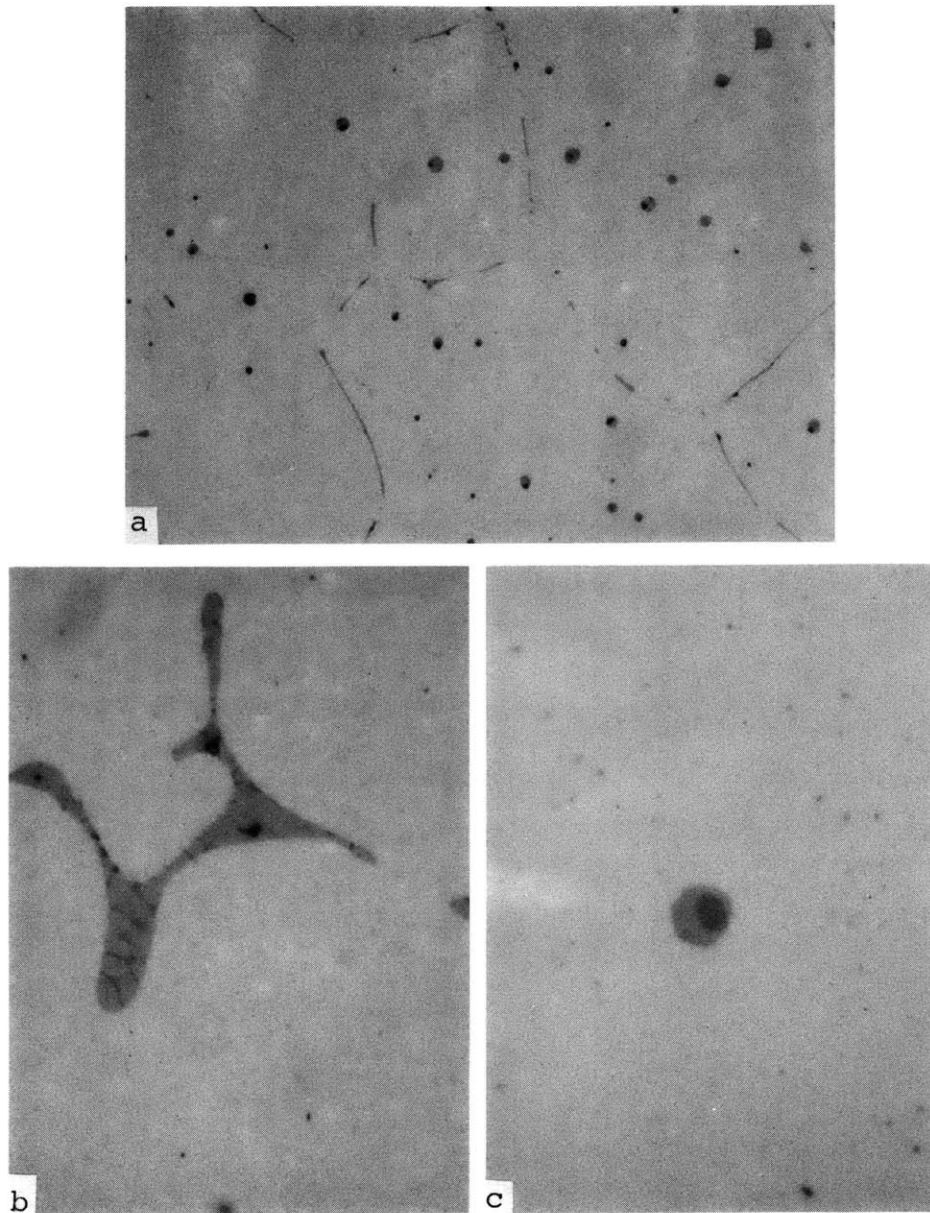


Figure 37: Photomicrographs of an Fe-0.4% S-0.05% O alloy ( $O/S = 0.125$ ) solidified at  $1^{\circ}\text{C}/\text{sec}$ , unetched, showing:

- (a) Inclusion morphology and distribution, 200X.
- (b) Morphology of an iron sulphide rich inclusion, 1000X.
- (c) Morphology of a wustite rich inclusion, 1000X.

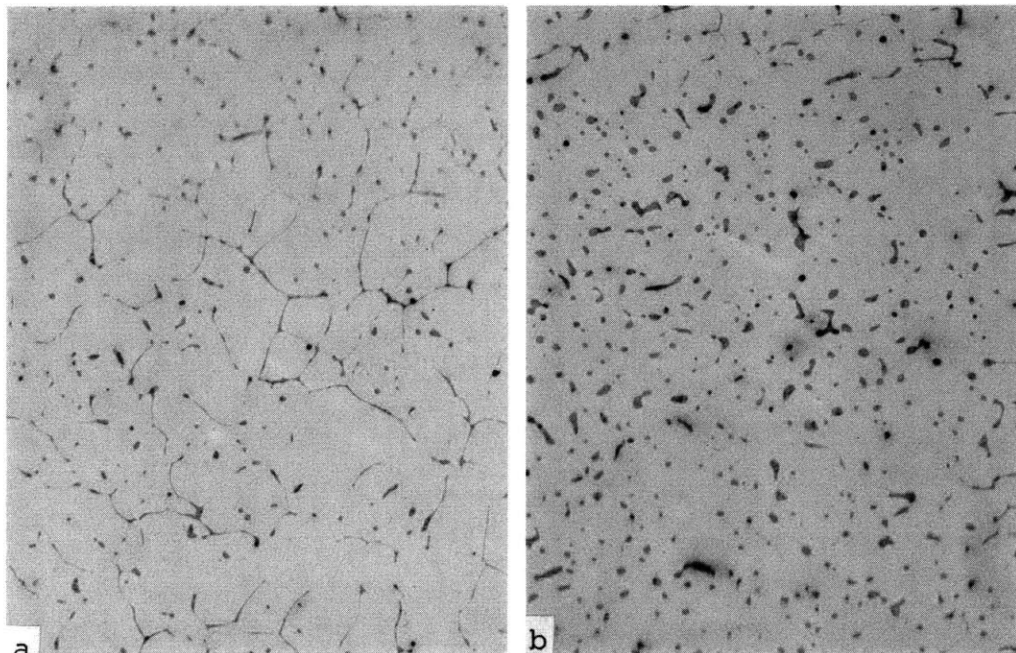


Figure 38: Photomicrographs of Fe-S-O alloys solidified at 10°C/sec, unetched, 100X; showing the effect of O/S ratio on inclusion morphology and distribution.

- (a) Fe-1.5% S-0.15% O, O/S = 0.10.
- (b) Fe-1.5% S-0.12% O, O/S = 0.17.

inclusions still appear but many of them have become restricted in extent and also thicker in cross section. As a result of these changes the dendritic pattern of the iron is much more difficult to discern than it is in Figure 38a.

In general it may be said that the higher the O/S ratio the greater the proportion of spherical wustite rich inclusions and the lower the extent of the interdendritic network of highly sulphide rich inclusions. However, the interdendritic inclusions persist even at high O/S ratios, albeit in minor amounts, whereas the wustite rich spherical inclusions disappear altogether at O/S ratios less than 0.08.

### 3. Effect of Solidification Rate

The inclusion morphologies and distributions described above all refer to alloys solidified at rates of a few degrees per second. Alloys solidified at greater rates were examined to reveal any effects on the morphology or distribution of inclusions.

It was found that increased solidification rate had little or no effect on inclusions, morphology and distribution. Figure 39 a and b show two sections of the same alloy, of O/S ratio 0.3, solidified at a rate estimated to be between 20 and 100°C/sec. It can be seen that the wustite rich inclusions still appear spherical in form and are positioned inside the dendrite arms. Also the iron sulphide rich inclusions retain their sheet-like morphology enveloping the dendrite arms.

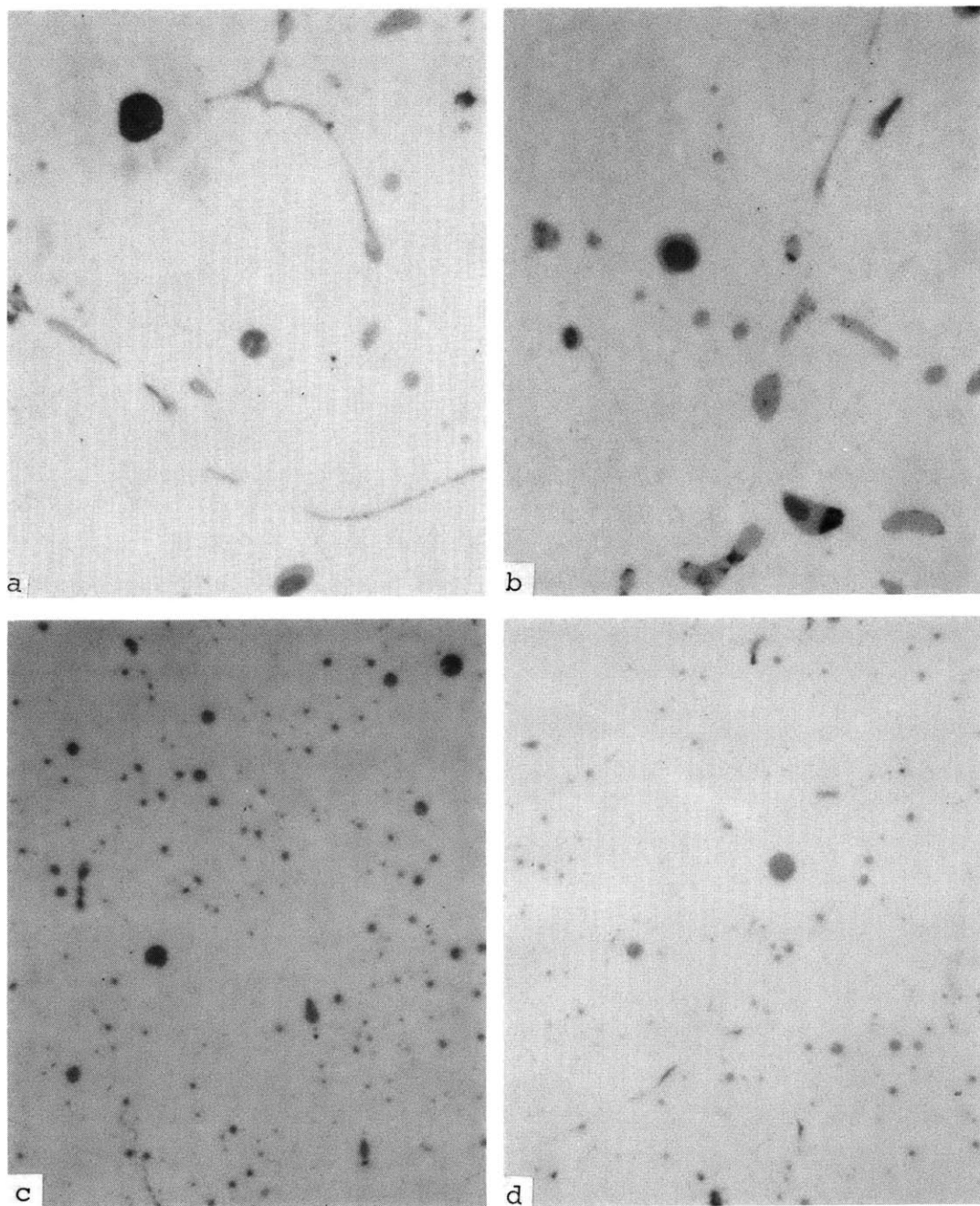


Figure 39: Photomicrographs of Fe-S-O alloys, unetched, 1000X, showing morphology and distribution of inclusion solidified at different rates.

- (a) and (b) Fe-0.5% S-0.15% O ( $O/S = 0.3$ )  
Solidified between 20 and  $100^{\circ}\text{C}/\text{sec}$ .
- (c) and (d) Fe-0.14% S-0.175% O ( $O/S = 1.25$ )  
Solidified at a rate in excess of  $100^{\circ}\text{C}/\text{sec}$ .

Photomicrographs c and d of Figure 39 shows two sections of an alloy, of higher O/S ratio, solidified at a rate in the neighborhood of  $100^{\circ}\text{C}/\text{sec}$ . The structure is sufficiently fine as to make identification of the inclusion compositions very difficult but close inspection shows that neither the morphology nor the distribution of the inclusions was affected by the increased rate of solidification.

## XIV. DISCUSSION

In Chapter VI two solidification models, the "equilibrium" model and the "isolation" model were constructed, based on the Fe-FeS-FeO phase diagram. Computer programs were written to facilitate the consideration of solidification of various liquids according to the dictates of these models. The resulting inclusion compositions, morphologies and distributions were determined. Summaries of these calculations are given on pages 102-106. To test these models, a series of solidification experiments was performed, the results of which are described in Chapter XIII. An analysis and interpretation of the experimental results in terms of the solidification models follows.

A. Inclusion Composition

The experimental results show that from the point of view of composition, two distinct types of inclusions are found in Fe-S-O microstructures. The first contains dendritic wustite in a matrix of iron sulphide-wustite eutectic and the second iron sulphide dendrites in the same eutectic matrix. An intermediate type containing only eutectic also exists. According to both solidification models the inclusions form by the freezing of pools of oxygen and sulphur rich liquid  $L_2$ . During freezing this liquid undergoes one of two eutectic reactions, which give solid iron, and wustite or iron sulphide, followed by a ternary eutectic reaction which gives solid iron, wustite and iron sulphide. Thus, the inclusions would be



expected to contain a binary eutectic in a ternary eutectic matrix. The explanation of this apparent anomaly is that the amounts of iron formed in both reactions are so small that it almost inevitably precipitates on the nearby iron dendrites which surround the small pools of  $L_2$  to form a divorced eutectic.

More detailed study of the microstructures show that inclusions with a range of compositions form during the solidification of Fe-S-O melts. A clear indication of this is given by the photomicrographs of Figure 34 which show inclusions of many different compositions found in a slowly solidified alloy.

This observation is in accord with the predictions made by consideration of the "isolation" model. This model suggests that during the course of the three-phase monotectic reaction, which occurs in freezing, pools of liquid rich in oxygen and sulphur are isolated by the solidifying iron. As the pools have a range of compositions, from high to low O/S ratio, the inclusions formed by the freezing of the pools must have a variety of compositions. On the other hand, the "equilibrium" model predicts that all inclusions must have the same composition, a forecast which clearly runs contrary to the experimental evidence.

It is of considerable interest to compare the qualitative experimental results of inclusion composition with those predicted by the "isolation" model. According to the model the important factor to be considered as a guide to the range

of inclusion compositions is the O/S ratio of the melt. The actual quantities of oxygen and sulphur involved being of lesser importance as these values are only expected to affect the amount of included matter and not its composition. Also, solidification rate would not be expected to have any effect on the inclusion composition range. It should be born in mind that the model cannot be applied to alloys of less than a certain minimum O/S ratio. This minimum ratio corresponds to the O/S ratio of the plait point which according to Hilty and Crafts<sup>12</sup> is 0.09 and according to Schurmann and von Hertwig<sup>46</sup> 0.043. Alloys of lower O/S ratio would not be expected to encounter the miscibility gap during freezing and consequently the "isolation" mechanism could not function.

The various predictions of the "isolation" model outlined above were tested experimentally; the results appearing in Chapter XIII. The predictions and experimental results are compared graphically below.

#### 1. Composition Range at Constant Cooling Rate

Figure 40 shows the range of inclusion compositions predicted by the "isolation" model based on the phase diagram of Hilty and Crafts<sup>12</sup>, for three O/S ratios. Points corresponding to the experimentally observed inclusion compositions for alloys of the same O/S ratios, solidified at approximately 1°C/sec, are also plotted for comparison. The agreement between predicted ranges and those determined by experiment is striking. The experimental data do in fact extend slightly beyond the predicted ranges for all three alloys but this is readily accountable in terms of experimental

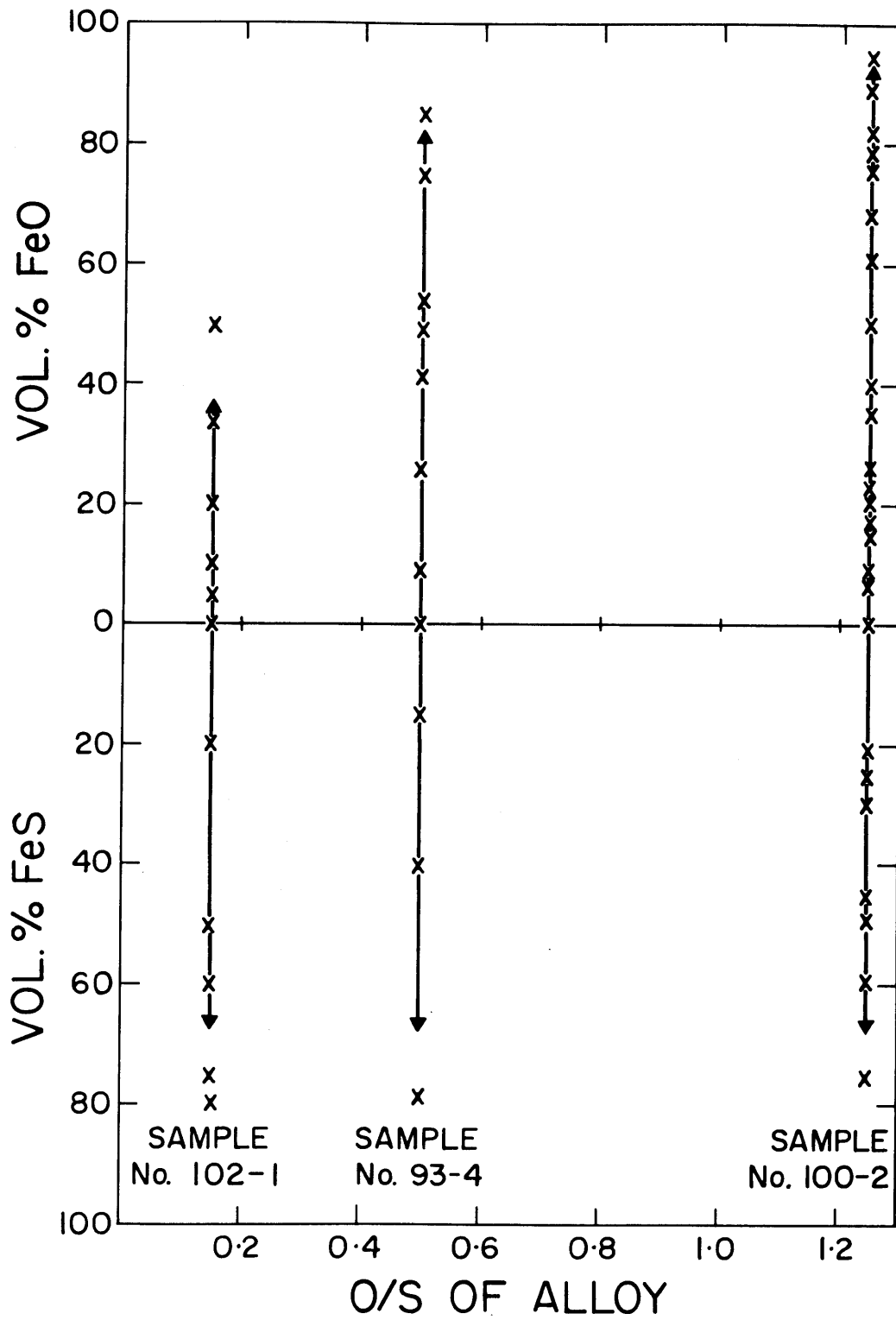


Figure 40. Observed inclusion composition range compared to the range predicted by the isolation model (indicated by the arrows) for alloys of three different O/S ratios, all solidified at  $\sim 1^{\circ}\text{C}/\text{sec}$ .

error and uncertainty in the phase diagram used as a basis for the model. In particular the extreme of the iron sulphide rich inclusion range is governed by the positions of the plait point and the ternary eutectic point. The position of the plait point is somewhat uncertain and it may be worth observing that use of the data of Schurmann and von Hertwig<sup>46</sup> would lead to better agreement at this end of the range. A maximum sulphide content of 80 percent by volume is predicted using the latter data.

The "isolation" model predicts that the maximum iron sulphide content of the inclusions should be constant whereas the maximum wustite content should increase with increasing O/S ratio. These two assertions are born out by the data presented in Figure 40 and listed in Table 7 of Chapter XIII. However, further observation of the maximum wustite content of the inclusions as a function of the melt O/S ratio were made in order to test the veracity of the "isolation" model in more detail. Figure 41 shows two plots of the maximum wustite content of inclusions, as a function of the O/S ratio, predicted by the "isolation" model; one based on the phase diagram of Hilty and Crafts<sup>12</sup> and the other on the diagram of Schurmann and von Hertwig<sup>46</sup>. Also included for comparison are plots of the inclusion composition predicted by the "equilibrium" model based on the two phase diagrams. The construction of this diagram is considered in detail in Chapter VI. Points corresponding to the experimentally determined maximum wustite contents of alloys solidified at approximately 1°C/sec, which are listed in Table 8 of Chapter XIII, are

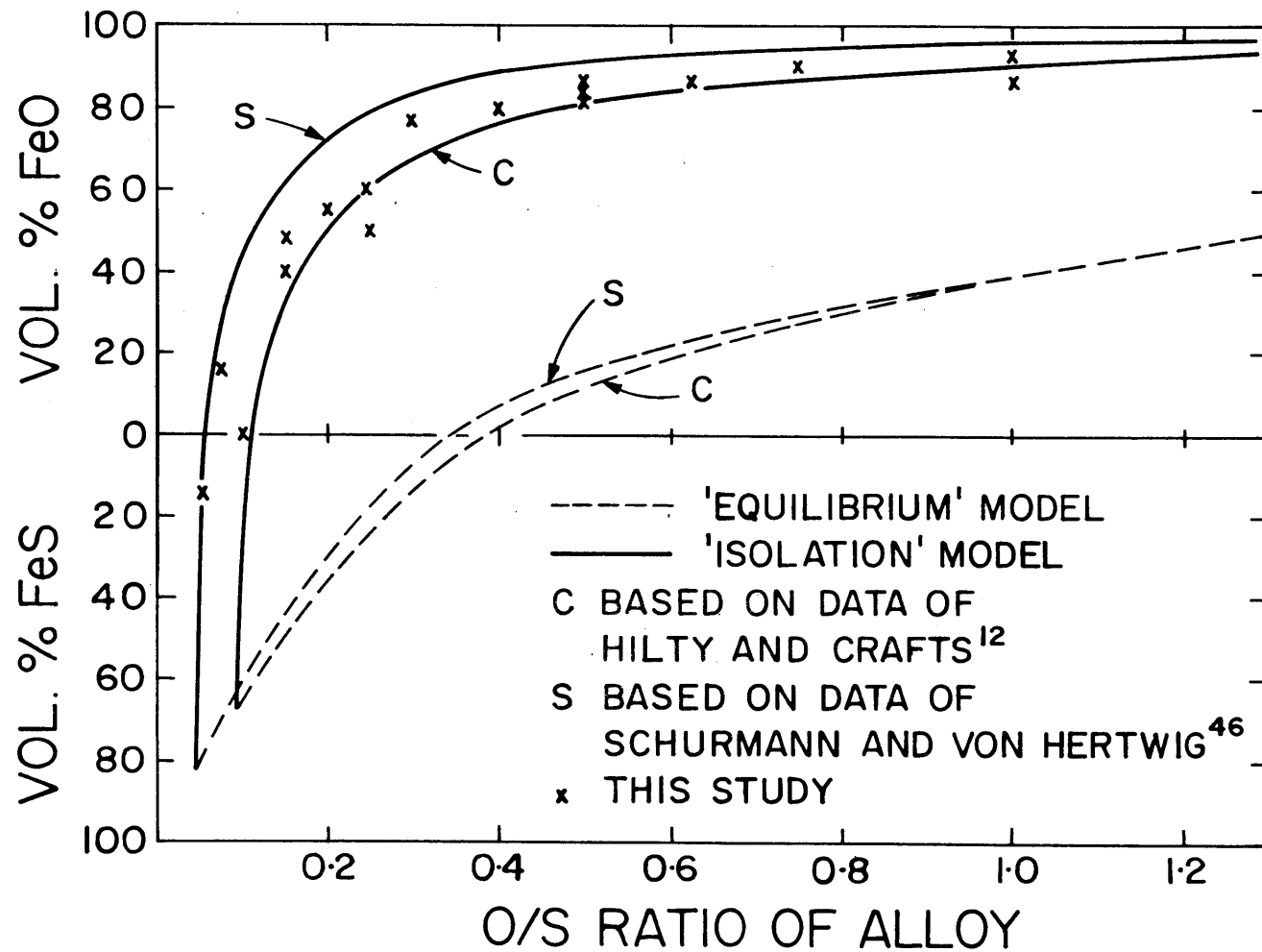


Figure 41. Observed maximum volume percent of FeO or minimum volume percent of FeS dendrites in the inclusions compared to those predicted by the equilibrium and isolation models for alloys having a range of O/S ratios and all solidified at  $\sim 1^{\circ}\text{C}/\text{sec}$ .

reported on the graph for ease of comparison with the predicted values. It can be seen that there is a good measure of agreement between the observed and predicted results, most data points lying between the two above mentioned "isolation" model curves.

Where more than one data point is reported for a particular O/S ratio melts of different compositions were made to test the effect of the actual sulphur and oxygen contents on the inclusion composition range. According to the "isolation" model no effect would be expected and in fact inspection of the data both on the graph and in its tabulated form reveals no consistent effect. Actually the observed wustite contents of inclusions for alloys of the same O/S ratio are equal within the limits of experimental accuracy.

No effect of solidification rate on the range of inclusion composition is predicted by the "isolation" model. Therefore, alloys of equal O/S ratio were solidified at different rates and the range of inclusion compositions measured in order to test this prediction. The results of these experiments are listed in Tables 9 and 10, Chapter XIII, and compared to the expected inclusion composition ranges for two O/S ratios in Figures 42 and 43. The data match the predicted composition ranges very well for all the alloys and solidification rates investigated. Some slight overlap exists at the high iron sulphide extreme of the ranges in these diagrams as it does in Figure 40. As in the case of Figure 40 the explanation for this could lie in the uncertain location of the plait point of the Fe-FeO-FeS phase diagram.

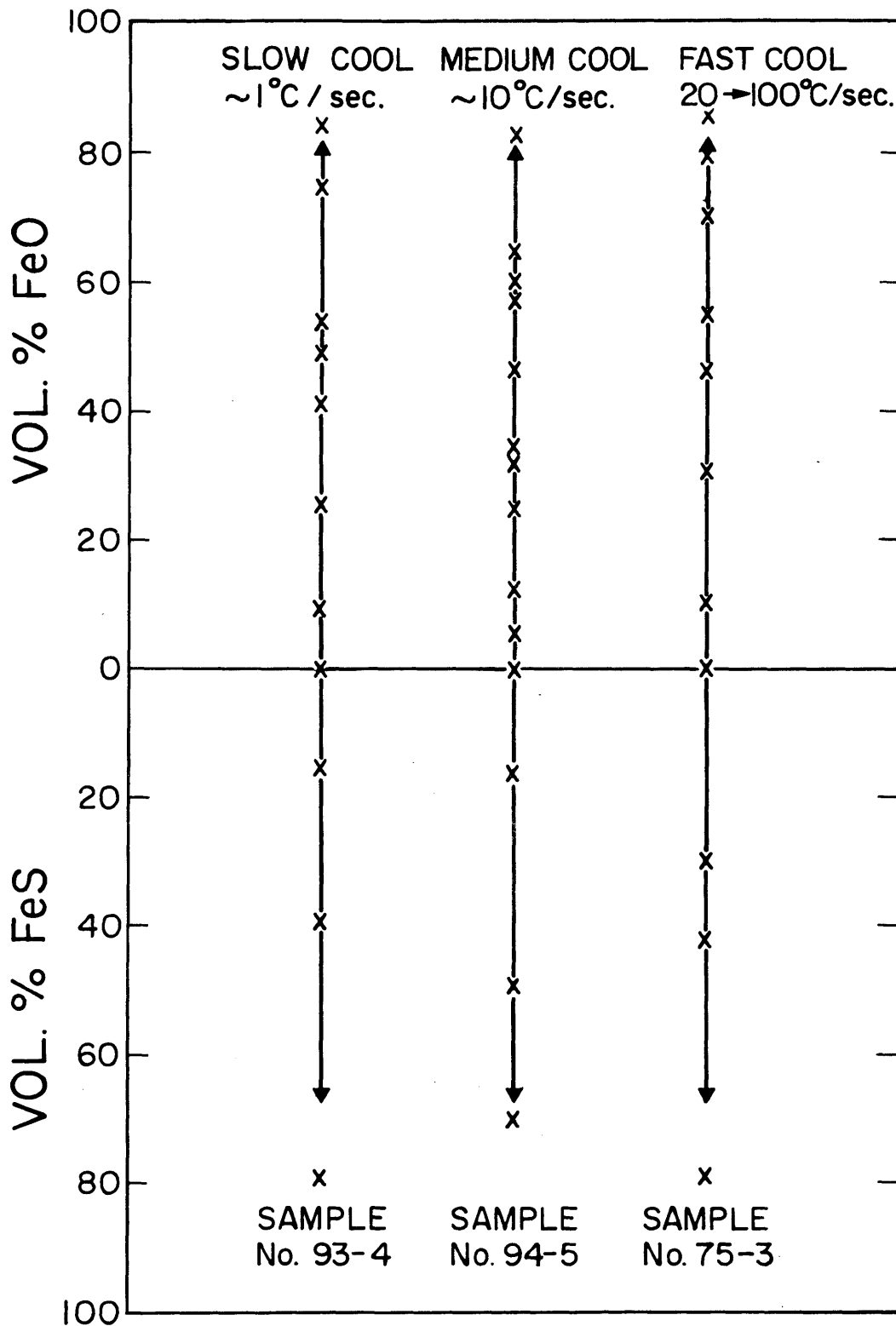


Figure 42. Observed range of inclusion composition for three alloys all having an O/S ratio of 0.5 but solidified at different rates, compared to the ranges predicted by the isolation model (indicated by arrows).

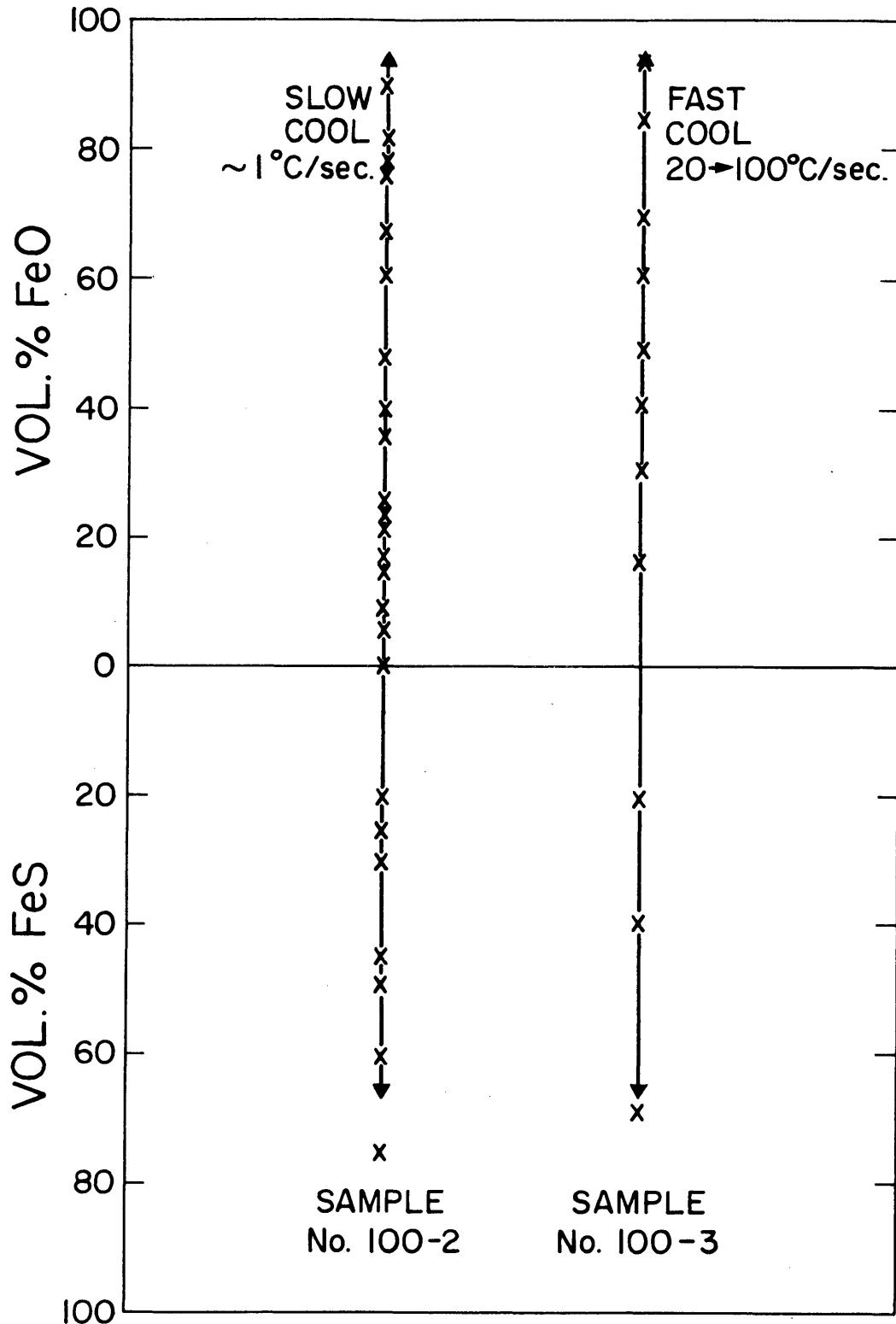


Figure 43. Observed range of inclusion composition for two alloys both having an O/S ratio of 1.25 but solidified at different rates compared to the ranges predicted by the isolation model (indicated by arrows).



## B. Morphology and Distribution of the Inclusions

The experimental results obtained in this study indicate that inclusions of different compositions are located in different positions relative to the iron dendrites and have a range of morphologies. A consequence of the "equilibrium" solidification model is that all inclusions are located interdendritically. Thus a poor correlation exists between the observed and predicted results for this model. On the other hand the "isolation" model requires that inclusion forming liquid be trapped inside the growing dendrites and it shows that some inclusions will appear interdendritically no matter what O/S ratio is chosen. Superficially the experimental results bear out these predictions and thus the correlation merits closer inspection.

According to the "isolation" model for alloys of O/S ratio greater than that of the plait point, the inclusions which form closest to the center line of the dendrite arms are richest in oxygen or poorest in sulphur. At increasing distances from the center lines inclusions richer in sulphur and poorer in oxygen are formed. Finally the interdendritic spaces are filled with iron sulphide rich inclusions having the highest sulphur content of all. For alloys of O/S ratio less than that of the plait point all the inclusions appear as interdendritic filling.

The O/S ratio also determines the actual composition range of the inclusions and as a consequence the inclusions

closest to the center lines of the dendrite arms may be richest in wustite or poorest in iron sulphide depending on the actual value of the O/S ratio.

Perhaps the most graphic illustration that these predictions are born out by the experimental results is offered by Figure 36. Photomicrographs a and b in this figure show wustite rich inclusions located inside the dendrites which in turn are almost completely enveloped by iron sulphide rich inclusions. In general, the experimental results show that inclusions richest in oxygen are located inside the dendrites whilst those richest in iron sulphide form the interdendritic filling. This observation is in complete agreement with the predictions arrived at from consideration of the "isolation" model.

The experimental results also indicate that at lower O/S ratios a greater proportion of included matter is concentrated into the interdendritic spaces than is the case for high O/S ratios. This too is in agreement with the predicted results of the "isolation" model. At high O/S ratios the majority of the oxygen and sulphur rich liquid,  $L_2$ , is formed at the beginning of the monotectic three-phase reaction and hence is trapped deep inside the iron dendrites. Relatively minor amounts of  $L_2$  are precipitated towards the end of the reaction when the melt is almost completely solid. As the O/S ratio of the melt considered decreases less  $L_2$  is formed early in the monotectic reaction and proportionately more towards the end. As the  $L_2$  solidifies to form the

inclusions this means that they are distributed in a like manner to  $L_2$ ; in agreement with the experimental observations.

Variation of freezing rate is not expected to have any effect on the distribution of inclusions as predicted by the "isolation" model. This expectation is born out in practice as shown by Figure 39 of Chapter XIII.

Neither solidification model makes any specific predictions as to the morphology of the inclusions; however, some limited conclusions may be drawn from the predicted location of the inclusions and the manner in which they form. According to the "equilibrium" model all inclusions form from the interdendritic liquid remaining at the completion of the monotectic reaction. The morphologies of such inclusions would be influenced strongly by the shape of surrounding dendrites and consequently a more or less continuous network of inclusions would be expected. The amount of iron precipitated during the freezing of  $L_2$  is quite small, of the order of 3 percent or less by volume and so the morphology of the inclusions would be closely related to that of the liquid from which they formed. Little more can be said in the absence of interfacial tension data.

The above reasoning would explain the morphology of the interdendritic inclusions observed experimentally but not that of the spherical or near spherical inclusions, located inside the dendrite arms. The "equilibrium" model must therefore be rejected as an explanation of inclusion morphology.

The "isolation" model locates inclusions both interdendritically and inside the dendrite arms. The interdendritic generation of inclusions would be expected to form a network pattern in the same way as the "equilibrium" model inclusion. The morphology of the inclusions set into the dendrite arms would be expected to depend largely on the shape of the  $L_2$  pools from which they formed as the quantities of iron precipitated during freezing of the pools are very limited. The actual form which  $L_2$  would assume is a matter for conjecture so long as no interfacial tension data exists for the  $\alpha/L_1$ ,  $\alpha/L_2$  and  $L_1/L_2$  interfaces. However, the adoption of a more or less spherical geometry would aid the subsequent entrapment of the pool. (See Chapter VI, page 87.) Thus the fact that in practice near spherical inclusions of high oxygen content are found located inside the dendrite arms in no way contravenes the predictions of the "isolation" model.

The preceding analysis of the experimental results shows that inclusion compositions, their morphologies and their distributions in the solidified alloys are best described by the "isolation" solidification model.

## XV. SUMMARY AND CONCLUSIONS

The processes underlying the formation of inclusions in the Fe-FeO-FeS system have been investigated. The system is dominated by a miscibility gap in the liquid region which extends from Fe-FeO binary into the ternary field up to about 20 percent sulphur. It has been shown that iron alloys having an O/S ratio greater than 0.05 encounter the miscibility gap during freezing. Two models simulating the possible processes of solidification and inclusion formation involving the miscibility gap were constructed. The first or "equilibrium" model assumes complete equilibrium between the solid iron and the two immiscible liquids during solidification. The second or "isolation" model assumes entrapment of the oxygen-sulphur rich liquid, formed because of the presence of the miscibility gap, in the solidifying iron. This entrapped liquid, while remaining in equilibrium with the surrounding solid iron, is prevented from maintaining equilibrium with the liquid iron by the solid iron which acts as a barrier to mass transport. The inclusion compositions and their locations in the solid sections were determined for each model.

Experiments were performed in which levitated melts of various O/S ratios were equilibrated and solidified over a range of cooling rates. The solidified samples were sectioned, polished and examined by standard metallographic techniques in order to reveal the composition, location and morphology of the inclusions. The results of these

determinations were compared to those predicted from the "equilibrium" and "isolation" models.

The compositions, locations and morphologies observed from experiment agree with those determined from the "isolation" model. In all cases, for alloys having O/S ratios greater than 0.05, the inclusions showed a range of compositions corresponding to a range of O/S ratios. The upper limit of this range depends on the O/S ratio of the original melt and the lower limit corresponds to the O/S ratio of the plait point which is the minimum temperature point of the miscibility gap. Inclusions of high O/S ratio exist in the form of globules set inside the iron dendrites whereas the inclusions with the lowest O/S ratio form an interdendritic network. Alloys having an O/S ratio less than 0.05 solidify in a simple eutectic manner and contain interdendritic inclusions of a single composition.

The results indicate that during solidification of iron containing oxygen and sulphur, liquid pools rich in oxygen and sulphur are entrapped by the growing iron dendrites and isolated from liquid iron. This phenomenon results in the liquid iron enriching in sulphur up to the plait point of the miscibility gap and then solidifying as an interdendritic network of inclusions. Solidification of the entrapped oxygen-sulphur rich pools results in the formation of other inclusions having a range of compositions.

## XVI. SUGGESTIONS FOR FURTHER WORK

A. The Levitation Apparatus

With the present experimental set-up it is not possible to measure temperatures of iron much in excess of  $1700^{\circ}\text{C}$ . This is because the dense fumes, emanating from the levitated iron at these high temperatures, are swept upwards through the Vycor furnace tube into the optical path of the pyrometer by the gas flow (see Figure 5). If the gas flow were reversed this problem would be solved and experiments similar to those described in Chapter III of this study could be performed at temperatures in excess of  $1700^{\circ}\text{C}$ . Argon-helium mixtures would have to be used as atmospheres because the thermal conductivity of pure helium is too great to allow the attainment of such high temperatures with the present apparatus.

In solidification experiments the cooling rate applied to the sample may be important; for instance the affect of cooling rate on inclusion size is of considerable interest. With the present apparatus cooling rates from  $1^{\circ}\text{C}/\text{sec}$  up to about  $20^{\circ}\text{C}/\text{sec}$  can be attained by gas flow cooling and measured with the two-color pyrometer. Higher cooling rates can be achieved by casting the molten metal into chill molds or into a liquid quenching bath. However, the actual rates may only be estimated with the present equipment. The use of thermocouples to measure the temperature changes at the mold metal

interface or in the quenching bath liquid could be used to determine the quench rate. This would represent a considerable advance in the usefulness of the apparatus.

#### B. The Fe-FeO-FeS System

In this study it was shown that large compositional differences exist between inclusions separated by distances shorter than the secondary dendrite arm spacing. It would be interesting and informative to study the effect of heat treating cycles on such inclusions. Sulphur and oxygen would be expected to diffuse through the solid iron to restore chemical equilibrium. Also the changing surface energies would be expected to result in changes in inclusion morphology.

#### C. Other Systems

Manganese is the most common alloying addition to sulphur bearing steels and its strong affinity for sulphur results in the formation of many inclusions which are basically manganese sulphides. The present work, on the Fe-FeO-FeS system, if taken together with a similar study of the Fe-Mn-S system could be used as the basis for a study of the complex Fe(Mn)-S-O system. Hilty and Crafts<sup>58</sup> have proposed a pseudoternary solidification diagram for the Fe-S-O system modified by manganese which could be of considerable help in understanding inclusion formation in this system.



D. Interfacial Tension

A need exists for interfacial tension measurements in metal slag systems. Data of this sort could be used in gaining an understanding of inclusion nucleation and morphology which is impossible with the present limited and inaccurate data.

## XVII. BIBLIOGRAPHY

1. Report of the U. S. Bureau of Standards, Chemical and Metallurgical Engineering, 26, 778 (1922).
2. F. S. Tritton and D. Hanson, J. Iron and Steel Inst., 110, 90 (1924).
3. C. H. Hertzy, Jr. and J. M. Gaines, Trans. A.I.M.E., Iron and Steel Technology in 1928.
4. F. Korber, Stahl und Eisen, 52, 133 (1932).
5. F. Korber and W. Oelsen, Mitt. Kaiser Wilhelm Inst. Fur Eisenforsch., 14, 181 (1932).
6. J. Chipman and K. L. Fetters, Trans. A.S.M., 29, 953 (1941).
7. C. R. Taylor and J. Chipman, Trans. A.I.M.E., 154, 228 (1943).
8. W. A. Fischer and H. vom Ende, Arch. Eisen., 23, 21 (1952).
9. N. A. Gokcen, Trans. A.I.M.E., 206, 1558 (1956).
10. E. S. Tankins, N. A. Gokcen and G. R. Belton, Trans. A.I.M.E., 230, 820 (1964).
11. W. A. Fischer and W. Ackermann, Arch. Eisen., 38, 1 (1967).
12. D. C. Hilty and W. Crafts, Trans. A.I.M.E., 196, 1307 (1952).
13. H. L. Hamner and R. M. Fowler, Trans. A.I.M.E., 194, 1313 (1952).
14. W. A. Fischer and W. Ackermann, Arch. Eisen, 36, 643 (1965).
15. W. A. Fischer and W. Ackermann, Arch. Eisen, 37, 779 (1966).
16. E. Okness, D. Wroughton, G. Comenetz, P. Brace and J. Kelly, J. Appl. Phys., 23, 545 (1952).
17. E. Fromm and H. Jehn, Brit. J. Appl. Phys., 16, 653 (1965).

18. R. W. Strachan, Ph.D. Thesis, M.I.T. (1967).
19. S. Y. Sherashi and R. G. Ward, *Can. Met. Quarterly*, 3, 117 (1964).
20. H. Larson, Sc.D. Thesis, M.I.T. (1967).
21. P. Kozakevitch, Proc. of the Symposium on Liquids, Structure, Properties, Solid Interaction. G. M. Res. Labs., Warren, Michigan (1963), Elsevier, Amsterdam (1965).
22. T. P. Floridis and J. Chipman, *Trans. A.I.M.E.*, 204, 549 (1958).
23. C. Wagner, Thermodynamics of Alloys, Addison Wesley, Cambridge, Mass. (1952).
24. H. Schenck, M. G. Froberg and E. Steinmetz, *Arch. Eisen.*, 31, 671 (1960).
25. C. H. P. Lupis and J. F. Elliott, *Acta Met.*, 15, 265 (1967).
26. W. B. Eisen, Ph.D. Thesis, M.I.T. (1968).
27. J. F. Elliott, M. Gleiser and V. Ramakrishna, Thermochemistry for Steelmaking, 2, A.I.S.I. (1963).
28. C. E. Sims, *Trans. A.I.M.E.*, 215, 367 (1959).
29. M. Baeyertz, Non-Metallic Inclusions in Steel, A.S.M., Cleveland, Ohio (1947).
30. C. Benedicks and H. Lofquist, Non-Metallic Inclusions in Iron and Steel, Chapman and Hall, London (1930).
31. H. Wentrup, *Tech. Mitt. Krupp*, 5, 131 (1937).
32. C. R. Wohrman, *Trans. Am. Soc. Steel Treating*, 14, 542 (1928).
33. R. Kiessling and N. Lange, Non-Metallic Inclusion in Steel, Iron and Steel Institute, Special Reports No. 90 (1964), No. 100 (1966) and No. 115 (1968).
34. C. E. Sims and G. A. Lilliequist, *Trans. A.I.M.E.*, 100, 154 (1932).
35. C. E. Sims, H. A. Saller and F. W. Boulger, *Trans. Am. Foundry Soc.*, 57, 233 (1949).

36. W. Dahl, H. Hengstenberg and C. Duren, *Stahl und Eisen*, 86, 782 (1966).
37. L. H. Van Vlack, *Trans. A.I.M.E.*, 191, 251 (1951).
38. A. S. Keh and L. H. Van Vlack, *Trans. A.I.M.E.*, 206, 950 (1956).
39. W. Crafts and D. C. Hilty, *Proc. Elec. Furnace Steel Conference*, 121 (1953).
40. W. Crafts, J. L. Egan and W. D. Forgeng, *Trans. A.I.M.E.*, 140, 233 (1940).
41. L. S. Darken and R. W. Gurry, *J. Am. Chem. Soc.*, 68, 799 (1946).
42. J. Chipman, *Metals Handbook*, A.S.M. Cleveland, Ohio (1948).
43. T. Rosenquist and B. L. Dunicz, *Trans. A.I.M.E.*, 194, 604 (1952).
44. P. Asanti and E. J. Kohlmeyer, *Z. Anorg. Chem.*, 265, 94 (1951).
45. R. Vogel and W. Fulling, *Festschriftan J. Arvid Hedvall*, 597 (1948).
46. E. Schurmann and I. O. von Hertwig, *Giesserei Techn.-Wiss. Beihefte*, 14, 31 (1962).
47. Ya. I. Ol'Shanskii, *Doklady Akad. Nauk S.S.S.R.*, 70, 47 (1950).
48. Ya. I. Ol'Shanskii, *Doklady Akad. Nauk S.S.S.R.*, 80, 893 (1951).
49. G. H. Gulliver, *J. Inst. Metals*, 9, 120 (1913).
50. E. Scheil, *Z. Metallk.*, 34, 70 (1942).
51. W. G. Pfann, *Trans. A.I.M.E.*, 194, 747 (1952).
52. H. D. Brody and M. C. Flemings, *Trans. A.I.M.E.*, 236, 615 (1966).
53. T. F. Bower, H. D. Brody and M. C. Flemings, *Trans. A.I.M.E.*, 236, 624 (1966).
54. T. Kuwabara and J. F. Elliott, *Trans. A.I.M.E.* (to be published).

55. T. F. Allmand, Microscopic Identification of Inclusions in Steel, B.I.S.R.A., London (1962).
56. J. H. Swisher and E. T. Turkdogan, Trans. A.I.M.E., 239, 426 (1967).
57. J. E. Hilliard and J. W. Cahn, Trans. A.I.M.E., 221, 344 (1961).
58. D. C. Hilty and W. Crafts, Trans. A.I.M.E., 200, 959 (1954).

## APPENDIX A

## Calibration of the Pyrometer

1. Experimental Technique

Samples of Ferrovac-E iron were prepared and levitated in much the same way as described in Chapter V. With the pyrometer in its normal operational mode, the gas flow was controlled so that successive cycles of melting and freezing were produced. The temperature corresponding to each melting and recalescence point was recorded. This procedure was repeated for several samples of iron until one hundred determinations of the fixed point had been made.

2. Calculation of the Standard Deviation

The results of the experiments are shown graphically in Figure A.1. The standard deviation is defined as:

$$\sigma = \sqrt{\frac{\sum d^2}{k}} \quad (\text{A.1})$$

where:  $d$  = deviation from the mean

$k$  = the number of measurements.

It can be shown that in this case  $\sigma = 5^{\circ}\text{C}$ .

This means that if a Gaussian distribution is assumed then the probability of the result or melting point being within  $\pm 5^{\circ}\text{C}$  of the average  $1533^{\circ}\text{C}$  is 68.3% and the probability of its being within  $\pm 10^{\circ}\text{C}$  is 95.4%. Thus it can be said, with

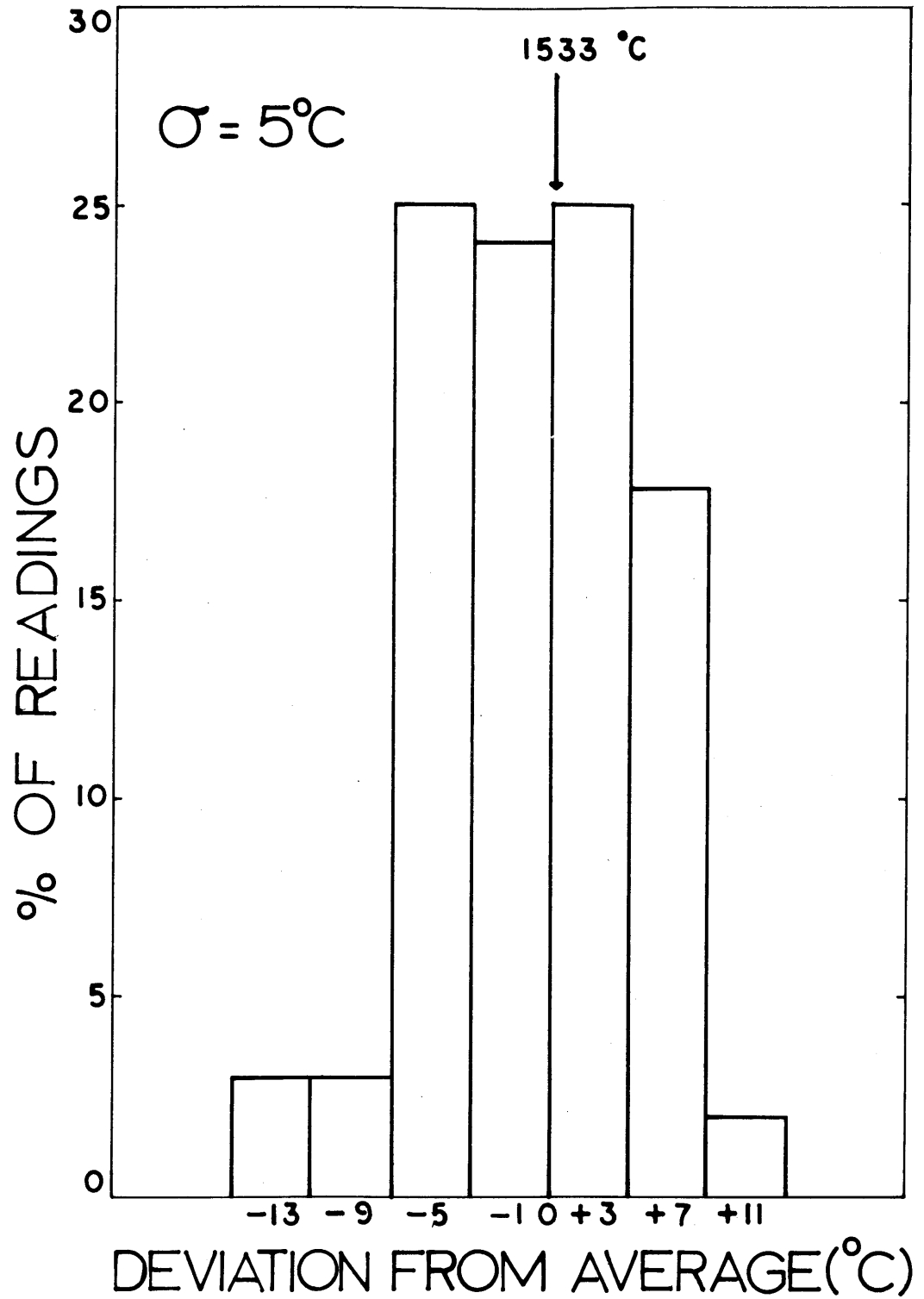


Figure A1. Distribution of melting point readings about the mean.

some confidence, that the deviation of the pyrometer is  $\pm 10^{\circ}\text{C}$ . Although this is only strictly true for measurements close to the melting point, the relative insensitivity of the two-color pyrometer to changes of emissivity should not lead to significantly greater error when reading within two hundred degrees centigrade of this point.

Therefore, as the true melting point of iron was taken to be  $1536^{\circ}\text{C}$ , the pyrometer was assumed to read  $3^{\circ}\text{C}$  low over the range covered with a deviation of  $10^{\circ}\text{C}$ .

The calibration was checked monthly in the same way as the original calibration was carried out.



## APPENDIX B

## Materials

The iron used in this study was Ferrovac-E iron supplied by Crucible Steel Company in the form of half inch rod. The lot analysis is given in Table B.1.

Table B.1

## Lot Analysis of Ferrovac-E Iron

	wt. pct.		wt. pct.
C :	0.005 - 0.01	N :	0.0002 - 0.00085
Co:	0.0006 - 0.005	Ni:	0.02 - 0.02
Cr:	0.006 - 0.01	O :	0.0002 - 0.003
Cu:	0.006 - 0.01	P :	0.002 - 0.003
Mn:	< 0.0005 - 0.001	S :	0.003 - 0.005
Mo:	0.001 - 0.01	Si:	0.006 - 0.006

The iron sulphide was supplied by Rocky Mountain Research Inc. X-ray analysis revealed only the FeS phase<sup>26</sup>.

Iron oxide in the form of reagent grade ferric oxide (>99.5%) supplied by Baker and Adamson was used as the source of oxygen.

## APPENDIX C

## Sample Preparation for Optical Metallography

Firstly the mounted samples were slowly and carefully "coarse" ground. This was followed by medium and fine grinding on wheels with 240, 320 and 600 wet papers, applying light but positive pressure at all times. The samples were then polished on three wheels. The first two; six and one micron diamond wheels, were covered with Buehler "First Quality Microcloth". A final light polish on a wheel covered with Selvyt Cloth, impregnated with 0.05 micron "Linde B Alumina" completed the operation.

The samples were rotated at all times during the polishing operation. This, and the fact that the diamond wheels were covered with a napless cloth helped prevent fragmentation and the dragging out of the inclusions. Despite all these precautions some of the inclusions, and particularly the oxide phase in the inclusions, became dislodged during polishing.

## APPENDIX D

## Solubility of Oxygen in Undercooled Iron

Fischer and Ackermann<sup>11</sup> express the solubility of oxygen in undercooled iron under a silica saturated slag by the following equation:

$$\log (\%O)^* = -4065/T + 1.116 \quad (D.1)$$

where \* refers to silica saturation

The activity of FeO in the slag may be written as follows:

$$a_{FeO}^* = (\%O)^*/(\%O)' \quad (D.2)$$

where ' refers to equilibrium with a pure FeO slag.

Thus:

$$\log (\%O)' = \log (\%O)^* - \log a_{FeO}^* \quad (D.3)$$

By substituting a reliable value for  $\log a_{FeO}^*$  at any relevant temperature into equation (D.3) the results of Fischer and Ackermann<sup>11</sup> may be compared to those obtained in the present work. Values for  $a_{FeO}^*$  at silica saturation are available at two temperatures; 1350°C and 1600°C.<sup>27</sup>  $a_{FeO}^*$  decreases only slightly over this temperature range; from 0.37 to 0.36, and so a linear interpolation was used to compute  $a_{FeO}^*$  as a function of temperature. The values of  $a_{FeO}^*$  obtained were substituted into equation (D.3) and the results plotted in Figure D.1. Thus both the results of the present study and those of Fischer and

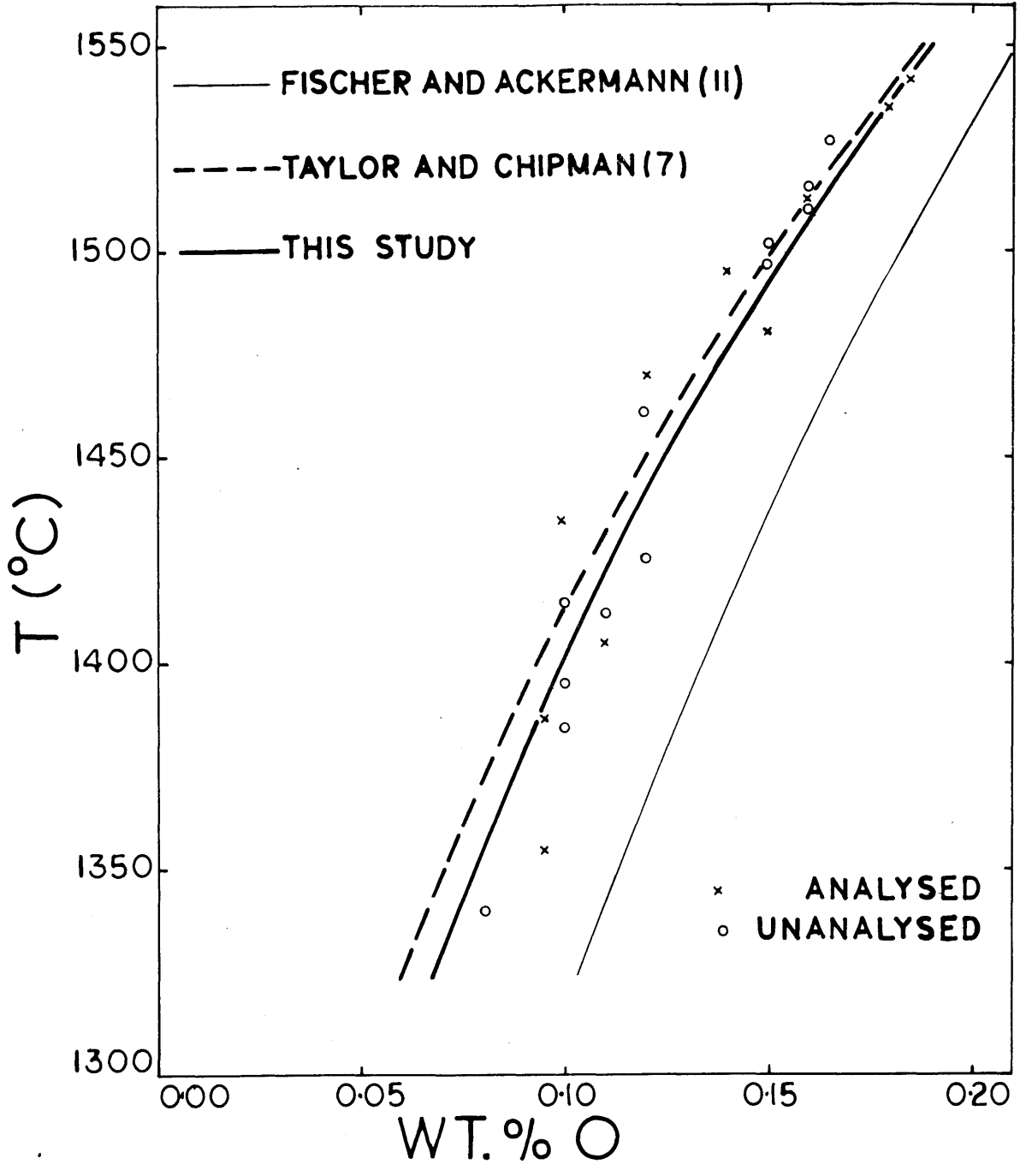


Figure D1. Solubility of oxygen in undercooled liquid iron. The line of Fischer and Ackermann<sup>11</sup> comes from equation D1 corrected to  $a_{FeO} = 1$ .

Ackermann<sup>11</sup>, as they expressed in Figure D1, refer to oxygen solubility in equilibrium with pure FeO.

It can be seen from this figure that the results of the present study agree quite closely with the line of Taylor and Chipman<sup>7</sup> extrapolated from above the melting point. However, a difference of approximately 0.003% exists between the present results and those of Fischer and Ackermann<sup>11</sup> over the whole temperature range. It is difficult to draw any conclusion from this as the experiments are not directly comparable and the discrepancies may well lie in the adjustment of the activity of FeO.

## APPENDIX E

## Solubility of Sulphur and Oxygen in Solid Iron

In the formulation of the solidification models it is assumed that there is no solubility of sulphur or oxygen in solid iron. The dissolution of large amounts of oxygen and/or sulphur in the solid iron would have the effect of reducing the proportions of these elements available for inclusion formation to such an extent that the models would have to be modified to take it into account. The validity of the assumption of zero solid solubility is discussed herein.

Under the condition of "non-equilibrium" solidification, where diffusion in the solid phase is taken as zero, the amount of a solute element retained by the solidifying iron may be found using the partition ratio  $k$ . This is the ratio of the solute concentration in the solid phase to that in the liquid phase at the interface, and is in general a function of temperature. Phase diagram data<sup>42,43</sup> were used to calculate an average partition ratio  $k$  for sulphur in the  $\delta$  iron range of 0.02. The partition ratio  $k'$  of oxygen in  $\delta$  iron is given as 0.05 by Swisher and Turkdogan<sup>56</sup>. Solubility of oxygen and sulphur in  $\gamma$  iron is much less than in  $\delta$  iron and it decreases rapidly as the temperature falls. For this reason and because it was shown that most of the iron solidifies in the  $\delta$  iron range solution of oxygen and sulphur in  $\gamma$  iron is neglected in the following calculations.

Dissolution of oxygen and sulphur in iron is not expected to influence the rate of increase of  $f_\alpha$  (wt. fraction of solid iron) during freezing to a first approximation, so the results of the computer programs, described in Chapter XI, may be used in estimating the quantities of solute elements taken into solution in  $\delta$  iron. Two representative alloys were considered, the first having a high O/S ratio of 1.68 (0.168%O, 0.10%S) and the second having a low O/S ratio of 0.16 (0.32%O, 2.0%S).

The computer outputs for both "equilibrium" and "isolation" solidification give  $f_\alpha$  as a function of composition of  $L_1$  ( $C_{L_1}$ ,  $C'_{L_1}$ ) and the temperature. The concentrations of sulphur and oxygen in the solid at the interface  $C_S^*$ ,  $C_S^{*}$  are given by  $kC_{L_1}$  and  $k'C'_{L_1}$ . Considerations of the average value of  $C_{L_1}$  and  $C'_{L_1}$  over small intervals of freezing  $\Delta f_\alpha$  allows the estimation of the quantities of oxygen and sulphur taken into solution in each small fraction  $\Delta f_\alpha$ . Summation of these quantities over the complete  $\delta$  range enables one to calculate the amounts of oxygen and sulphur dissolved in the metal as a percentage of the original solute content of the melt. The proportions of the solute elements retained by the iron dendrites proved to be independent of the original melt composition over the wide range of O/S ratios considered, to all intents and purposes. For all the cases considered it was found that between 5 and 7% of the total sulphur and between 4 and 5% of the oxygen would be retained by the solidifying

iron. These quantities are quite negligible for considerations of inclusion formation.

In the calculations outlined above diffusion in the solid  $\alpha$  phase was neglected. This may not always be a good assumption and Brody and Flemings<sup>52</sup>, recognizing this, proposed a modification of the Scheil equation incorporating the factor  $\alpha k = (D_S t_F k / L^2)$ . In this expression  $D_S$  is the average diffusion coefficient of the solute element in the solid over the freezing range,  $t_F$  is the local solidification time and  $L$  is half the dendrite arm spacing. This factor can be used to estimate the extent of diffusion in the solid under the conditions which they describe. The diffusion paths are sufficiently different in the present case, due to the presence of a third phase  $L_2$  which is sometimes assumed to be trapped inside the growing dendrites, that the factor  $\alpha k$  cannot be used to predict the extent of diffusion with any confidence. However, it is possible to predict the maximum amount of the solute elements retained by the  $\alpha$  dendrites in solidification under conditions of complete diffusion.

The sulphur concentration in  $L_1$  ( $C_{L_1}$ ) builds up to a high level before the  $\delta \rightarrow \gamma$  transformation temperature is reached and under conditions of complete equilibrium all sulphur in melts containing less than about 0.13% S would be retained by the solidified iron. However, alloys having sulphur contents of this order were found experimentally to contain large quantities of FeS in interdendritic inclusions. This observation indicates that the effects of diffusion are quite small



and so assumption of zero solubility of sulphur should not affect the validity of the models to a significant extent.

The maximum oxygen content of the iron dendrites under conditions of complete equilibrium would be 0.03 assuming that the partition ratio of 0.05 holds down to the  $\delta \rightarrow \gamma$  transformation temperature. This is about 18% of the minimum oxygen content of melts considered in the models. Thus, depending on the extent of diffusion, between 5% and 18% of the oxygen content of the melt would be retained by the iron dendrites during solidification. Dissolution of even the maximum amounts of solute elements considered feasible above would not alter the essential features of the solidification models discussed in Chapter XI. For this reason the assumption of zero solubility of sulphur and oxygen in solid iron may be considered justified.

APPENDIX F  
Tie-Line Data

Data representing the tie-lines connecting the two liquids,  $L_1$  (liquid iron) and  $L_2$  (liquid slag) at the intersection of the miscibility gap and iron liquidus surfaces were interpolated from the experimental data of both Hilty and Crafts<sup>12</sup> and Schurmann and von Hertwig<sup>46</sup>. The two sets of data are listed below in Tables F1 and F2.

TIE LINE DATA INTERPOLATED FROM THE PHASE DIAGRAM OF  
HILTY AND CRAFTS

S IN L1 WT. PCT.	O IN L1 WT. PCT.	S IN L2 WT. PCT.	O IN L2 WT. PCT.	TEMP. DEG. C
0.00	0.1600	0.00	22.60	1528.0
0.01	0.1608	0.10	22.46	0.0
0.02	0.1616	0.20	22.32	0.0
0.03	0.1624	0.30	22.18	0.0
0.04	0.1632	0.40	22.04	1522.0
0.05	0.1640	0.50	21.90	1520.0
0.06	0.1648	0.60	21.76	0.0
0.07	0.1656	0.70	21.62	0.0
0.08	0.1664	0.80	21.48	0.0
0.09	0.1672	0.90	21.34	0.0
0.10	0.1680	1.00	21.20	0.0
0.11	0.1688	1.11	21.09	1513.0
0.12	0.1696	1.22	20.98	0.0
0.13	0.1704	1.33	20.87	0.0
0.14	0.1712	1.44	20.76	0.0
0.15	0.1720	1.55	20.65	0.0
0.16	0.1728	1.66	20.54	0.0
0.17	0.1736	1.77	20.43	0.0
0.18	0.1744	1.88	20.32	0.0
0.19	0.1752	1.99	20.21	0.0
0.20	0.1760	2.10	20.10	1503.0
0.21	0.1768	2.20	20.02	0.0
0.22	0.1776	2.30	19.94	0.0
0.23	0.1784	2.40	19.86	0.0
0.24	0.1792	2.50	19.78	0.0
0.25	0.1800	2.60	19.70	0.0
0.26	0.1808	2.70	19.62	0.0
0.27	0.1816	2.80	19.54	0.0
0.28	0.1824	2.90	19.46	0.0
0.29	0.1832	3.00	19.38	0.0
0.30	0.1840	3.10	19.30	1495.0
0.32	0.1856	3.32	19.16	0.0
0.34	0.1872	3.54	19.02	0.0
0.36	0.1888	3.76	18.88	0.0
0.38	0.1904	3.98	18.74	1488.0
0.40	0.1920	4.20	18.60	0.0
0.50	0.2000	5.10	18.00	1480.0
0.60	0.2080	5.80	17.30	0.0
0.70	0.2160	6.40	16.80	0.0
0.80	0.2240	6.90	16.40	1460.0
0.90	0.2320	7.40	15.90	0.0
1.00	0.2400	7.90	15.50	1450.0
1.10	0.2480	8.30	15.10	0.0
1.20	0.2560	8.70	14.80	0.0
1.30	0.2640	9.10	14.50	1440.0
1.40	0.2720	9.40	14.20	0.0
1.50	0.2800	9.80	13.90	0.0

0.0	13.60	10.10	0.2880	1.60
0.0	13.30	10.45	0.2960	1.70
0.0	13.10	10.75	0.3040	1.80
0.0	12.90	11.05	0.3120	1.90
0.0	12.70	11.40	0.3200	2.00
0.0	12.40	11.70	0.3280	2.10
0.0	12.20	12.00	0.3360	2.20
1420.0	12.00	12.35	0.3440	2.30
0.0	11.80	12.65	0.3520	2.40
0.0	11.60	12.95	0.3600	2.50
0.0	11.40	13.20	0.3680	2.60
1420.0	11.25	13.50	0.3760	2.70
0.0	11.05	13.80	0.3840	2.80
0.0	10.90	14.05	0.3920	2.90
0.0	10.70	14.35	0.4000	3.00
0.0	10.50	14.60	0.4080	3.10
0.0	10.30	14.85	0.4160	3.20
1400.0	10.15	15.10	0.4240	3.30
0.0	10.00	15.35	0.4320	3.40
0.0	9.85	15.60	0.4400	3.50
0.0	9.65	15.80	0.4480	3.60
0.0	9.50	16.00	0.4560	3.70
0.0	9.35	16.25	0.4640	3.80
0.0	9.20	16.45	0.4720	3.90
1390.0	9.05	16.70	0.4800	4.00
0.0	8.90	16.90	0.4880	4.10
0.0	8.75	17.10	0.4960	4.20
0.0	8.60	17.30	0.5040	4.30
0.0	8.45	17.50	0.5120	4.40
0.0	8.30	17.70	0.5200	4.50
0.0	8.15	17.85	0.5280	4.60
0.0	8.00	18.00	0.5360	4.70
1380.0	7.90	18.20	0.5440	4.80
0.0	7.80	18.35	0.5520	4.90
0.0	7.65	18.50	0.5600	5.00
0.0	7.50	18.65	0.5680	5.10
0.0	7.35	18.80	0.5760	5.20
0.0	7.25	18.95	0.5840	5.30
0.0	7.15	19.10	0.5920	5.40
0.0	7.00	19.25	0.6000	5.50
0.0	6.90	19.40	0.6080	5.60
0.0	6.80	19.50	0.6160	5.70
1370.0	6.70	19.65	0.6240	5.80
0.0	6.60	19.75	0.6320	5.90
0.0	6.50	19.90	0.6400	6.00
0.0	6.35	20.00	0.6480	6.10
0.0	6.25	20.10	0.6560	6.20
0.0	6.15	20.20	0.6640	6.30
0.0	6.05	20.30	0.6720	6.40
1365.0	5.95	20.40	0.6800	6.50
0.0	5.85	20.45	0.6880	6.60
0.0	5.70	20.55	0.6960	6.70
0.0	5.60	20.65	0.7040	6.80
0.0	5.50	20.70	0.7120	6.90
0.0	5.40	20.75	0.7200	7.00

7.10	0.7280	20.85	5.30	1360.0
7.20	0.7360	20.89	5.25	0.0
7.30	0.7440	20.92	5.20	0.0
7.40	0.7520	20.95	5.10	0.0
7.50	0.7600	20.98	5.00	0.0
7.60	0.7680	20.99	4.90	0.0
7.70	0.7760	21.00	4.80	0.0
7.80	0.7840	21.00	4.70	0.0
7.90	0.7920	21.00	4.65	0.0
8.00	0.8000	20.99	4.60	0.0
8.10	0.8080	20.98	4.50	1355.0
8.20	0.8160	20.97	4.45	0.0
8.30	0.8240	20.96	4.38	0.0
8.40	0.8320	20.95	4.31	0.0
8.50	0.8400	20.94	4.24	0.0
8.60	0.8480	20.93	4.17	0.0
8.70	0.8560	20.91	4.10	0.0
8.80	0.8640	20.89	4.03	0.0
8.90	0.8720	20.87	3.96	0.0
9.00	0.8800	20.85	3.89	0.0
9.10	0.8880	20.81	3.82	0.0
9.20	0.8960	20.79	3.76	0.0
9.30	0.9040	20.76	3.70	1350.0
9.40	0.9120	20.73	3.64	0.0
9.50	0.9200	20.70	3.58	0.0
9.60	0.9280	20.67	3.52	1349.0
9.70	0.9360	20.64	3.47	0.0
9.80	0.9440	20.61	3.40	0.0
9.90	0.9520	20.58	3.33	0.0
10.00	0.9600	20.55	3.27	1348.0
10.10	0.9680	20.51	3.21	0.0
10.20	0.9760	20.47	3.15	0.0
10.30	0.9840	20.43	3.10	0.0
10.40	0.9920	20.39	3.05	1347.0
10.50	1.0000	20.35	3.00	0.0
10.60	1.0080	20.31	2.95	0.0
10.70	1.0160	20.27	2.90	0.0
10.80	1.0240	20.23	2.85	1346.0
10.90	1.0320	20.19	2.80	0.0
11.00	1.0400	20.14	2.75	0.0
11.10	1.0480	20.09	2.70	0.0
11.20	1.0560	20.04	2.65	0.0
11.30	1.0640	19.99	2.60	1345.0
11.40	1.0720	19.94	2.56	0.0
11.50	1.0800	19.89	2.52	0.0
11.60	1.0880	19.84	2.48	0.0
11.70	1.0960	19.79	2.44	0.0
11.80	1.1040	19.74	2.40	1344.0
11.90	1.1120	19.69	2.36	0.0
12.00	1.1200	19.64	2.32	0.0
12.10	1.1280	19.59	2.28	0.0
12.20	1.1360	19.54	2.24	0.0
12.30	1.1440	19.49	2.20	0.0
12.40	1.1520	19.44	2.16	0.0
12.50	1.1600	19.39	2.12	1343.0

12.60	1.1680	19.34	2.09	0.0
12.70	1.1760	19.28	2.06	0.0
12.80	1.1840	19.22	2.03	0.0
12.90	1.1920	19.16	2.00	0.0
13.00	1.2000	19.10	1.97	0.0
13.10	1.2080	19.04	1.94	0.0
13.20	1.2160	18.98	1.91	0.0
13.30	1.2240	18.92	1.88	1342.0
13.40	1.2320	18.86	1.85	0.0
13.50	1.2400	18.80	1.83	0.0
13.60	1.2480	18.73	1.81	0.0
13.70	1.2560	18.66	1.79	0.0
13.80	1.2640	18.59	1.77	0.0
13.90	1.2720	18.52	1.75	0.0
14.00	1.2800	18.45	1.73	0.0
14.10	1.2880	18.38	1.72	0.0
14.20	1.2960	18.31	1.71	0.0
14.30	1.3040	18.24	1.70	0.0
14.40	1.3120	18.16	1.69	0.0
14.50	1.3200	18.08	1.68	1341.0
14.60	1.3280	18.00	1.67	0.0
14.70	1.3360	17.92	1.66	0.0
14.80	1.3440	17.84	1.65	0.0
14.90	1.3520	17.76	1.64	0.0
15.00	1.3600	17.68	1.63	0.0
15.10	1.3680	17.60	1.62	0.0
15.20	1.3760	17.52	1.61	0.0
15.30	1.3840	17.44	1.60	0.0
15.40	1.3920	17.36	1.59	0.0
15.50	1.4000	17.28	1.58	0.0
15.60	1.4080	17.21	1.57	0.0
15.70	1.4160	17.14	1.56	0.0
15.80	1.4240	17.06	1.55	0.0
15.90	1.4320	16.98	1.54	0.0
16.00	1.4400	16.90	1.53	0.0
16.10	1.4480	16.82	1.52	0.0
16.20	1.4560	16.74	1.51	0.0
16.30	1.4640	16.66	1.50	0.0
16.40	1.4720	16.58	1.49	0.0
16.50	1.4800	16.50	1.48	1340.0

TIE LINE DATA INTERPOLATED FROM THE PHASE DIAGRAM OF  
SCHURMANN AND VON HERTWIG

S IN L1 WT. PCT.	O IN L1 WT. PCT.	S IN L2 WT. PCT.	O IN L2 WT. PCT.	TEMP. DEG. C
0.00	0.16000	0.00	22.600	1528.0
0.01	0.16033	0.07	22.560	1528.0
0.02	0.16066	0.14	22.520	0.0
0.03	0.16099	0.21	22.480	0.0
0.04	0.16132	0.28	22.440	0.0
0.05	0.16165	0.35	22.400	0.0
0.06	0.16198	0.42	22.360	0.0
0.07	0.16231	0.49	22.320	0.0
0.08	0.16264	0.56	22.280	0.0
0.09	0.16297	0.63	22.240	0.0
0.10	0.16330	0.70	22.200	0.0
0.11	0.16363	0.77	22.165	0.0
0.12	0.16396	0.84	22.130	0.0
0.13	0.16429	0.91	22.095	1525.0
0.14	0.16462	0.98	22.060	0.0
0.15	0.16495	1.05	22.025	0.0
0.16	0.16528	1.12	21.990	0.0
0.17	0.16561	1.19	21.955	0.0
0.18	0.16594	1.26	21.920	0.0
0.19	0.16627	1.33	21.885	0.0
0.20	0.16660	1.40	21.850	0.0
0.21	0.16693	1.46	21.815	0.0
0.22	0.16726	1.52	21.780	0.0
0.23	0.16759	1.58	21.745	0.0
0.24	0.16792	1.64	21.710	0.0
0.25	0.16825	1.70	21.675	1520.0
0.26	0.16858	1.76	21.640	0.0
0.27	0.16891	1.82	21.605	0.0
0.28	0.16924	1.88	21.570	0.0
0.29	0.16957	1.94	21.535	0.0
0.30	0.16990	2.00	21.500	0.0
0.32	0.17056	2.12	21.430	0.0
0.34	0.17122	2.24	21.360	0.0
0.36	0.17188	2.36	21.290	0.0
0.38	0.17254	2.48	21.220	1515.0
0.40	0.17320	2.60	21.150	0.0
0.50	0.17650	3.20	20.750	1512.0
0.60	0.17980	3.80	20.400	1508.0
0.70	0.18310	4.40	20.050	0.0
0.80	0.18640	4.90	19.700	0.0
0.90	0.18970	5.40	19.350	1498.0
1.00	0.19300	5.90	19.000	0.0
1.10	0.19630	6.30	18.650	0.0
1.20	0.19960	6.80	18.300	1490.0
1.30	0.20290	7.30	17.950	1487.0
1.40	0.20620	7.70	17.600	0.0
1.50	0.20950	8.10	17.300	0.0

1.60	0.21280	8.50	17.000	1480.0
1.70	0.21610	9.00	16.700	0.0
1.80	0.21940	9.40	16.400	0.0
1.90	0.22270	9.75	16.150	0.0
2.00	0.22600	10.10	15.900	1470.0
2.10	0.22930	10.50	15.650	1468.0
2.20	0.23260	10.85	15.400	0.0
2.30	0.23590	11.20	15.150	0.0
2.40	0.23920	11.55	14.900	0.0
2.50	0.24250	11.90	14.650	1460.0
2.60	0.24580	12.20	14.400	0.0
2.70	0.24910	12.55	14.150	0.0
2.80	0.25240	12.85	13.900	0.0
2.90	0.25570	13.15	13.700	0.0
3.00	0.25900	13.50	13.450	1450.0
3.10	0.26230	13.80	13.200	0.0
3.20	0.26560	14.10	13.000	0.0
3.30	0.26890	14.40	12.750	0.0
3.40	0.27220	14.70	12.500	0.0
3.50	0.27550	14.95	12.300	0.0
3.60	0.27880	15.20	12.050	0.0
3.70	0.28210	15.40	11.850	1440.0
3.80	0.28540	15.65	11.600	0.0
3.90	0.28870	15.90	11.400	0.0
4.00	0.29200	16.10	11.150	0.0
4.10	0.29530	16.35	10.950	0.0
4.20	0.29860	16.60	10.700	0.0
4.30	0.30190	16.80	10.500	0.0
4.40	0.30520	17.00	10.300	0.0
4.50	0.30850	17.20	10.100	1430.0
4.60	0.31180	17.40	9.900	0.0
4.70	0.31510	17.60	9.700	0.0
4.80	0.31840	17.80	9.500	0.0
4.90	0.32170	17.95	9.300	1425.0
5.00	0.32500	18.10	9.100	0.0
5.10	0.32830	18.25	8.900	0.0
5.20	0.33160	18.40	8.700	0.0
5.30	0.33490	18.55	8.500	1420.0
5.40	0.33820	18.70	8.300	0.0
5.50	0.34150	18.85	8.100	0.0
5.60	0.34480	19.00	7.900	0.0
5.70	0.34810	19.15	7.750	0.0
5.80	0.35140	19.30	7.600	1415.0
5.90	0.35470	19.45	7.450	0.0
6.00	0.35800	19.60	7.300	0.0
6.10	0.36130	19.70	7.150	0.0
6.20	0.36460	19.80	7.000	0.0
6.30	0.36790	19.90	6.850	0.0
6.40	0.37120	20.00	6.700	1410.0
6.50	0.37450	20.10	6.550	0.0
6.60	0.37780	20.20	6.450	0.0
6.70	0.38110	20.30	6.350	0.0
6.80	0.38440	20.40	6.200	0.0
6.90	0.38770	20.50	6.050	0.0
7.00	0.39100	20.60	5.900	0.0



12.50	0.39430	20.65	5.800	1405.0
12.40	0.39760	20.70	5.700	0.0
12.30	0.40090	20.75	5.550	0.0
12.20	0.40420	20.80	5.450	0.0
12.10	0.40750	20.85	5.350	0.0
12.00	0.41080	20.90	5.200	0.0
11.90	0.41410	20.95	5.100	0.0
11.80	0.41740	21.00	5.000	0.0
11.70	0.42070	21.03	4.850	1400.0
11.60	0.42400	21.06	4.750	0.0
11.50	0.42730	21.09	4.650	0.0
11.40	0.43060	21.12	4.550	0.0
11.30	0.43390	21.14	4.450	0.0
11.20	0.43720	21.16	4.350	1397.5
11.10	0.44050	21.17	4.300	0.0
11.00	0.44380	21.18	4.200	0.0
10.90	0.44710	21.19	4.100	0.0
10.80	0.45040	21.20	4.000	0.0
10.70	0.45370	21.19	3.950	1395.0
10.60	0.45700	21.18	3.850	0.0
10.50	0.46030	21.16	3.750	0.0
10.40	0.46360	21.14	3.650	0.0
10.30	0.46690	21.12	3.550	0.0
10.20	0.47020	21.10	3.500	0.0
10.10	0.47350	21.08	3.400	0.0
10.00	0.47680	21.06	3.350	1392.5
9.90	0.48010	21.04	3.250	0.0
9.80	0.48340	21.02	3.200	0.0
9.70	0.48670	21.00	3.100	0.0
9.60	0.49000	20.97	3.050	0.0
9.50	0.49330	20.94	2.950	0.0
9.40	0.49660	20.91	2.900	0.0
9.30	0.49990	20.88	2.800	0.0
9.20	0.50320	20.84	2.750	0.0
9.10	0.50650	20.80	2.700	0.0
9.00	0.50980	20.75	2.650	1390.0
8.90	0.51310	20.70	2.550	0.0
8.80	0.51640	20.65	2.500	0.0
8.70	0.51970	20.60	2.450	1389.0
8.60	0.52300	20.55	2.400	0.0
8.50	0.52630	20.50	2.350	0.0
8.40	0.52960	20.45	2.300	0.0
8.30	0.53290	20.40	2.250	0.0
8.20	0.53620	20.35	2.200	1388.0
8.10	0.53950	20.30	2.150	0.0
8.00	0.54280	20.25	2.100	0.0
7.90	0.54610	20.15	2.050	0.0
7.80	0.54940	20.05	2.000	0.0
7.70	0.55270	19.95	1.950	0.0
7.60	0.55600	19.85	1.900	1387.0
7.50	0.55930	19.80	1.850	0.0
7.40	0.56260	19.75	1.800	0.0
7.30	0.56590	19.70	1.760	0.0
7.20	0.56920	19.65	1.720	0.0
7.10	0.57250	19.60	1.680	1386.0

12.60	0.57580	19.55	1.640	0.0
12.70	0.57910	19.50	1.500	0.0
12.80	0.58240	19.42	1.570	0.0
12.90	0.58570	19.34	1.540	0.0
13.00	0.58900	19.26	1.510	0.0
13.10	0.59230	19.18	1.480	0.0
13.20	0.59560	19.10	1.450	1385.0
13.30	0.59890	19.02	1.420	0.0
13.40	0.60220	18.96	1.390	0.0
13.50	0.60550	18.87	1.360	0.0
13.60	0.60880	18.79	1.330	0.0
13.70	0.61210	18.70	1.300	0.0
13.80	0.61540	18.62	1.270	0.0
13.90	0.61870	18.53	1.240	0.0
14.00	0.62200	18.45	1.210	1384.0
14.10	0.62530	18.36	1.180	0.0
14.20	0.62860	18.28	1.150	0.0
14.30	0.63190	18.19	1.120	0.0
14.40	0.63520	18.11	1.090	0.0
14.50	0.63850	18.02	1.060	0.0
14.60	0.64180	17.94	1.030	0.0
14.70	0.64510	17.85	1.000	0.0
14.80	0.64840	17.77	0.980	0.0
14.90	0.65170	17.68	0.960	0.0
15.00	0.65500	17.60	0.940	0.0
15.10	0.65830	17.51	0.920	1383.0
15.20	0.66160	17.43	0.900	0.0
15.30	0.66490	17.34	0.880	0.0
15.40	0.66820	17.26	0.860	0.0
15.50	0.67150	17.17	0.840	0.0
15.60	0.67480	17.09	0.820	0.0
15.70	0.67810	17.00	0.800	0.0
15.80	0.68140	16.92	0.780	0.0
15.90	0.68470	16.83	0.760	0.0
16.00	0.68800	16.75	0.740	0.0
16.10	0.69130	16.66	0.730	0.0
16.20	0.69460	16.58	0.720	0.0
16.30	0.69790	16.49	0.710	1382.0
16.40	0.70000	16.40	0.700	1382.0

## APPENDIX G

Considerations of the Effect of the Position  
of the Plait Point on Solidification

Figure G1 is a schematic representation of the Fe-FeO-FeS system qualitatively similar to that determined experimentally by both Hilty and Crafts<sup>12</sup>, and Schurmann and von Hertwig<sup>46</sup>. The plait point P and the tie-lines have been arranged in such a way as to emphasize possible effects of curvature in the line MP, on solidification. Curvature of this line makes it possible for the plait point to have a higher O/S ratio than the adjacent section of the line MP and this circumstance would have a considerable effect on the solidification of alloys encountering the miscibility gap, according to the models outlined in the main text. Two alloys may be used as examples to illustrate the effect on equilibrium solidification.

Firstly consider an alloy a. Under equilibrium conditions the fractions of  $L_1$  and  $L_2$  in the total liquid may easily be found by application of the lever rule. When the two liquids are joined by the tie-line ab at the initiation of the monotectic three-phase reaction:

$$f'_{L_1} / f'_{L_2} = ab/aa, \quad \text{where } f'_{L_1} + f'_{L_2} = 1$$

This means the liquid is composed of 100 pct  $L_1$  and an infinitesimal amount of  $L_2$ . On cooling to the tie-line a'b':

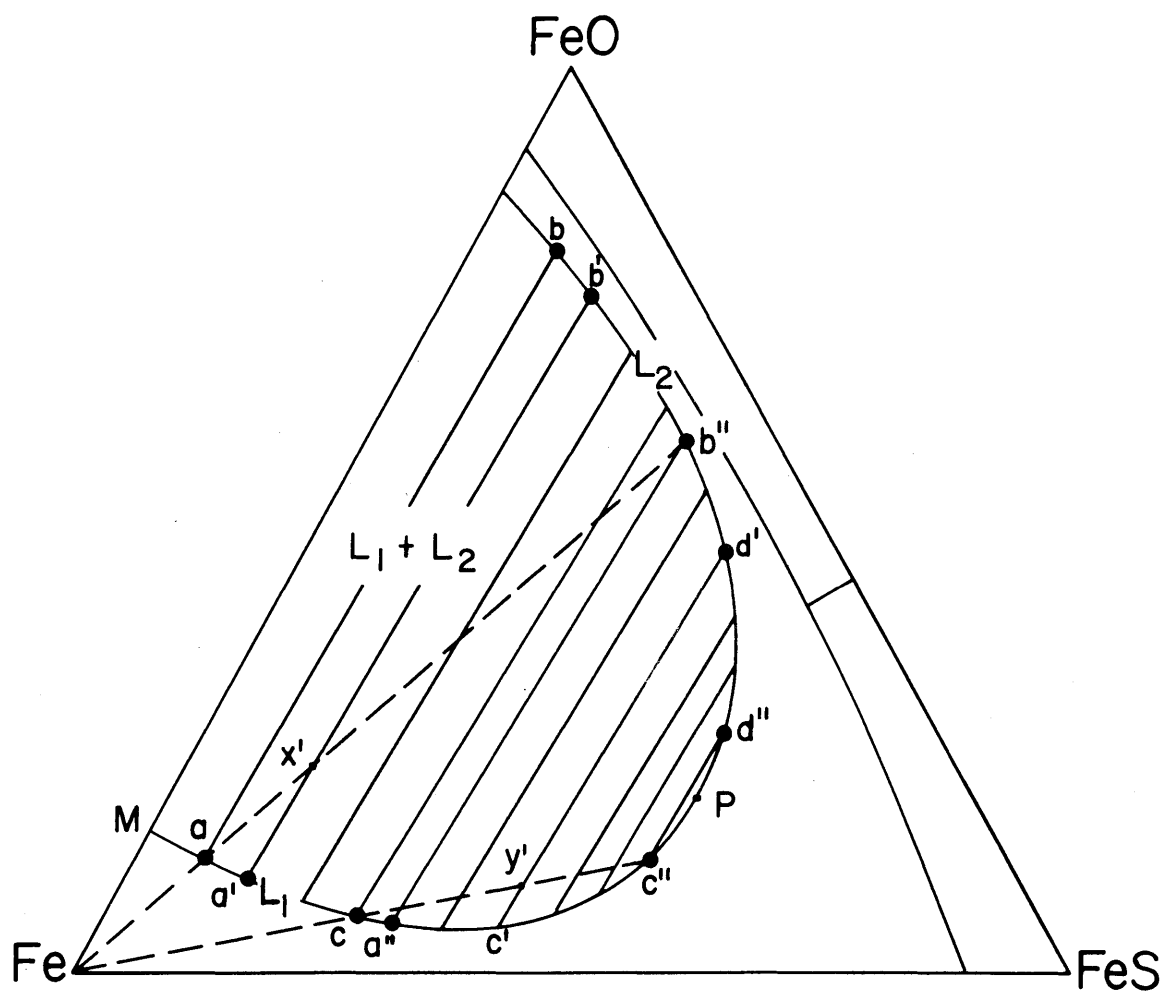


Figure G1. Schematic illustration of the Fe-FeO-FeS phase diagram used in considering equilibrium solidification.

$$f'_{L_1} / f'_{L_2} = b'x' / a'x' = 7/1$$

Thus the liquid now contains about 87.5 pct  $L_1$  of composition  $a'$  and 12.5 pct  $L_2$  of composition  $b'$ .

It can be seen that as cooling continues the ratio of  $L_1$  to  $L_2$  decreases until by the time  $L_1$  reaches the composition  $a''$  it is consumed completely, for at this point:

$$f'_{L_1} / f'_{L_2} = b''b'' / a''b''$$

that is the liquid is now 100 pct  $L_2$ . Note that the composition of  $L_2$ ,  $b''$ , in equilibrium with  $a''$  has the same O/S ratio as the original melt of composition  $a$ .

Now consider a melt of composition  $c$  which has cooled to the iron liquidus temperature. At position  $c$  the liquid consists of 100 pct  $L_1$  in equilibrium with an infinitesimal quantity of  $L_2$  of composition  $d$ . As the melt cools the tie line  $c'd'$  is reached and at this time the relative quantities of  $L_1$  and  $L_2$  are given by:

$$f'_{L_1} / f'_{L_2} = y'd' / y'c' = 5/1$$

i.e., 84 pct  $L_1$  of composition  $c'$ , and 16 pct  $L_2$  of composition  $d'$ . This is the maximum amount of  $L_2$  existing during solidification.

Application of the lever rule to the lower temperature tie-lines shows that between  $c'd'$  and  $c''d''$  the quantity of  $L_2$  decreases until it is completely consumed as it reaches

composition d". The O/S ratio of the  $L_1$  of composition c" in equilibrium with  $L_2$  at this point is the same as that of the original melt c.

From the above examples one may conclude that under equilibrium conditions, if the line originating from the solid iron phase and passing through the original melt composition intersects the miscibility gap twice on the  $L_1$  side of the plait point then  $L_2$ , rather than  $L_1$ , will be consumed at the end of the monotectic three phase reaction. If, on the other hand, the line intersects the miscibility gap once on the  $L_1$  side of the plait point and once on the  $L_2$  side, then  $L_1$  will be consumed at the end of the reaction. The first condition cannot arise if the line of intersection of the miscibility gap and iron liquidus surfaces is straight up to the plait point. In fact, for the simple case of zero solid solubility of oxygen and sulphur in iron, the plait point must be at a higher O/S ratio than the minimum O/S ratio on the line of intersection for the first condition to arise.

It is interesting to consider the effect of such a situation on the "isolation" solidification model. Figure G2 is a schematic representation of an Fe-FeO-FeS phase diagram which would allow the consumption of  $L_2$  in equilibrium solidification, with some aspects exaggerated for the sake of clarity. The proposed "isolation" solidification model employs a series of equilibria in which  $L_2$  is formed from  $L_1$  and then cut off in pools. Two steps in this local equilibrium process, the sizes of which are exaggerated, may be considered by reference to Figure G2.

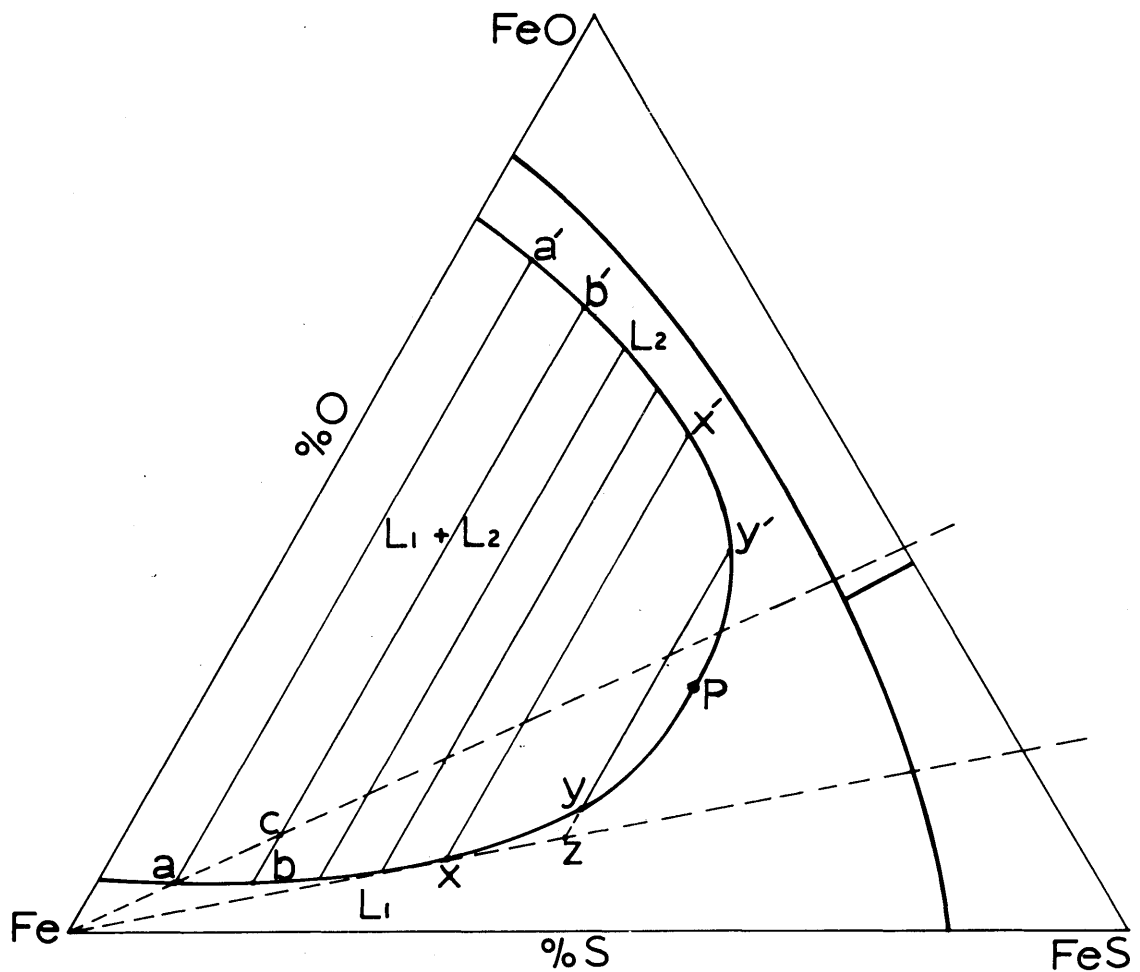


Figure G2. Schematic illustration of the Fe-FeO-FeS phase diagram used in considering isolation solidification.

In step 1 liquid  $L_1$  of composition  $a$  when cooled under conditions of local equilibrium from  $a$  to  $b$  generates some  $L_2$  of composition  $b'$ . The quantity  $f'_{L_2}$  of  $b'$  generated in this step is given by the lever rule:

$$f'_{L_2} = bc/bb' \quad \text{where } f'_{L_1} + f'_{L_2} = 1$$

This quantity of  $L_2$  is then entrapped by the growing solid iron and removed from consideration as far as the progress of the monotectic three-phase reaction is concerned.  $L_1$ , now of composition  $b$ , continues to cool and produces more  $L_2$  in succeeding steps similar to step 1.

In step 2 cooling of  $L_1$  from  $x$  to  $y$  is considered. Application of the lever rule to compute the quantity  $f'_{L_2}$  of  $L_2$  of composition  $y'$  produced in this step gives:

$$f'_{L_2} = -zy/yy' \quad \text{a negative quantity.}$$

This is impossible since the liquid  $L_2$  is "isolated". Clearly then  $L_1$  cannot change in composition from  $x$  to  $y$  while satisfying the condition that the O/S ratio of the overall liquid must remain constant.

In reality, what must happen is that when  $L_1$  reaches position  $x$ , a point corresponding to the minimum O/S ratio on the curve, further cooling would cause precipitation of solid iron only; the composition of the remaining liquid moving off the line of two-fold saturation and down the iron liquidus surface in the direction  $xz$ . In other words the



monotectic three-phase reaction ceases when  $L_1$  reaches composition  $x$ .

The liquids, from which the inclusions form, would in this case be  $L_2$ , in the composition range  $a'$  to  $x'$ , and the interdendritic  $L_1$  of composition  $x$ . Thus no inclusion with O/S ratios corresponding to the composition range  $x$  to  $x'$  could be formed during non-equilibrium solidification of any alloy on the  $L_1$  side of the miscibility gap in this system and a whole range of inclusion composition would never be found in the solidified alloys.

The two phase diagrams given by Hilty and Crafts<sup>12</sup> and Schurmann and von Hertwig<sup>46</sup> both show the O/S ratio of the plait point at a higher level than the portion of the curved intersection of the miscibility gap with the iron liquidus surface immediately on the  $L_1$  side of it. However, in both cases the O/S ratio is only marginally higher and a slight adjustment to the position of the plait point, which is only approximate in any case, would put it at the minimum O/S ratio on the curve. This consideration, together with the fact that the underlying tie line data is too scattered to justify a curved rather than a straight line from the Fe-FeO monotectic to the plait point, is the reason that the consumption of  $L_2$  during the three-phase reaction is not considered in the main text.

The gap expected in the range of inclusion composition for the Fe-FeO-FeS system was determined by consideration of the exact curves given by Schurmann and von Hertwig<sup>46</sup> and by

Hilty and Crafts<sup>12</sup> in their phase diagrams. For the diagram of Crafts the gap extends from 25 pct FeS in the inclusions to 67 pct FeS and for the Schurmann diagram from 45 pct FeS to 82 pct FeS. However, metallographic examination of the specimens produced in this work revealed no such gap.

It is also worthy of note that the inclusions formed in an "equilibrium" solidification process would in no way be affected by such variations in the type of phase diagram. The liquid remaining at the completion of the monotectic three-phase reaction would have the same O/S ratio regardless of whether it was  $L_1$  or  $L_2$  and it would also occupy the same position with respect to the dendrites.

## APPENDIX H

## "Equilibrium" Solidification Model - Computer Program

```

1      DIMENSION A(200),B(200),C(200),D(200),
2      2X(200),Y(200),Z(200),T(200)
3      READ,MAX,XN,YN,ZN
4      DO 101 I=1,MAX
5      101 READ,A(I),B(I),C(I),D(I),T(I)
6      READ,K
7      X(K)=XN
8      Y(K)=YN
9      Z(K)=ZN
10     MMM=MAX-1
11     MAXN=K-1
12     DO 102 J=K,MMM
13     MAXN=MAXN+1
14     Y(J)=(B(K)*C(J)-A(K)*D(J))/(B(J)*C(J)-A(J)*D(J))
15     Z(J)=(B(K)*A(J)-A(K)*B(J))/(A(J)*D(J)-B(J)*C(J))
16     X(J)=1.-Y(J)-Z(J)
17     102 IF(Y(J).LT.0.0.OR.Z(J).LT.0.0) GO TO 103
18     103 CONTINUE
19     DO 104 I=K,MAXN
20     PRINT,I
21     PRINT,A(I),B(I),C(I),D(I),T(I)
22     104 PRINT,X(I),Y(I),Z(I)
23     STOP
24     END

```

In the above program A, B, C, D and T represent  $C_{L_1}$ ,  $C'_{L_1}$ ,  $C_{L_2}$ ,  $C'_{L_2}$  and the temperature respectively and X, Y, and Z represent  $f_\alpha$ ,  $f_{L_1}$  and  $f_{L_2}$ .

## APPENDIX I

## "Isolation" Solidification Model - Computer Program

```

1      DIMENSION A(200),B(200),C(200),D(200),X(200),Y(200),Z(200),
      1DELX(200),DELY(200),DELZ(200),DIVZX(200),T(200)
2      READ,MAX,X(1),Y(1),Z(1)
3      DO 101 I=1,MAX
4      101 READ,A(I),B(I),C(I),D(I),T(I)
5          MMM=MAX-1
6          DO 102 J=1,MMM
7              AN1=(A(J+1)-A(J))/C(J)
8              BN1=(B(J+1)-B(J))/D(J)
9              AD1=A(J)/C(J)
10             BD1=B(J)/D(J)
11             AN2=(A(J+1)-A(J))/A(J)
12             BN2=(B(J+1)-B(J))/B(J)
13             AD2=C(J)/A(J)
14             BD2=D(J)/B(J)
15             QUOT1=(AN1-BN1)/(AD1-BD1)
16             QUOT2=(AN2-BN2)/(AD2-BD2)
17             Y(J+1)=Y(J)-Y(J)*QUOT1
18             Z(J+1)=Z(J)-Y(J)*QUOT2
19             X(J+1)=1-Y(J+1)-Z(J+1)
20             DELX(J)=X(J+1)-X(J)
21             DELY(J)=Y(J+1)-Y(J)
22             DELZ(J)=Z(J+1)-Z(J)
23     102 DIVZX(J)=DELZ(J)/DELX(J)
24             DO 103 I=1,MAX
25                 PRINT,I
26                 PRINT,A(I),B(I),C(I),D(I),T(I)
27                 PRINT,X(I),Y(I),Z(I)
28     103 PRINT,DELX(I),DELY(I),DELZ(I),DIVZX(I)
29             STOP
30             END

```

In the above program A, B, C, D and T represent  $C_{L_1}$ ,  $C'_{L_1}$ ,  $C_{L_2}$ ,  $C'_{L_2}$  and the temperature respectively and X, Y and Z represent  $f_\alpha$ ,  $f_{L_1}$  and  $f_{L_2}$ .

## APPENDIX J

## Point Counting Technique

A two dimensional systematic point count was used to determine the volume fractions of the FeO or FeS dendrites in the inclusions. The actual method used involved the superposition of a fine mesh lattice on a photomicrograph (1000X) of the inclusion to be investigated. Various lattice spacings were used so that approximately 100 intersections or points could be included within the inclusion section in all cases.

The errors arising in the use of such a method are of interest. Hilliard and Cahn<sup>57</sup> showed that the standard deviations to be expected in the measurement of volume fractions of  $\alpha$  features using this method depend on a number of variables. These include the expected perimeter length of the  $\alpha$  features, the expected number of the features, the expected number of points that they occupy, the expected area that they occupy and the lattice spacing. As these factors vary from one inclusion to the next, the expected standard deviation of each measurement would be different. Rather than calculate the expected standard deviation for each inclusion measured, which would be an extremely laborious process, it was decided to measure the standard deviation observed on one reasonably representative inclusion experimentally. The standard deviation obtained in this way may be used as an estimate of the deviations likely to occur in all measurements.

In order to find the standard deviation in the measurements on one inclusion the lattice or grid was laid down on the photomicrograph of the inclusion in random positions and the point count repeated each time, on ten separate occasions. The following results were obtained:

Vol. % FeO=54, 58, 59, 55, 57, 58, 59, 59, 63, 56

The mean of these readings is 58 and the deviations from this mean are as follows:

Deviations: -4, 0, +1, -3, -1, 0, +1, +1, +5, -2

From these deviations a root mean square deviation of  $\sigma = 2.5$  was calculated.

This standard deviation, although it may only be applied to the general case with a degree of circumspection, is an indication that the measurements are reproducible and are sensitive enough for use as a test of the validity of the models.

As a further test of reproducibility of the two-dimensional systematic point count technique, the volume fractions of FeO or FeS dendrites in six inclusions were measured by both the point count method and an areal analysis. The areal analysis was conducted by making a slide of the photomicrograph containing the inclusion; projecting the image onto a paper screen, tracing the outline of the phases of interest on the paper; and finally cutting out the areas of the phases on the paper and weighing the paper. In this

way the volume fraction of the FeO or FeS dendrites could be found and compared to the value obtained from a point count on the same inclusion. The results of these measurements on inclusions in samples number 100-2 are given below in Table J1.

Table J1  
Comparison of the Point Counting and Areal  
Analysis Techniques

inclusion number	vol. pct. of FeO or FeS from two-dimensional systematic point count	vol. pct. of FeO or FeS from areal analysis
1	89% FeO	86% FeO
2	61% FeO	63% FeO
3	20% FeO	21% FeO
4	25% FeS	25% FeS
5	60% FeS	57% FeS
6	75% FeS	77% FeS

It can be seen that the values obtained by these techniques agree within a few percent in all cases. This is further evidence of the reproducibility of the method used.

In conclusion it may be said that the two-dimensional systematic point count method is sufficiently accurate and

reproducible to be used as a means of characterizing the inclusion compositions obtained in this study.



## APPENDIX K

## Calculation of Inclusion Composition

Inclusion composition was investigated by consideration of the solidification of  $L_2$  formed during the monotectic three phase reaction. The necessary calculations were carried out in two steps.

In the first step the solidification of the oxygen and sulphur rich liquid  $L_2$  was considered from the completion of the monotectic reaction down to the appropriate pseudobinary eutectic valley. Calculations were made for eight different liquids, the O/S ratios of which varied between infinity and 0.09; the complete range for  $L_2$  according to the phase diagram of Hilty and Crafts<sup>12</sup>. The calculation for one of these liquids, of O/S ratio 0.16, is used as an example and the results for the other ratios are tabulated. All the symbols used in this Appendix are defined in Table K4.

The compositions  $C_{L_2}^M$ ,  $C_{L_2}^{M'}$  of  $L_2$  of O/S ratio 0.16 at the end of the three-phase reaction is found from the phase diagram to be 20.54 pct S and 3.29 pct O. As only pure iron is precipitated while  $L_2$  moves across the iron liquidus surface to the pseudobinary eutectic line the O/S ratio remains constant at 0.16 and so the composition of the liquid remaining at the pseudobinary is found easily from the phase diagram. This composition  $C_{L_2}^E$ ,  $C_{L_2}^{E'}$  is 27.9 pct S and 4.46 pct O.

Now the fraction  $f_{L_2}^*$  of the original amount of  $L_2$  at the end of the monotectic reaction remaining at the pseudo-binary eutectic line is given by a simple mass balance:

$$C_{L_2}^E f_{L_2}^* = C_{L_2}^M, \quad f_{L_2}^* = C_{L_2}^M / C_{L_2}^E = 20.54 / 27.9 = 0.735$$

thus between the miscibility gap and the eutectic line 26.5 pct of the  $L_2$  is deposited as solid iron on the pre-existing dendrites. The fraction of  $L_2$  built up by the end of the monotectic reaction,  $f_{L_2}^M$ , is known for alloys whose overall compositions lie on the line of intersection of the miscibility gap and iron liquidus surface. For an alloy of O/S ratio 0.16,  $f_{L_2}^M$  is 0.097. A fraction 0.735 of this remains when the eutectic line is reached and so the absolute quantity  $f_{L_2}^E$  of  $L_2$  remaining at the eutectic line is given by:

$$f_{L_2}^E = f_{L_2}^M \times f_{L_2}^* = 0.097 \times 0.735 = 0.071$$

Hence,  $f_{\alpha}^E = 0.929$ .

Table K1 shows the corresponding results for all the alloys considered in this way. The overall compositions of these alloys all lie on the  $L_1$  side of the line of intersection of the miscibility gap and iron liquidus surfaces.

Table K1

Liquid Compositions and Weight Fractions of  $L_2$   
During Solidification Between the Miscibility<sup>2</sup>  
Gap and the Eutectic Valley

O/S	$C_{L_2}^M, C_{L_2}^{M'}$ (wt pct)	$C_{L_2}^E, C_{L_2}^{E'}$ (wt pct)	$f_{L_2}^*$	$f_{L_2}^M$	$f_{\alpha}^M$	$f_{L_2}^E$	$f_{\alpha}^E$
0.09	16.5 S 1.480	29.16S 2.620	0.565	1.000	0.000	0.565	0.435
0.11	19.4 S 2.130	28.75S 3.160	0.675	0.276	0.724	0.186	0.814
0.16	20.54S 3.290	27.90S 4.460	0.735	0.097	0.903	0.071	0.929
0.48	17.5 S 8.450	21.9 S 10.5 O	0.800	0.023	0.977	0.018	0.982
1.68	8.8 S 14.7 O	10.4 S 17.450	0.842	0.0114	0.9886	0.0096	0.9904
4.08	4.5 S 18.4 O	5.0 S 20.4 O	0.902	0.0089	0.9911	0.0080	0.9920
16.08	1.33S 20.900	1.39S 22.300	0.937	0.0077	0.9923	0.0072	0.9928
$\infty$	0.0 S 22.6 O	0.0 S 22.9 O	0.987	0.0071	0.9929	0.0070	0.9930

The second step, which is the final stage of solidification, involves the pseudobinary eutectic reaction and the ternary eutectic reaction. At the beginning of this process  $L_2$  of a known composition precipitates small quantities of iron and either FeO or FeS depending on which eutectic line it lies on. For O/S ratios greater than 0.375 the Fe-FeO eutectic reaction takes place and for ratios between 0.375 and 0.09 the Fe-FeS

eutectic reaction occurs. The initial composition of  $L_2$ , the composition of the ternary eutectic and the compositions of FeO, FeS and Fe are all known. Hence the quantities of iron and FeO or FeS, which precipitate before the remaining liquid reaches the ternary eutectic composition and freezes, may be found by use of the following simple mass balance:

For O/S ratios greater than 0.375,

$$C_{\alpha}'' f_{\alpha}'' + C_{TE}'' f_{TE}'' + C_{FeO}'' f_{FeO}'' = C_{L_2}^E \quad (K1)$$

$$C_{\alpha}' f_{\alpha}' + C_{TE}' f_{TE}' + C_{FeO}' f_{FeO}' = C_{L_2}^{E'} \quad (K2)$$

$$f_{\alpha}'' + f_{FeO}'' + f_{TE}'' = 1 \quad (K3)$$

and for O/S ratios smaller than 0.375 and greater than 0.09,

$$C_{\alpha}'' f_{\alpha}'' + C_{TE}'' f_{TE}'' + C_{FeS}'' f_{FeS}'' = C_{L_2}^E \quad (K4)$$

$$C_{\alpha}' f_{\alpha}' + C_{TE}' f_{TE}' + C_{FeS}' f_{FeS}' = C_{L_2}^{E'} \quad (K5)$$

$$f_{\alpha}'' + f_{FeS}'' + f_{TE}'' = 1 \quad (K6)$$

In the above equations the initial fraction of  $L_2$  is taken as one in order to consider the composition of the inclusions formed more easily.

It is assumed that  $C_{\alpha}$ ,  $C_{\alpha}' = 0$  and from the phase diagram  $C_{TE} = 24.0$ ,  $C_{TE}' = 9.0$ ,  $C_{FeO} = 0$ ,  $C_{FeO}' = 25.0$ ,  $C_{FeS} = 38.0$ ,

and  $C_{\text{FeS}}^I = 0$ . Consequently equations (K1), (K2), (K4) and (K5) reduce to the following:

Where  $O/S > 0.375$ ,

$$24 f_{\text{TE}}'' = C_{\text{L}_2}^{\text{E}} \quad (\text{K7})$$

$$9 f_{\text{TE}}'' + 25 f_{\text{TE}}'' = C_{\text{L}_2}^{\text{E}'} \quad (\text{K8})$$

Where  $0.09 < O/S < 0.375$

$$24 f_{\text{TE}}'' + 38 f_{\text{FeS}}'' = C_{\text{L}_2}^{\text{E}} \quad (\text{K9})$$

$$9 f_{\text{TE}}'' = C_{\text{L}_2}^{\text{E}'} \quad (\text{K10})$$

Knowing the values of  $C_{\text{L}_2}^{\text{E}}$  and  $C_{\text{L}_2}^{\text{E}'}$  for the various O/S ratios the above equation may be used to solve for  $f_{\alpha}''$ ,  $f_{\text{FeO}}''$ ,  $f_{\text{FeS}}''$  and  $f_{\text{TE}}''$ . These values are a measure of the inclusion composition. Also multiplication by  $f_{\text{L}_2}^{\text{E}}$  from Table K1 above gives the true fractions of the phases,  $f_{\alpha}$ ,  $f_{\text{FeS}}$ ,  $f_{\text{FeO}}$ , and  $f_{\text{TE}}$  precipitated during this step. These various values are given below in Table K2.

Table K2

Liquid Compositions and Weight Fractions  
of the Various Phases Involved During  
the Solidification of  $L_2$  from the  
Intersection of the Pseudobinary Eutectic  
to the Ternary Eutectic Point

O/S	$C_{L_2}^E$ wt. pct	$C_{L_2}^{E'}$ wt. pct	$f_{L_2}^E$	$f_{TE}''$	$f_{FeS}''$	$f_{\alpha}''$	$f_{TE}$	$f_{FeS}$	$f_{\alpha}$
0.09	29.16	2.62	0.565	0.291	0.584	0.125	0.1645	0.3300	0.0706
0.11	28.75	3.16	0.186	0.352	0.534	0.114	0.0655	0.0993	0.0212
0.16	27.90	4.46	0.071	0.496	0.421	0.083	0.0352	0.0299	0.0059
					$f_{FeO}''$			$f_{FeO}$	
0.48	21.90	10.5	0.018	0.909	0.090	0.001	0.0164	0.0016	0.00002
1.68	10.4	17.45	0.010	0.433	0.542	0.025	0.0043	0.0054	0.00025
4.08	5.0	20.4	0.008	0.208	0.742	0.050	0.0023	0.0059	0.0004
16.08	1.39	22.3	0.0072	0.058	0.871	0.071	0.0004	0.0063	0.0005
$\infty$	0.0	22.9	0.0070	0.0	0.916	0.084	0.0	0.0064	0.0006

As the quantities of iron precipitated during cooling of  $L_2$  from the miscibility gap to the ternary eutectic point are quite small, and the pre-existing iron dendrite network is very extensive, for alloys of reasonable sulphur and oxygen content, it is assumed that all of the iron precipitated from  $L_2$  deposits on the existing dendrites and does not become part of the inclusion. Taking the density of FeO equal to  $4.5 \text{ gm/cm}^3$  and the density of FeS equal to  $4.77 \text{ gm/cm}^3$  the

volume fractions of FeO, FeS and ternary eutectic making up the inclusions were calculated from  $f_{\text{FeO}}''$ ,  $f_{\text{FeS}}''$  and  $f_{\text{TE}}''$ . Table K3 lists the inclusion composition in volume percent as a function of the melt O/S ratio for "equilibrium" solidification. This information was used to plot Figure 23 in the main text and a similar graph was obtained by an identical method using the data from the phase diagram of Schurmann and von Hertwig<sup>46</sup>.

Table K3

Inclusion Composition for Melts of Various O/S Ratios;  
"Equilibrium" Solidification Model

O/S ratio of melt	volume percent FeO	volume percent FeS	volume percent ternary eutectic
0.09	-	67	33
0.11	-	60	40
0.16	-	46	54
0.48	9	-	91
1.68	56	-	44
4.08	78	-	22
16.08	94	-	6
$\infty$	100	-	0

Table K4

## Various Symbols Used in Appendix K

symbol	definition
$C_{\alpha}$	sulphur content of solid iron (wt. pct.)
$C'_{\alpha}$	oxygen content of solid iron (wt. pct.)
$C_{L_2}^M$	sulphur content of $L_2$ at completion of monotectic reaction (wt. pct.)
$C_{L_2}^{M'}$	oxygen content of $L_2$ at completion of monotectic reaction (wt. pct.)
$C_{L_2}^E$	sulphur content of $L_2$ at the intersection of pseudo-binary eutectic (wt. pct.)
$C_{L_2}^{E'}$	oxygen content of $L_2$ at the intersection of pseudo-binary eutectic (wt. pct.)
$C_{FeO}$	sulphur content of FeO (wt. pct.)
$C'_{FeO}$	oxygen content of FeO (wt. pct.)
$C_{FeS}$	sulphur content of FeS (wt. pct.)
$C'_{FeS}$	oxygen content of FeS (wt. pct.)
$C_{TE}$	sulphur content of ternary eutectic (wt. pct.)
$C_{TE}^I$	oxygen content of ternary eutectic (wt. pct.)
$f_{L_2}^M$	fraction of $L_2$ at the end of the monotectic reaction
$f_{\alpha}^M$	fraction of $\alpha$ at the end of the monotectic reaction
$f_{L_2}^*$	fraction of $f_{L_2}^M$ remaining at the intersection of the pseudobinary eutectic
$f_{L_2}^E$	fraction of $L_2$ at the intersection of the pseudo-binary eutectic
$f_{\alpha}^E$	fraction of $\alpha$ at the intersection of the pseudo-binary eutectic
$f_{\alpha}''$	fraction of $f_{L_2}^E$ deposited as iron



Table K4 (cont'd)

symbol	definition
$f''_{\text{FeS}}$	fraction of $f_{L_2}^E$ deposited as FeS
$f''_{\text{FeO}}$	fraction of $f_{L_2}^E$ deposited as FeO
$f''_{\text{TE}}$	fraction of $f_{L_2}^E$ deposited as ternary eutectic
$f_{\alpha}$	fraction of $\alpha$
$f_{\text{FeO}}$	fraction of FeO
$f_{\text{FeS}}$	fraction of FeS
$f_{\text{TE}}$	fraction of ternary eutectic

## BIOGRAPHICAL NOTE

The author was born in Manchester, Lancashire, England on October 24, 1942. He attended Chetham's Hospital School and Manchester University where he received the degree of Bachelor of Science in Metallurgy in 1964. He entered the Graduate School of the Massachusetts Institute of Technology in September, 1964 as a candidate for the degree of Doctor of Philosophy, with a major in Metallurgy and a minor in Industrial Management.

The author is a member of the Iron and Steel Institute, the Institution of Metallurgists, the Metallurgical Society of the A.I.M.E. and the American Society for Metals.